Materials Today Physics 27 (2022) 100832

Contents lists available at ScienceDirect

Materials Today Physics

journal homepage: www.journals.elsevier.com/materials-today-physics

A review and progress of multiphase flows in atmospheric and low pressure plasma spray advanced coating

Sen-Hui Liu [a,b,c], Juan.P Trelles [b], Chang-Jiu Li [a], Cheng-Xin Li [a,*], Hong-Bo Guo [c,**]

[a] School of Materials Science and Engineering, State Key Laboratory for Mechanical Behavior of Materials, Xi'an Jiaotong University, Xi'an, Shaanxi, 710049, China
[b] School of Materials Science and Engineering, Key Laboratory of High-Temperature Structure Materials and Protective Coatings, Beihang University, Beijing, 100191, China
[c] Department of Mechanical Engineering, University of Massachusetts Lowell, Massachusetts 01854, USA

ARTICLE INFO

Keywords:
Plasma spray
Laminar plasma spray
Modeling simulation
TBCs
PS-PVD

ABSTRACT

Arc plasma sprayed thin films and coatings exhibit excellent mechanical properties for anti-corrosion, anti-wear, anti-radiation, thermal isolation, and heat conduction applications. These coatings have been used in metallic parts of aircraft engines, automobile engines, gas turbine engines, diesel engines, nuclear power equipment, and oil refining equipment. The microstructures and properties of the deposited coatings change with plasma spray processing parameters. In general, depositing of coatings through plasma spraying involves different types of material flow and atomization. Under constant feed rates of metallic or ceramic powders, various spraying distances are employed to deposit the coating. Therefore, the heating history, motion, and phase transformation of the powder in the plasma jet during plasma spraying have been extensively studied. This paper reviews the current state of plasma spray technology for the production of coatings and presents multiphase flows and heat transfer mechanisms from powders to the coating. Progresses in novel atmospheric micro plasma spraying and long laminar plasma spraying technology are shown, low-pressure supersonic plasma-induced physical vapor deposition of quasi-columnar ceramic coatings is also presented. The shadowing effect, flash vaporization, breakup, and atomization of in-flight droplets at a chamber pressure of 200 Pa, and maximum distance of 2200 mm were clarified. Finally, the remaining unresolved issues are discussed, and a future outlook on plasma spraying technology is presented.

1. Introduction

1.1. History and recent developments on arc plasma spraying

The production of coatings through plasma spraying allows modification of the surface properties of parts or components commonly used in aircraft engines, automobile engines, gas turbine engines, nuclear power equipment, and oil refining equipment. These surface modifications are indispensable to ensure that metallic parts can work reliably even under extreme operating conditions, such as highly corrosive environments, wear environments, and high-temperature settings. With the development of plasma spraying technology, worn parts can be repaired and rebuilt to their original dimensions to extend their component life. This technology is particularly useful for the reconstruction of materials for military and aerospace applications. Commonly, the coating is in the form of powders, ceramic rods, and wires. Besides, transferred arc plasma-weld overlays have also been used as a coating technology (Fig. 1-a to 1-c) [1].

For arc plasma spraying using powders (Fig. 1-d to 1-g), coatings are formed through the successive impingement of molten droplets and/or semi-molten particles, followed by flattening, rapid cooling, and solidification on the prepared substrate [2]. The coatings usually exhibit a lamellar microstructure with some micropores or globular pores, an interlamellar unbonded interface, and vertical cracks at the cross-sections [3,4]. The intersplat unbonded interfaces primarily affect properties of the coatings, such as thermal conductivity, electrical conductivity, Young's modulus, cohesive strength, and fracture toughness

* Corresponding author. School of Materials Science and Engineering, Xi'an Jiaotong University, State Key Laboratory for Mechanical Behavior of Materials, Xi'an, Shaanxi Province, 710049, PR China.
** Corresponding author. School of Materials Science and Engineering, Beihang University, Key Laboratory of Aerospace Materials and Performance (Ministry of Education), Beihang University, No. 37 Xueyuan Road, Beijing, 100191, E-, China.
E-mail addresses: licx@xjtu.edu.cn (C.-X. Li), guo.hongbo@buaa.edu.cn (H.-B. Guo).

https://doi.org/10.1016/j.mtphys.2022.100832
Received 12 August 2022; Accepted 29 August 2022
Available online 6 September 2022

Abbreviations

APS	Atmospheric Plasma Spraying
ALPS	Atmospheric Laminar Plasma Spray
AMPS	Atmospheric Micro-Plasma Spray
BUAA	Beihang University
EBSD	Electron Back - Scattered Diffraction
GZO	gadolinium zirconate
LCO	$La_2Ce_2O_7$
LTE	Local Thermodynamic Equilibrium
LPPS	Low Pressure Plasma Spray
LZO	$La_2Zr_2O_7$
MHD	Magneto Hydrodynamic
OES	Optical Emission Spectroscopy
Oh	Ohnesorge Number
PS - PVD	Plasma Spray - Physical Vapor Deposition
Pr	Prandtl Number
SD	Spraying Distance
STDEV	Standard Deviation
Sh	Sherwood Number
SLPM	Standard Liter Per Minute
SPS	Suspension Plasma Spraying
NCE	Non-Chemically Equilibrium
NEC	Net Emission Coefficient
Nu	Nusselt Number
We	Weber Number
XJTU	Xi'an Jiaotong University
YSZ	Yttria-Stabilized Zirconia

[5]. Therefore, the original particle size of the feed powder, method of injection, in-flight particle velocity and temperature, and interaction between the particles and plasma plume at a given distance, which affect the microstructure of the products, determine the properties of the coatings synthesized through multi spraying. Plasma spraying methodologies such as suspension plasma spraying technology (SPS), atmospheric micro plasma spraying technology (AMPS), and atmospheric laminar plasma spraying technology (ALPS), in which suspension powder, novel hollow cathodes, and ultralong plasma jets are used, respectively, have been designed considering the processing and material property relations.

Different applications require different material performances, properties, and microstructures [6]. For example, yttria-stabilized zirconia (YSZ) has been widely used as a top coating for thermal barrier coatings and as an electrolyte layer in solid oxide fuel cells (SOFCs) [7]. When it is used as a thermal barrier coating, the formation of abundant pores within the material is often desired to decrease the thermal conductivity and improve the thermal barrier effect in YSZ. In contrast, when used as an electrolyte for SOFCs, the YSZ coating must be sufficiently dense to achieve high gas tightness and high ionic conductivity [2,8]. Coatings based on a mixture of Mo (melting point: 2620 °C) and its oxides are widely used in industrial applications owing to their excellent wear resistance. Moreover, molybdenum oxide, which has high hardness, can serve as a solid lubricant to reduce the coefficient of friction between components during the wear test [9]. These Mo-based mixtures are produced by the oxidation of in-flight pure Mo particles during spray processing. By changing the spraying parameters, Mo-based coatings with different microstructures can be obtained.

Nevertheless, the oxidation of metallic coatings can be observed throughout the atmospheric plasma spraying process. As such, a low pressure (10^4–10^5 Pa) plasma spraying method (LPPS) was proposed for the large-scale deposition of metallic coatings, such as Al, Cu, Ti, and Ni-based alloys. Based on LPPS technology, a very low-pressure (50–200 Pa) plasma-induced physical vapor deposition (PS-PVD) technology using a high-input powder plasma torch was employed to produce ceramic coatings with a unique quasi-columnar structure (Fig. 1-t to 1-w).

1.2. Fundamentals, equipment, and operating parameters of the arc plasma torches

An electric arc with a temperature of the order of 10^4 K can be transferred to a workpiece through arc additive manufacturing, arc welding (Fig. 2-a), and plasma cutting, or deposited on the surface through plasma spraying. A plasma spray system contains different subsystems. The core part is a plasma torch (or plasma gun) that generates a high-energy plasma plume in either an atmospheric or a reduced-pressure environment. In a direct-current nontransferred arc plasma torch, an electric arc is generated between the conical cathode and anode nozzle (Fig. 2-b, 2-c) [34]. The cathode and anode are typically placed in a linear scheme. Hence, the heat transfer and flow characteristics of the arc are determined by the channel structure of the torch, composition of the working gas and its flow rate, input current, and internal surface roughness of the electrodes.

Typically, the plasma torch for the APS process is operated at an output power ranging from 25 to 150 kW and a higher gas flow rate (usually ≥30 SLPM) than those of arc welding torches [21,22]. At atmospheric pressure, entrainment from the surrounding air to the plasma jet occurs immediately, which reduces the length of the plasma jet (≤250 mm) owing to the formation of eddies, swirls, and other flow instabilities [23–25,46].

A supersonic plasma spray torch was designed using a Laval-type nozzle (Fig. 2-d) instead of a conventional cylindrical nozzle as the anode. The torch was composed of a convergent inlet, a narrow throat, and a divergent outlet. The Laval nozzle can change the flow characteristics from subsonic to supersonic by modifying the nozzle area and, in turn, the flow speed. An internal feedstock injection mode is typically employed to provide more favorable conditions for particle melting and acceleration during plasma spraying.

The arc voltages of the plasma torches are typically quite low, indicating that the electrical conductivity of the arc column and the corresponding number density of the plasma species are also lower (Table 1). For pure Ar, mixed Ar/H_2, and $Ar/He/H_2$ plasma gases, the plasma temperature increases with increasing plasma number density (Fig. 3) [10,26]. Therefore, the design of the conventional plasma torch was optimized to extend the arc column by limiting the arc axial movement using a forced constricted-type torch channel. Plasma torches using the optimized design show increased arc voltages.

Forced constricted structures are used as auxiliary electrodes between the cathode and the anode. Auxiliary electrodes, which are also called neutrodes or interelectrodes, are used with or without insulation, depending on the application requirements [31,36]. To date, commercial plasma torches with a cascaded anode, such as Triplex, Mettech Axial III, C + Plasma, HE100, and Plazjet, have been presented [35,36]. Using a cascaded structure, the enthalpy of the plasma jet can be increased without the using of molecular gas (i.g., H_2) in some cases (Fig. 2-e) [31]. The triplex plasma torch was developed at the University of the German Armed Forces in Munich (Germany) and commercialized by Sulzer Metco [31]. As shown in Fig. 2-f, three different arcs were generated by the three cathodes, which produced fixed arc attachment positions on the anode surface.

When these insulated electrodes were assembled with injections of vortex gas flow at the torch cross-sections, a laminar plasma jet with high thermal efficiency was designed for material processing (Fig. 2-f) [32]. Vortex gas flows can stabilize the plasma column inside a torch channel [32,37]. Moreover, an advanced cascaded arc plasma torch was

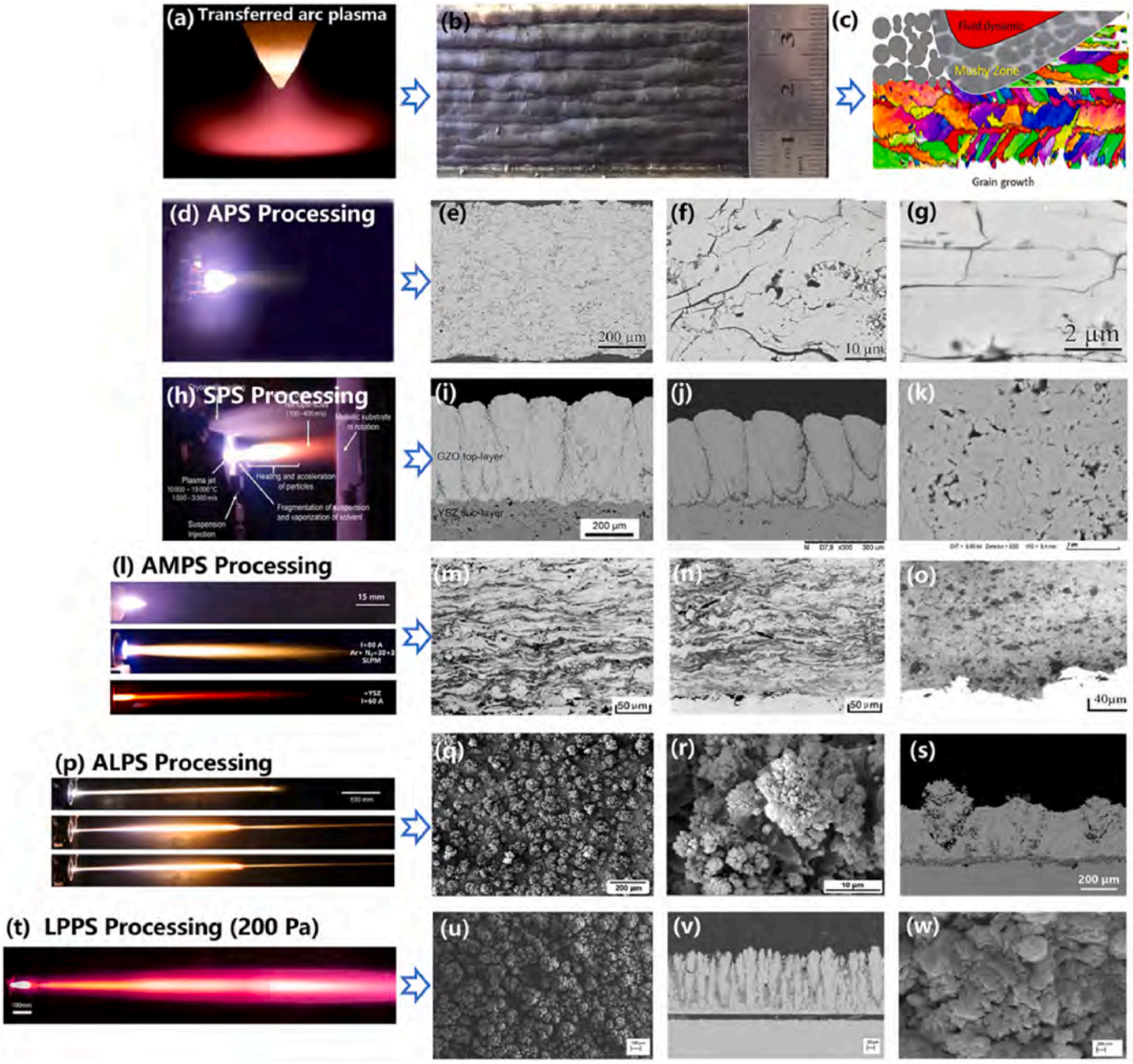

Fig. 1. (a) Transferred arc plasma processing [10]; (b) top surface view of alloys produced through arc-additive manufacturing [11]; (c) powder-bed additive manufacturing process [12]; (d) conventional atmospheric plasma spray processing (APS) [13] and (e–g) typical microstructures of/metallic ceramic coatings produced through APS [14,15]; (h) atmospheric suspension plasma spray processing (SPS) [16] and (i–k) typical microstructures of the coatings synthesized through atmospheric SPS [17,18]; (l) novel atmospheric micro plasma spray (AMPS) and (m–o) typical microstructures of AMPS-produced coatings; (p) atmospheric laminar plasma spray processing (ALPS) [19] and (q–s) typical microstructures of YSZ coatings produced through ALPS [20]; (t) low-pressure plasma spray (LPPS) processing and (u–w) typical microstructures of coatings [13] (Reproduced with permission © Springer Nature, IOP Publishing Ltd., & Elsevier B·V.).

designed and manufactured for plasma spraying and powder processing to precisely control plasma spray parameters, such as particle dwell time (flight time), particle temperature, and velocity, and to obtain a more stable plasma flow [33]. Plasma-sprayed coatings and powders produced through this highly reproducible methodology exhibit excellent properties and good homogeneity. In addition, When a trumpet-like anode was employed with auxiliary electrodes (Fig. 2-f), a long laminar plasma jet can be formed in the atmospheric environment [20,34].

Fig. 3-a and 3-b show the input current, arc voltage, and gas flow rate of some commercially available plasma spray torches. Currently, most plasma torches operate at high input currents and low arc voltages. In atmospheric environments, the first ionization of argon gas is Ar; the numerical density of Ar species, such as Ar^{+}, Ar^{++}, and Ar^{+++} varied significantly with increasing temperature (Fig. 3-c and 3-d). However, it is difficult to achieve an internal maximum temperature greater than 20,000 K using a water-cooled plasma spray torch and pure Ar gas. Therefore, gas mixtures are often used in plasma-spray torches. In addition, large deviations from the local thermodynamic equilibrium (LTE) are observed at the electrode wall (Fig. 3-e) [44]. Metal vapor from the electrodes considerably affects the properties of the arc column. To maintain the continuity of the electric current and energy flux density in theoretical modeling, thermal nonequilibrium sheaths are often used to simulate electrons and heavy species [26] (Fig. 3-f).

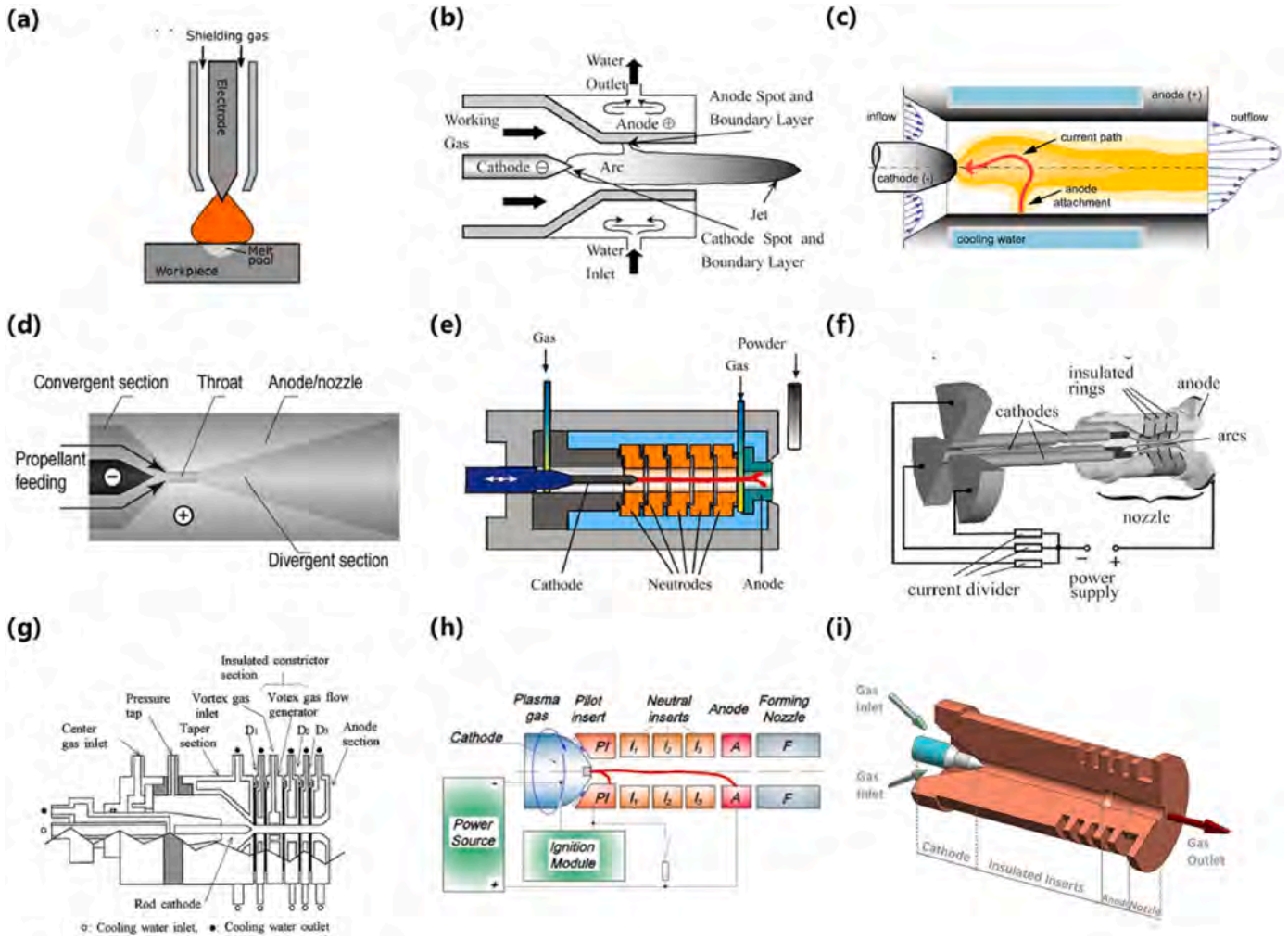

Fig. 2. Internal structures of the arc plasma torches: (a) a typical transferred arc plasma gun used in welding [26]; (b) schematic diagram of a direct current nontransferred arc plasma torch [27]; (c) arc flow inside a linear scheme plasma torch [28]; (d) internal structures of a supersonic arc plasma torch [29]; (e) schematic of a plasma spray torch with inserted neutrodes developed in 1968 [30,31]; (f) schematic of a commercial Triplex plasma torch with multielectrodes by the Sulzer Metco company [31]; (g) forced constricted-type arc plasma torch with a vortex gas injection nozzle [32]; (h) schematic of an advanced cascade arc plasma torch for plasma spraying and powder processing [33]; (i) arc plasma torch that can generate long laminar plasma plumes [34] (Reproduced with permission © Bentham Open, IOP Publishing Ltd., & Elsevier B·V.).

Table 1
Operating parameters of commercial direct current plasma spraying torches.

Business Name	Plasma Gas	Total Flow Rate (SLPM)	Input Current (A)	Maximum Power (kW)	Powder Feed Rate	Reference
Metco 9MBM Plasma Gun	Ar, Ar/H_2, or Ar/He	60	400	50	38 g/min Cr_2O_3	[38]
Metco SinplexPro Plasma Gun	Ar, Ar/H_2, or Ar/He	50–200	100–540	60	76 g/min Cr_2O_3	[39]
Metco F4MB Torch	Ar, Ar/H_2,	60	500–800	55	60 g/min Cr_2O_3	[47]
Metco TriplexPro 210 Gun	Ar, Ar/N_2 or Ar/H_2	200	450–490	65	60–180 g/min Cr_2O_3	[40]
Metco SinplexPro 03C Gun	Ar, Ar/H_2, Ar/He, or Ar/N_2	150–260	920–1200	130	/	[41]
Metco 03CP Gun	Ar/H_2, Ar/He	120	1600–2600	180	4–25 g/min YSZ	[42]
Praxair SG-100 Torch	Ar/H_2, Ar/He	40–60	450–800	80	/	[43]

Arc plasma torches yield high output enthalpies when operated at high arc voltages. Nevertheless, the arc attachment position inside the plasma torch is dominated by the balance between aerodynamic drag and electromagnetic forces (Fig. 4-a). The electromagnetic force generates positive or negative angular momentum to form an attachment on the opposite side. However, the drag force of the arc causes a net angular momentum that favors the formation of a new attachment on the opposite side of the original attachment (Fig. 4-b). Hence, arc spots drift dynamically along the electrode surface in the near-electrode regions until local anode-material erosion occurs [45]. Furthermore, a cold boundary layer surrounding the arc was formed inside the plasma torch [45,46]. The thickness determines the movement of the arc attachment. Thicker boundary layers favor the induction of a re-strike mode of high voltage fluctuations during arc attachment, whereas thin boundary

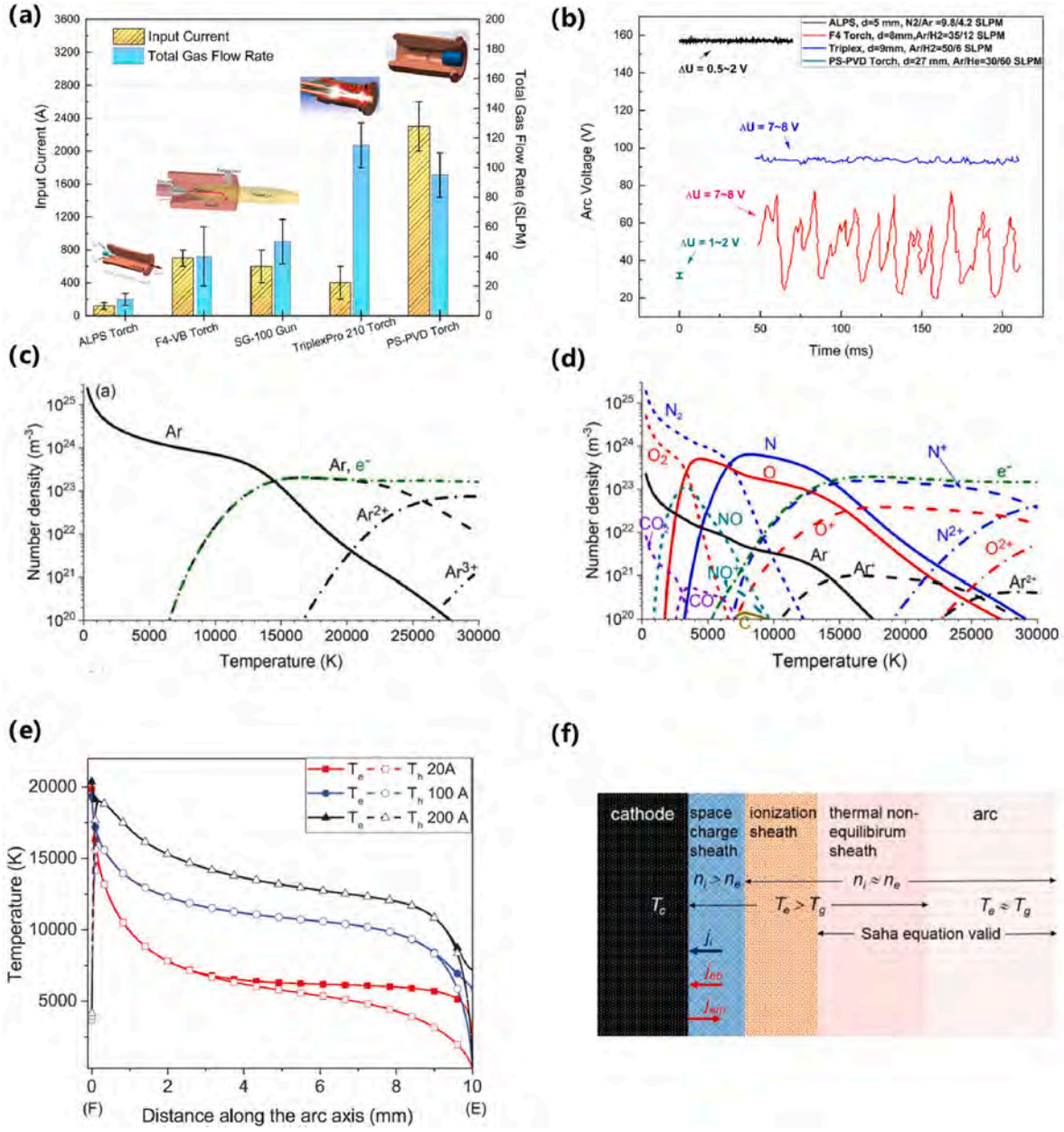

Fig. 3. (a) Input power and total gas flow rate of current plasma spray torches [13]; (b) time-dependent arc voltage variation of plasma spray torches [13]; number densities of argon (c) and air plasma species (d) as a function of temperature [26]; (e) electron (T_e) and heavy particle (T_h) temperature along the arc axis [44]; (f) sheath structures at the boundary layer of cathode of an arc [26] (Reproduced with permission © IOP Publishing Ltd & Elsevier B·V.).

layers prefer steady modes with very low voltage fluctuations [46]. For example, the potential of a conventional plasma gun produced at 65 V may fluctuate from 20 to 85 V in microseconds. Meanwhile, the potential of the Sinplex-Pro 03C spray gun fluctuates by only approximately 6 V [41]. Therefore, the instabilities and fluctuations in the properties of the plasma arc induce instabilities in the produced plasma jet and promote the entrainment of cold gas within the torch. In turn, plasma jet instabilities promote the development of turbulence, which reduces the controllability and reproducibility of the plasma-spraying process. The spraying procedure, which involves the heating and acceleration of the particles within the plasma jet, is discussed in the next section.

1.3. Multiphase flow characteristics of metallic and ceramic powders during plasma spraying

Industrial plasma spray technologies often employ external injection of the original powders into a plasma jet. The fluid dynamics of external injection processes typically involve cross and multiphase flows. The in-flight distance (spraying distance) substantially affects the properties of the coating because of possible variations in the particle velocity and temperature. In addition to solid particle melting, evaporation, and solidification in plasma spraying, the following phenomena will occur during the plasma spraying:

(1) Breakup and atomization of the liquid column near the torch nozzle.

After external or internal injection into the plasma jet, solid powders

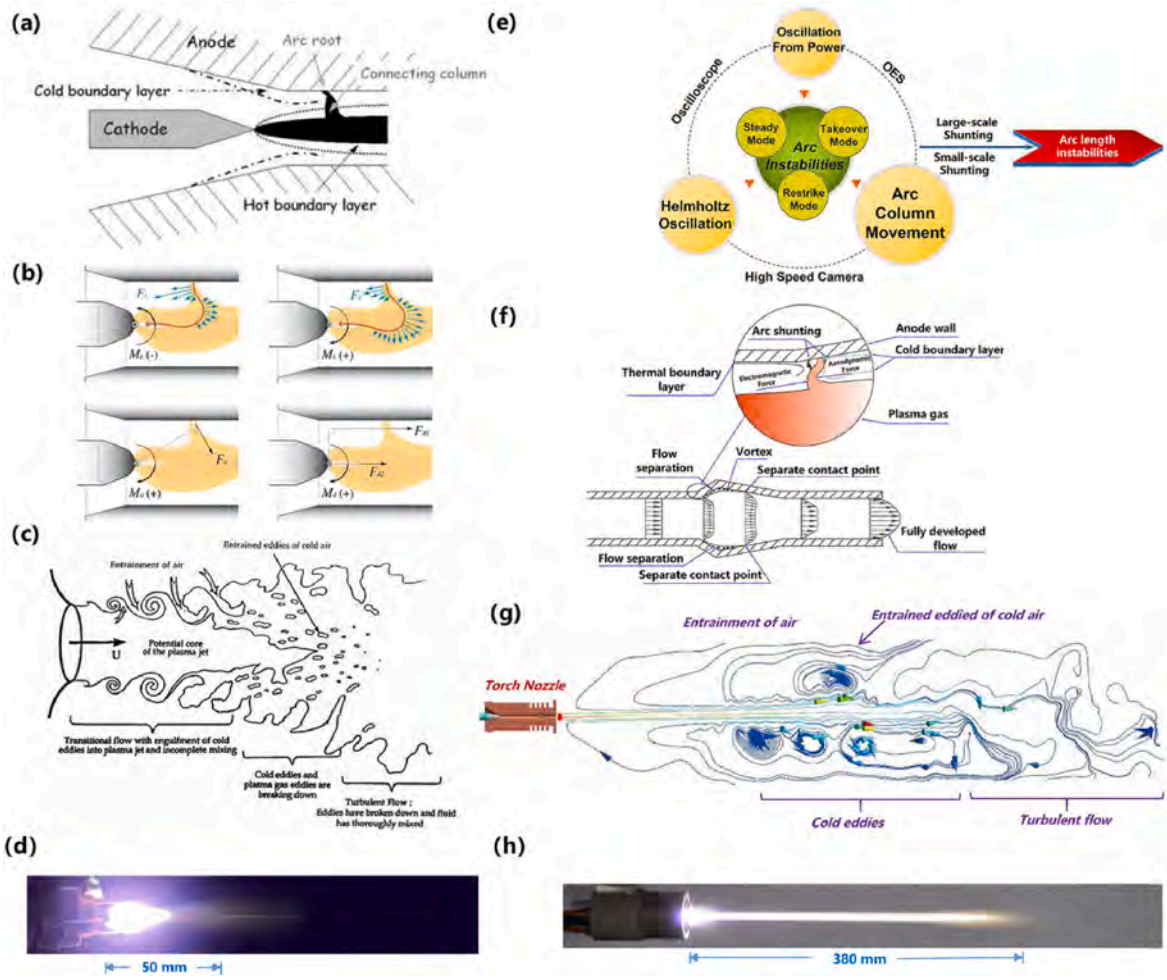

Fig. 4. (a) Effects of cold boundary layers on the generation of plasma jet inside the torch [47]; (b) mechanism of the reattachment process of the arc column inside the torch [48]; (c) regions of cold gas entrainment into an atmospheric plasma jet [49]; (d) experimental observation of a conventional atmospheric plasma jet (I = 550 A, 45 SLPM Ar); (e) formation of arc instabilities inside the torch; (f) effects of fluid characteristics on the arc movement inside the laminar plasma spray torch; (g) regions of cold gas entrainment into the novel atmospheric long laminar plasma jet; (h) experimental observation of the atmospheric long laminar plasma jet (I = 160 A, 9.8 SLPM N_2 + 4.2 SLPM Ar) [34] (Reproduced with permission © Springer Nature., IOP Publishing Ltd., & Elsevier B·V.).

initially melt into the liquid column, liquid bag, and droplets near the torch nozzle [50]. Plasma jets exhibit highly turbulent characteristics near the torch nozzle. Thus, the multiphase fluids near these regions undergo atomization. In SPS or SPPS processing, the cross-sectional aerodynamic drag force of the plasma plume rapidly breaks the liquid column. The plasma plume shockwaves in LPPS or PS-PVD also drive the local atomization of the liquid column and droplets.

(2) Vaporization and resolidification of the in-flight particles

In general, the droplets vaporize at temperatures greater than or equal to the boiling point of the liquid column. However, the surface molecules of these droplets may still vaporize at temperatures below their boiling point. This implies that heating vaporization ($Q_{conv} + Q_{rad} > Q_{vap}$), isothermal vaporization ($Q_{conv} + Q_{rad} = Q_{vap}$), and cooling vaporization ($Q_{conv} + Q_{rad} < Q_{vap}$) occur depending on the local conditions of the plasma spray [13,51], particularly at different spraying distances employed in ALPS and LPPS.

In LPPS (10^3–10^4 Pa) and PS-PVD (50–200 Pa), flash vaporization of the feed powders typically occurs because of the large pressure gradient between the plasma torch and plasma jet areas [52,53]. Conversely, resolidification of droplets has been extensively observed in APS processing. For example, at a constant input power, spherical particles were deposited on the substrate as the spraying distance increased from 80 to 120 mm during the plasma spraying of metallic powders. The resolidified spherical particles exhibited low adhesive strength on the substrate and were typically porous. Hence, resolidified particles are inevitably formed at the interspaces of the quasi-column structure when a large spraying distance is employed in LPPS and PS-PVD.

(3) Non-line-of-sight deposition of coatings due to self-shadowing effect of impinging particles.

At the velocity boundary layer of the substrate with a planar or double airfoil shape, impinging particles, including droplets, resolidified droplets, or solid particles, will suffer a self-shadowing effect during plasma spraying. The self-shadowing effect is a crucial consideration for the deposition of quasi-columnar thermal barrier coatings based on YSZ, GZO, or LCO through ALPS, SPS, and PS-PVD processing. This effect promotes the perpendicular growth of coatings rather than their horizontal growth. The fluid mechanisms involved in the self-shadowing effect are related to the different tangential velocities of the impinging particles of different sizes. Hence, only a mass of nanosized original feed powders (e.g., $D_{50} = 10$ μm) can induce an apparent shadow effect under a low feed rate during the deposition of quasi-columnar YSZ coatings in ALPS or PS-PVD.

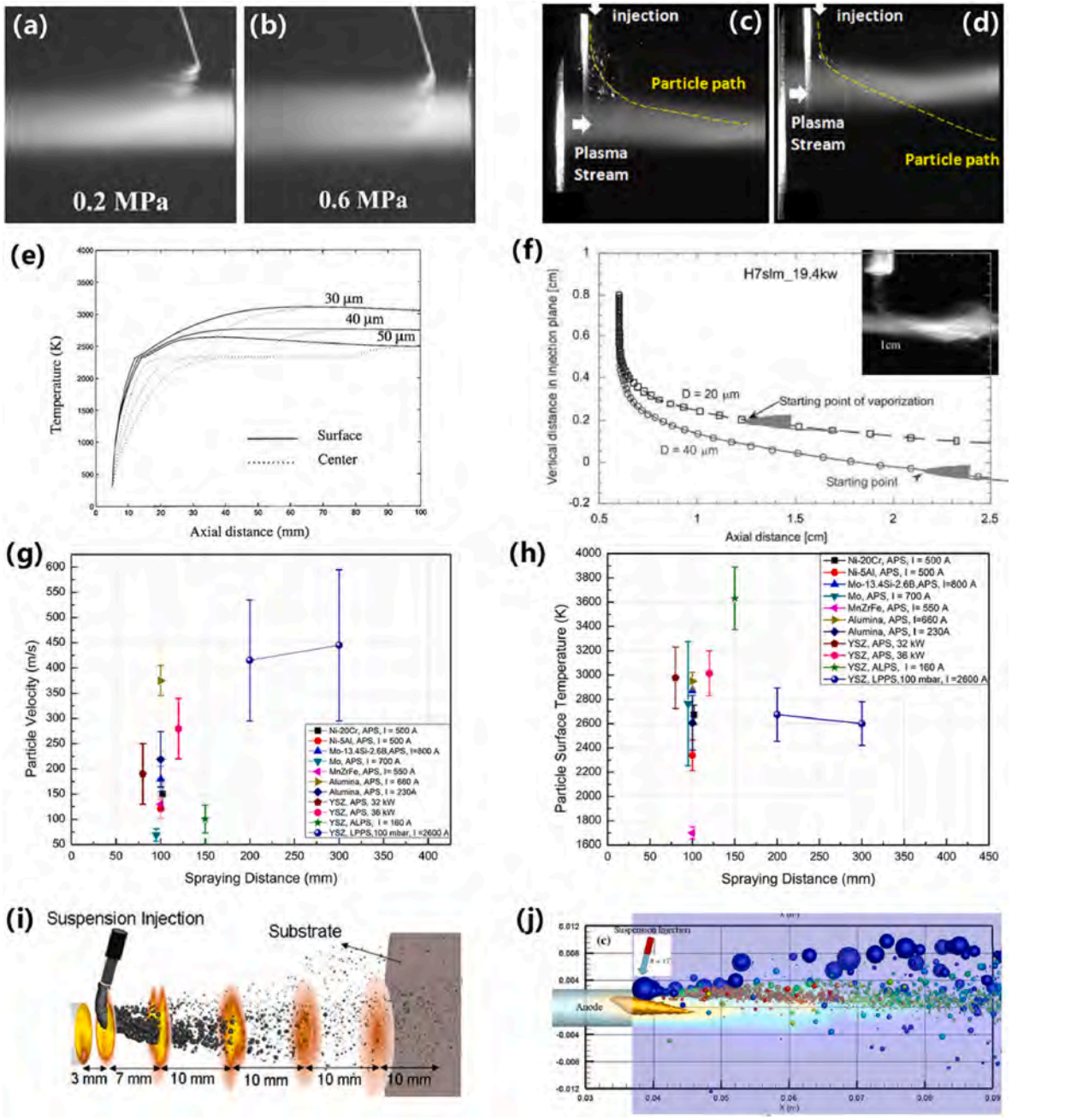

Fig. 5. (a) Experimental observation of atmospheric suspension plasma spraying (I = 550 A, 45 SLPM Ar+ 15H_2) at an injection pressure of 0.2 MPa (a) [55] and 0.6 MPa (b) [55]; (c) particle penetration path by carrier gas in plasma spraying [56]; (d) over-injected condition of particle penetration path in plasma spraying [56]; (e) calculated surface and core temperature of alumina particles in APS [57]; (f) modeling trajectories and locations of molybdenum particles during APS [58]; (g) experimental measurement of particle velocity and (h) surface temperature at different spraying distances; (i) modeling distributions of suspension injection and cross-sections of plasma jet [59]; (j) modeling of particle flows through suspension injection in SPS [60].

(4) Absorption and deposition of the atoms from the vapor stream to the substrate

Currently, plasma spraying cannot be achieved via full-vapor deposition. This process usually involves the deposition of multiphase mixtures composed of particles produced after 1) vapor condensation, 2) resolidification particles, and 3) secondary breakup nanoscale droplets [54], where 2) and 3) mutually transform in flight. From the experimental observations, a localized high-concentration vapor stream was formed at the center of the plasma jet as the jet impinged on the substrate during the PS-PVD processing. Moreover, multi-atom nanoclusters are formed on the substrate and then undergo surface diffusion, migration, coalescence, or even disappear (covered by subsequent deposition steps) on the substrate during the entire process.

Fauchais et al. (2006) observed a transverse cross-flow between the feed particle suspension and plasma jet near the torch nozzle (Fig. 5-a and 5-b) [55]. At a spraying distance of 15 mm, the injection pressure and suspension flow angle affect the heating profiles of the feed particles. The fragmentation (breakup) time was almost two orders of magnitude longer than the vaporization time. The suspension droplets initially break up and then vaporize. Similarly, Sampath et al. (2011) revealed poor penetration of the carrier gas achieved during SPS, where the particle track paths deviated from the hotter zone area of the plasma jet in Fig. 5-c and 5-d [56].

Table 2
Spraying parameters that comparing in Fig. 5-g and 5-h.

Business Name and Method	Output Power	Gas Flow Rate	Powder Size (μm)	Spraying Distance (mm)	Ref.
Mo-13.4 Si-2.6 B by SG-100 Torch	I = 800 A	40 SLPM Ar +10 SLPM He	20–53	100	[61]
Ni-5 wt.%Al by Sulzer PT F4 Torch	I = 500 A	50.5 SLPM Ar + 8 SLPM H_2	11–45	100	[62]
Mo by APS	I = 700 A	85 SLPM Ar	45–90	90–100	[63]
MnZrFe (MnZn Fe_2O_4) by APS, 7 MB plasma torch (Suzler Metco Inc., NY, USA)	I = 466–550 A	47 SLPM Ar + 0.5 SLPM H_2	25–95	100–130	[64]
Ni-20 Cr by APS Triplex Pro200 Torch	I = 500 A	20 SLPM Ar+ 20 SLPM He	5–45	102	[65]
Alumina by Sulzer F4VB Torch	I = 660 A	49 SLPM Ar +12 SLPM H_2	15–35	100	[66]
Alumina by Axial III plasma torch	I = 230 A	150 SLPM N_2	26–66	100	[67]
YSZ by Sulzer F4VB Torch	I = 600 A	45 SLPM Ar + 15 SLPM H_2	10–45	120	[68]
YSZ by Sulzer F4VB Torch		Ar (45 SLPM) + H_2 (15 SLPM)		120	[69]
YSZ by LPPS (20,000 Pa)	125 kW	50 SLPM Ar + 110 SLPM He	1–30	300	[70]
YSZ by LPPS (500–15,000 Pa)	15 kW	40 SLPM Ar	45–75	150–560	[71]
YSZ by ALPS	I = 160 A	9.5–14 SLPM (70% N_2 + 30% Ar)	1–30	50–550	[90]

Coddet et al. (2003) calculated the surface and core temperatures of alumina particles during APS [57]. Regardless of the particle size and at the same injection velocity, the temperatures of the surface and core of the Al_2O_3 particles were different. Only the particles with a diameter of 30 μm were fully molten at a spraying distance of 50 mm. Wang et al. (2001) modeled the evaporation of molybdenum particles during APS by considering noncontinuum effects. Smaller particles evaporate earlier than larger particles because of the higher evaporation rates and larger mass transfer coefficients. These results provide a comprehensive understanding of the rapid heat and mass transfer processes during APS, and the theoretical calculations agree well with the experimental results. Previously reported models commonly study the axial variations of the velocity and temperature in a steady flow and two-dimensional domain. To verify the computational results, experimental measurements were performed using a commercial DPV-2000 particle diagnostic system. It is worth noting that the measured temperature in the DPV-2000 can be understood as the particle surface temperature according to its two-wavelength detection mechanism.

Fig. 5-g and 5-h show the particle velocity and surface temperature distributions of Ni-60, Ni–5Al, Mo, MnZrFe, Al_2O_3, and YSZ powders as a function of the spraying distance. The results from these figures are summarized in Table 2. The particle flow was distributed over a larger area at the cross-section of a constant spraying distance. Apart from the particle injection parameters and plasma spray torch power, the particle density due to gravity affects the heating profiles of the particles. This has been proven in particular for Mo-based materials and alumina particles. Therefore, it is difficult to simultaneously improve the particle velocity and temperature by increasing the plasma torch power during conventional APS processing.

Recently, computational studies on plasma spraying have been carried out in the three-dimensional domain by emulating multisized particles and modeled more closely to realistic conditions. Dalir et al. (2018) developed a model to simulate droplet atomization during the SPS process (Fig. 5-i and 5-j), wherein it was shown that the number of evaporated particles increased with a decrease in the liquid core length [59,60]. In-flight droplets with low velocities cannot penetrate the high-temperature plasma jet owing to the incomplete evaporation of the solvent.

These three models were used to calculate and simulate the heating and motion of particles during plasma spraying:

1) single particle model;
2) limited particle model;
3) statistical particle model.

It is commonly assumed that the droplets are spherical in plasma spraying. As shown in Fig. 6, Westhoff et al. (1992) proposed a two-dimensional model for the calculation of plasma–particle interactions during APS (Fig. 6). This model, which has been used since its proposal, considers realistically complex conditions and provides a comprehensive understanding of the behavior of particles in a plasma jet. This model has been used for several years. Li et al. (2018) used this model to investigate the properties of NiCr particles with Mo-based shells during APS (Fig. 6-b). The surface and core temperatures of these specially designed particles were evaluated and their effects on the properties of the deposited coatings were demonstrated. Similarly, Vardelle et al. (2003) revealed the hill vortex phenomenon in Fe particles during APS, which was induced between the kinetic viscosity of the plasma gas and the particles (Fig. 6-d).

In particular, the SPS procedure involves a series of more complex phenomena between the particles and the plasma plume, such as atomization, breakdown (or breakup), evaporation, sintering, melting, and impacting (Fig. 6-c), than APS processing. SPS has been employed to produce quasi-columnar or vertical-crack ceramic thermal barrier coatings [72,73]. However, the size of the injected particles usually ranges from 300 to 900 nm because the deposition rate during SPS is lower than one-third of that during APS [144].

In addition, in-flight particles may resolidify and freeze during plasma spraying (Fig. 6-e), which promotes partial or full droplet solidification, particularly during APS or LPPS wherein a larger spraying distance is employed. Consequently, the coating may contain spherical particles at the top surface and/or at the interspace of the quasi-column structure. Typically, the resolidification particles often exhibit poor adhesion to the substrate. In PS-PVD, resolidification deposition should be avoided, and vapor concentration should be enhanced.

In fact, during the initial stage, when the particles are injected into the plasma jet, heat is transferred through convection and conduction. This is demonstrated by the increase in the particle temperature (Fig. 6-f), which in turn improves the radiation heat transfer. However, the total in-flight time of the particles during plasma spraying is usually quite low. For APS and LPPS, the in-flight time ranges from $1e^{-4}$ to $1e^{-3}$ s and 0.1–0.4 s, respectively. Therefore, the temperature gradient within a single particle is often considered negligible during the modeling and simulation of fine particles. However, the temperature gradient must be considered for large particles and core–shell composites.

Almost all the previously mentioned phenomena occur during LPPS and PS-PVD performed at large spraying distances (Fig. 6-g). In particular, the intensive backflow between the plasma plume and chamber wall promotes the deposition of coatings on the internal chamber surface and decreases the deposition rate on the prepared substrate. Moreover, secondary and/or multibreakup of in-flight droplets may occur, which further decreases the sizes of the deposition unit,

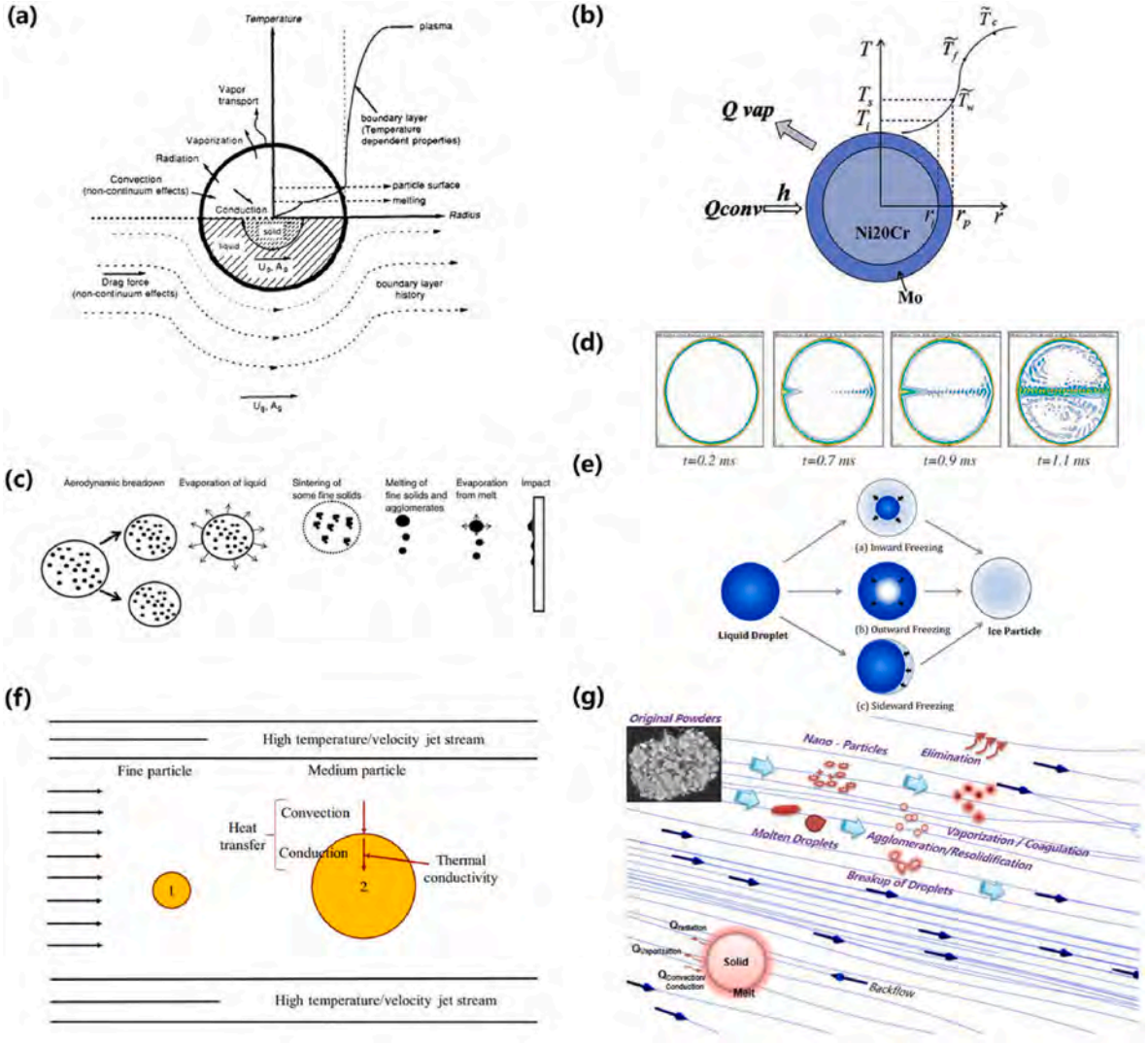

Fig. 6. (a) Schematic illustration of particle heat, mass, and momentum transfer in plasma gas [74]; (b) model of the shell–core structure powder during APS [75]; (c) heating and motion histories of a suspension droplet during APS [76]; (d) modeling of the convective movement by a Hill vortex within an iron particle (60 μm) [77]; (e) resolidification of the in-flight particles during spray processing [78]; (f) heating transfer in the in-flight particles in the thermal spray jet stream [79]; (g) heating and motion histories of the nano-agglomerated YSZ powders in the low-pressure plasma jet [13].

particularly in the plasma shock area.

Therefore, on a large scale, the mass transfer regions during plasma spraying can be divided into dense, mixed, and dilute areas (Fig. 7-a). The differences between these regions are mainly induced by the aerodynamic force from the plasma jet on the in-flight particles (Fig. 7-b); a relative velocity exists between the plasma jet and the particles. Fig. 7-e shows the formation mechanism of the droplet from the liquid column, which is driven by the difference between the transverse and perpendicular velocities, particularly in cross-flows that involve the external injection of particles. Chen et al. (2013) and Opfer et al. (2014) investigated this phenomenon, and the results of their work are shown in Fig. 7-c and Fig. 7-d, respectively.

Furthermore, in plasma spraying, the self-shadowing effect of the impinging particles occurs at the velocity boundary layer of the substrate. The intense shadowing phenomenon during the entire spraying process contributed to the deposition of quasi-columnar ceramic coatings through SPS, ALPS, and PS-PVD. For electron beam physical vapor deposition (EB-PVD), the shadowing effect from vapor flow is a critical consideration for the deposition of the columnar-structured coating (Fig. 7-f). Generally, the formation mechanism involving the shadowing effect is described using the Stokes number. If the Stokes number of an impinging particle is less than 1, the tracked trajectories of this particle will bend; hence, the particle will flow away from the substrate (Fig. 7-g, 7-h). Finally, a quasi-columnar structure is induced on the substrate. Studies on the self-shadowing effect at the velocity boundary layer of different substrates are presented in more detail in Sections 4 and 5.

The use of micro and nanosized powders for plasma spraying has been extensively studied owing to the possibility of producing coatings with unique microstructures and excellent properties. Shinozawa et al. (2017) produced a unique feather-like YSZ coating using LPPS (Fig. 8-a). The porosity of the coating was greater than 50% and its thermal conductivity at room temperature was approximately 0.5 W/(m K) [89]. Zhang et al. (2019) produced a cauliflower-like Mo coating using ALPS. The formation mechanisms of the coatings synthesized via plasma-induced PVD are presented in Fig. 8. Zhang et al. (2016) proposed an island growth model for coatings produced through PS-PVD, wherein homogeneous nucleation at the end of the plasma jet was achieved under a lower average coverage (Fig. 8-f). Song et al. (2019) used PS-PVD composed of fine grains, splats, and unmelted particles (Fig. 8-d), which was similar to the results of Guo et al. (2016) (Fig. 8-g). In addition, Racek et al. (2010) demonstrated the potential growth of island protrusions on the coating surface owing to the impingement of

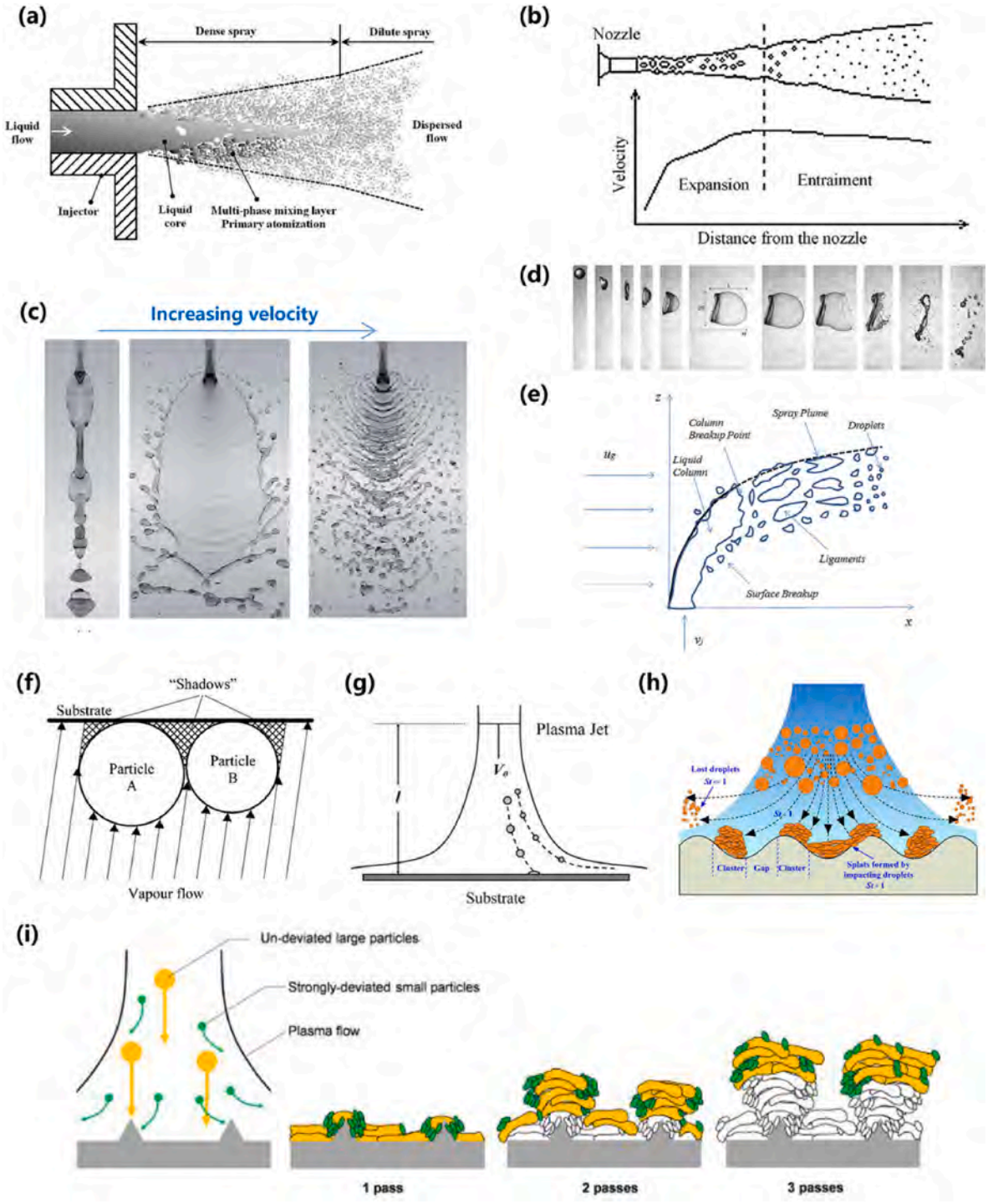

Fig. 7. (a) Schematic of the spray structure in the atomization region [80]; (b) expansion and entrainment areas with the increasing center velocity of a spray jet [81]; (c) jet flow patterns at increasing flow velocities [82]; (d) typical evolution of a single bag breakup of water in an airflow [83]; (e) liquid column and spray plume regions when a jet penetrates a cross-flow [84]; (f) shadowing zones in the vicinity of two particles during the EB-PVD process [85]; (g) predicted flow paths of in-flight particles with different size during APS process [86]; (h) motion trajectories of the droplets on the surface of a substrate during LPPS process [87]; (i) formation of a columnar -structured of coating during SPS [88].

high-speed particles on the substrate (Fig. 8-e), which revealed the possibility of producing quasi-columnar structures through LPPS or PS-PVD.

In PS-PVD processing, mixture deposition commonly occurs. By contrast, full vapor deposition can be achieved through EB-PVD processing, wherein a stable cluster is produced from the incoming vapor stream of the plasma jet or through surface diffusion on the substrate (Fig. 8-h). Considering a larger scale, coalescence and coverage of clusters may occur during the process. Combined with the shadowing effect of the impinging particles, the local growth rate in the perpendicular direction was considerably higher than that in the horizontal direction.

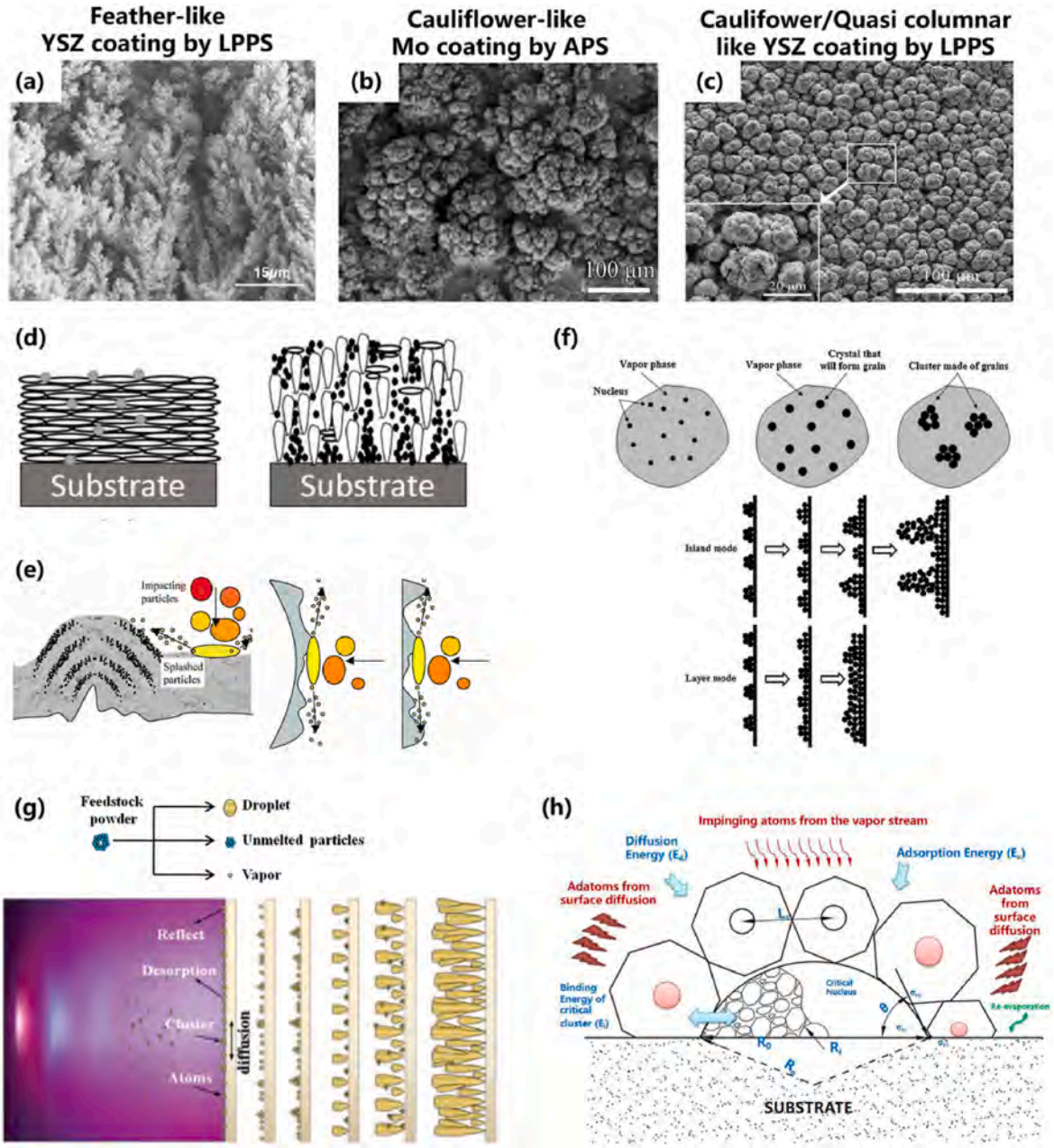

Fig. 8. Formation of vapor-deposited coatings during the plasma spraying: (a) feather-like YSZ coatings through LPPS (P = 66,661 Pa) [89]; (b) cauliflower-like Mo coating through ALPS [90]; (c) cauliflower-like or quasi-columnar like YSZ coating through PS-PVD (P = 200 Pa) [13]; (d) schematic of the deposition mechanism of the quasi-columnar coatings in a LPPS [91]; (e) formation of island protrusions from impinging particles on the top of the coating [92]; (f) island and layer growth modes of YSZ coatings produced through PS-PVD [93]; (g) growth of a quasi-columnar coating produced through PS-PVD [94]; (h) schematic of surface diffusion and vapor deposition of a stable cluster on a substrate during PS-PVD [13].

1.4. Industrial applications of arc plasma spraying

Thermal spraying technology is widely used for the production of aerospace materials (34%), industrial gas turbines (24%), and automobile components (16%) [1,3]. It is also a cutting-edge technology for improving the service lives of alloy parts of military equipment. Using arc plasma spraying technology, almost all metals used for industrial applications can be melted to produce coatings with thicknesses ranging from 20 μm to several millimeters. This technology features a higher deposition rate and broader applicability than electroplating and chemical vapor deposition (Fig. 9).

Evidently, the microstructure and properties of the produced coatings are affected by the particle heating and motion profiles achieved during the spraying process. Porous coatings can be manufactured through a mass of semi-molten droplets in an atmospheric environment. Dense ceramic or metallic coatings are usually produced in low-pressure environments because of the high particle velocities and low oxygen concentrations under such conditions.

In Section 2, we discuss a conventional APS technology using the internal injection of powders, and demonstrate the significant influence of cold carrier gas on the thermal plasma jet in plasma spraying, as well as the effects of heat transfer from the surrounding cold air to the plasma jet in an atmospheric environment. In Section 3, we introduce a AMPS, which uses a hollow cathode of carrier gas and model the particle heating and motion in AMPS processing. In Section 4, the deposition process of ALPS is studied, and the microstructural evolution, coating

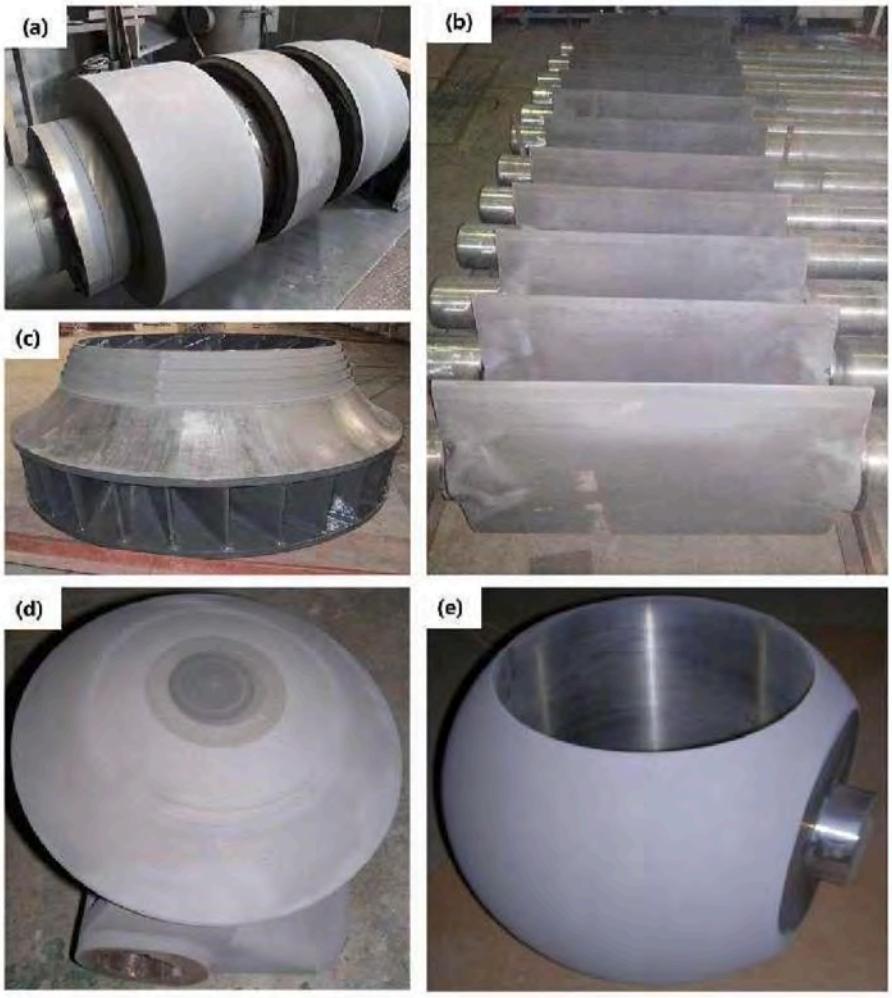

Fig. 9. Industrial applications of sprayed components: (a) rotor spindle for gas turbine engine; (b) guide vane for hydropower stations; (c) turning wheel; (d, e) ball valve and its spool.

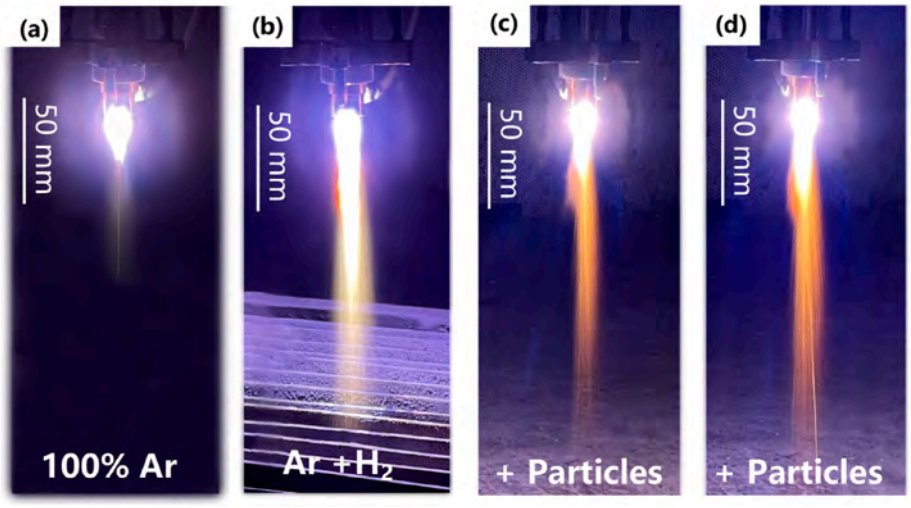

Fig. 10. (a) Experimental observation of the atmospheric plasma jet (I = 550 A, 45 SLPM Ar); (b) atmospheric plasma jet using argon (45 SLPM) and hydrogen gases (6.5 SLPM); (c, d) plasma jet with particles.

Table 3
Comparison of gas density, kinetic viscosity, thermal conductivity, and electrical conductivity that used in plasma spraying [98–102].

Property		Dry Air	nitrogen	Argon	helium	oxygen	hydrogen
Density(kg/m^3)	500 K	0.702	0.683	0.973	0.0976	0.779	0.0486
	10,000 K	0.172	0.0167	0.0476	0.0048	0.0191	0.0012
Kinetic viscosity (kg/(m s))	500 K	2.71×10^{-5}	2.45×10^{-5}	3.42×10^{-5}	2.89×10^{-5}	2.98×10^{-5}	1.21×10^{-5}
	10,000 K	2.45×10^{-4}	2.38×10^{-4}	2.69×10^{-4}	3.13×10^{-4}	2.86×10^{-4}	8.71×10^{-5}
Thermal conductivity (W/(mK))	500 K	0.0414	0.0386	0.0267	0.226	0.0421	0.258
	10,000 K	1.71	1.68	0.644	2.43	1.37	3.73
Electrical conductivity (A/(V m))	500 K	0	4.78×10^{-25}	3.07×10^{-23}	2.92×10^{-24}	8.21×10^{-24}	1.63×10^{-24}
	10,000 K	2705.5	2640.9	2990.0	41.74	3060.2	1927.8

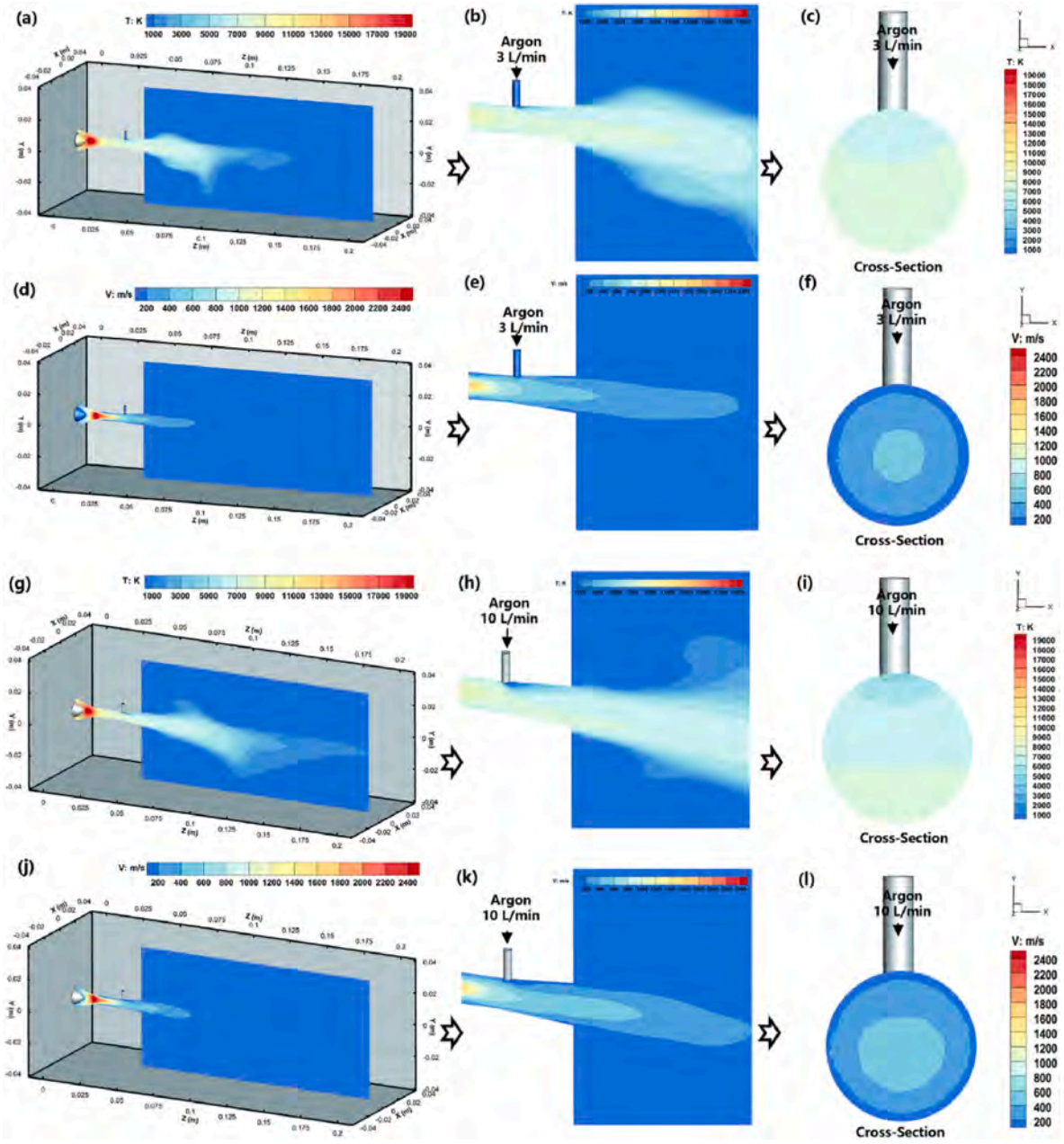

Fig. 11. Numerical investigation of the influence of cold carrier gas to plasma gas: plasma gas temperature (a), (b), (c), and velocity (d), (e), (f) distributions at the horizontal and cross-sections (3 SLPM argon). Plasma gas temperature (g), (h), (i), and velocity (j), (k), (l) distributions at the horizontal section (10 SLPM argon).

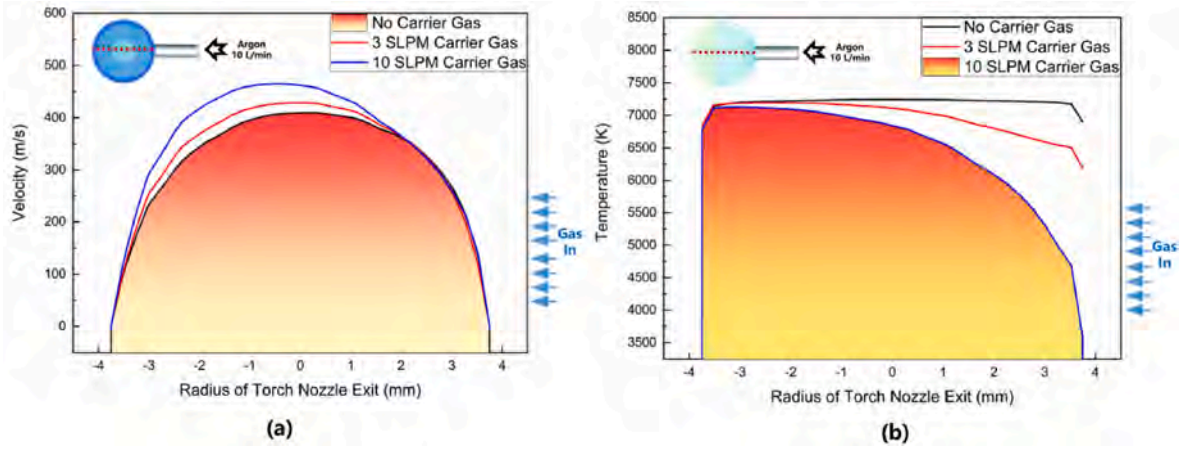

Fig. 12. Variations of plasma gas velocity (a) and temperature (b) at different carrier gas flow rates at the cross-section (center line) of the torch nozzle.

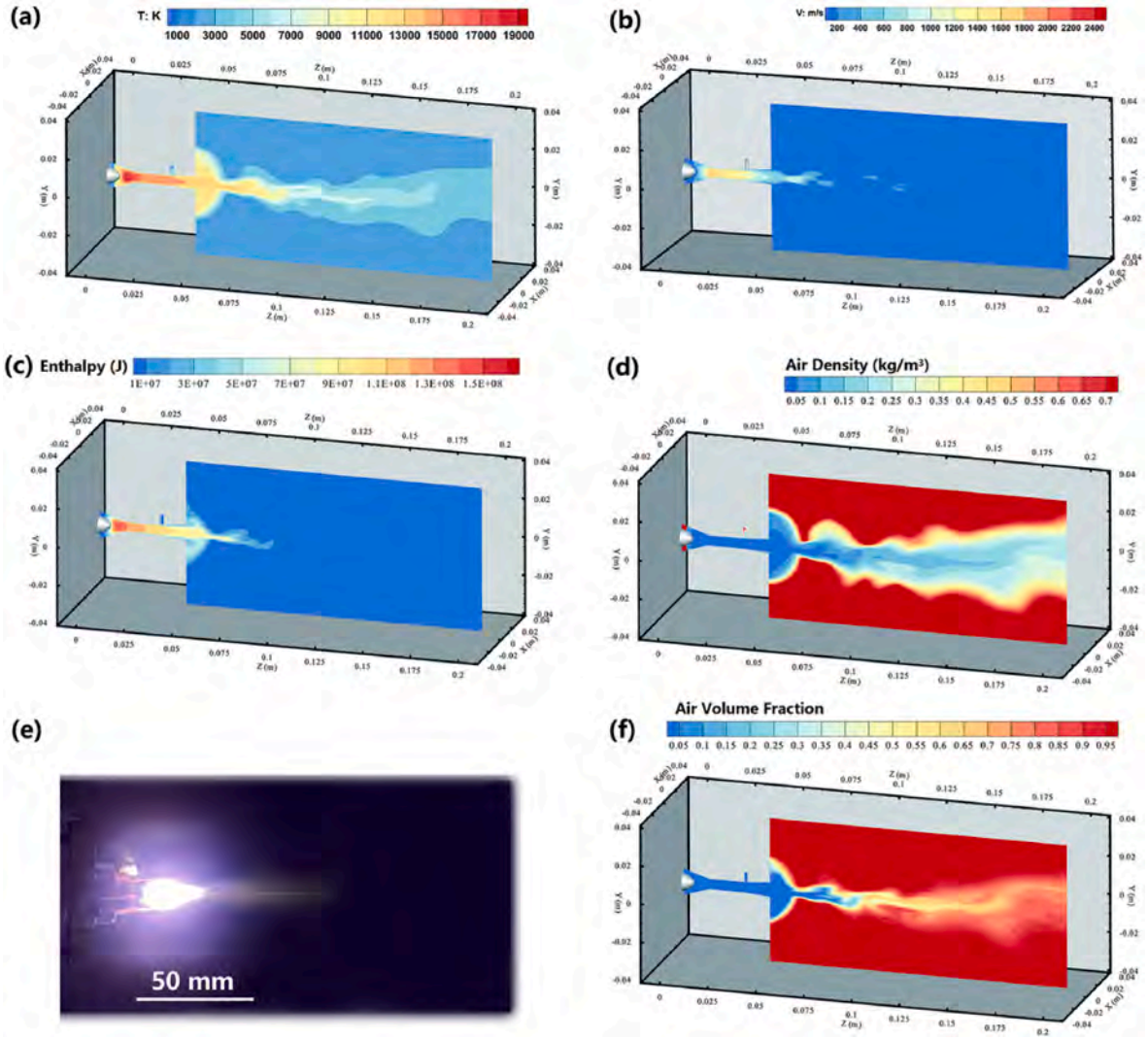

Fig. 13. Numerical investigation of the effect of surrounding air to the argon plasma jet in this work: (a) temperature; (b) velocity; (c) enthalpy, and (d) air density distributions of the surrounding air and argon plasma jet mixture; (e) experimental observation under the same conditions; (f) air volume fraction distribution (%).

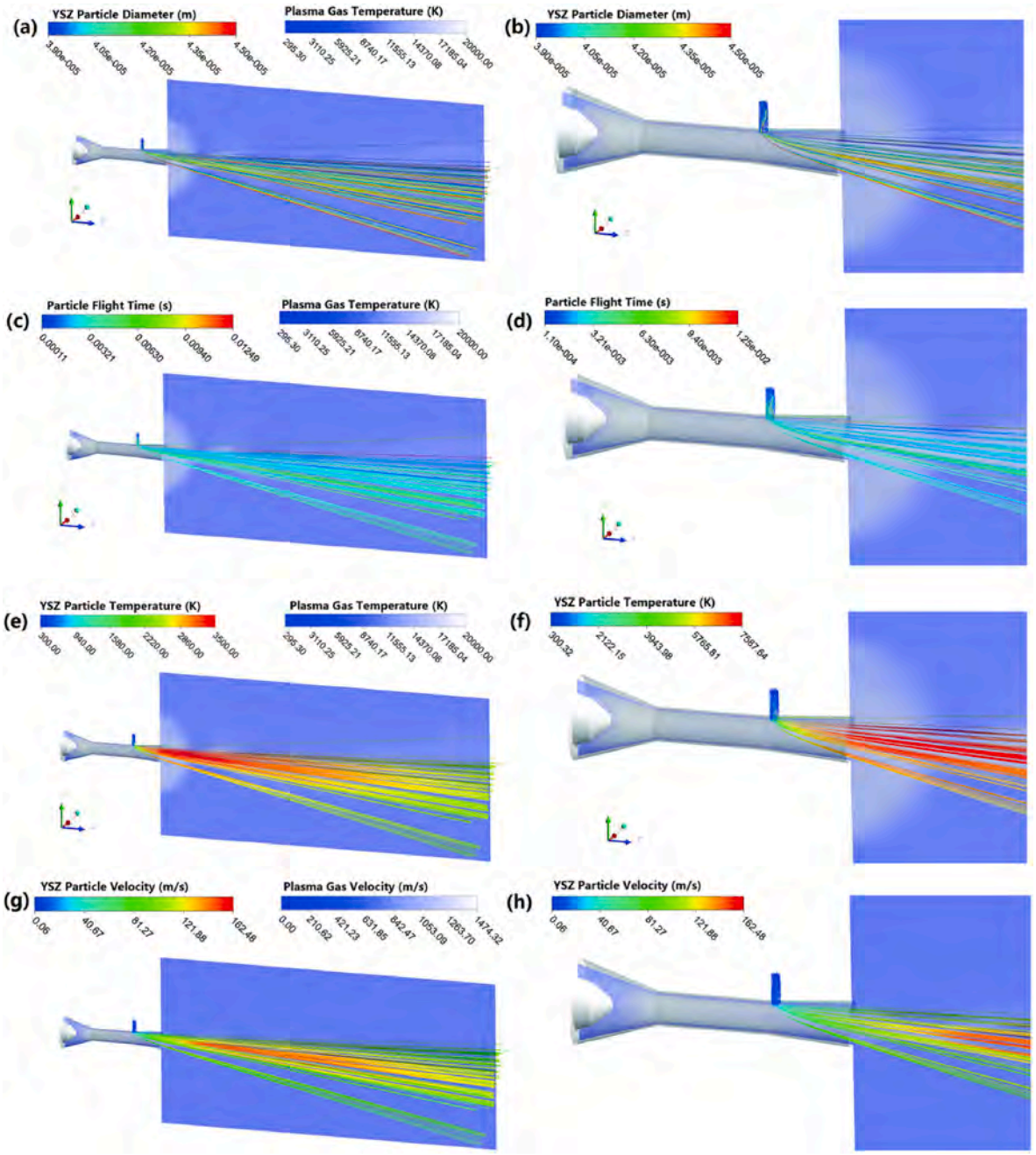

Fig. 14. Numerical simulation of tracked particle flow trajectory under steady model: Plasma jet temperature and YSZ particle (a) diameter distributions, (c) flight time, (e) temperature distribution, and (g) velocity distribution and (b, d, f, h) their corresponding magnified views.

properties, and particle heating histories are analyzed. In Section 5, we present recent progress in PS-PVD technology. Finally, Sections 6 and 7 present the summary and critical challenges of this review, respectively.

2. Modeling of an atmospheric nontransferred arc plasma spraying system

The following sections show recent progress in the multiphase flow effects on the coating microstructure. Deposition technologies include APS, AMPS, ALPS, LPPS, and PS-PVD. The results were obtained from numerical simulations and experimental measurements.

2.1. Processing

In this section, a typical atmospheric plasma spray system (GP-80) is described, which has been used in the Thermal Spray lab of Xi'an Jiaotong University for over two decades. An overview of the plasma spray system and plasma torch are shown in Fig. 10-a and 10-b, respectively. The powders are injected internally using Ar or Ar/H_2 carrier gas. The plasma torch power ranges from 35 to 55 kW. As shown in Fig. 10-c to 10-f, the length of the plasma jet in an atmospheric environment ranges from 30 to 80 mm. Therefore, the spraying distance commonly employed in experiments ranges from 80 to 120 mm for metallic or ceramic powders.

As discussed in Section 1.1, atmospheric plasma jets in a conventional APS system are quite short. Table 3 summarizes the density, kinetic viscosity, thermal conductivity, and electrical conductivity settings commonly used for plasma spraying. The densities of the cold gas and high-temperature plasma gas differ by one to two orders of magnitude. Therefore, the cold carrier gas considerably affected the thermal plasma

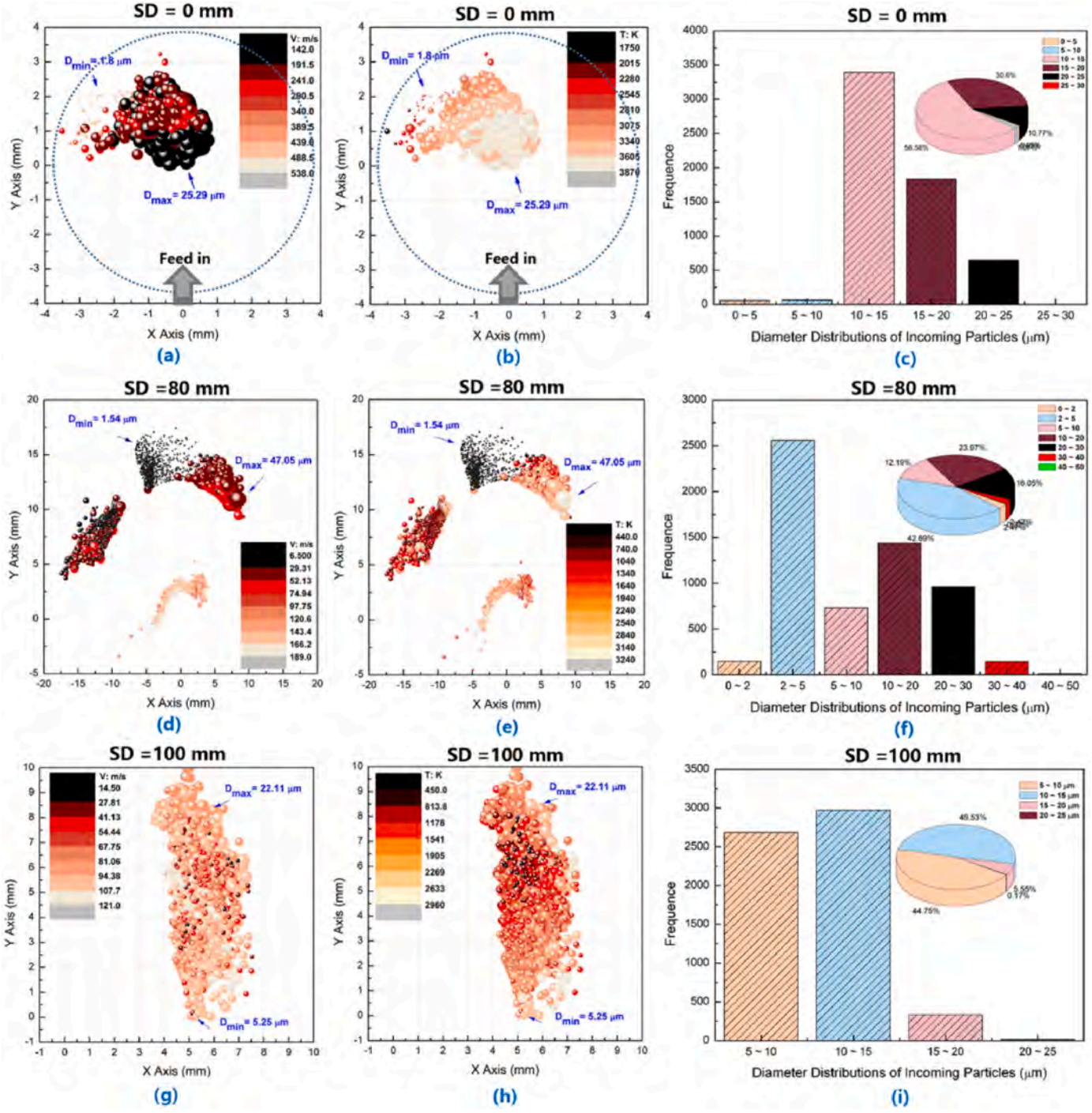

Fig. 15. Numerical simulation of the breakup and atomization of in-flight droplets at different spraying distances (SD): Particle velocity and temperature and the tracked particle diameter distributions at the cross-section of the plasma torch at SD = (a, b) 0, (d, e) 80, and (g, h) 100 mm. Statistical distribution of the particle diameters at the cross-section of the plasma torch at SD = (c) 0, (f) 80, and (i) 100 mm.

gas, particularly during the injection of the internal carrier gas. Li et al. (2001) [95] and Xu et al. (2003) [96] studied their interactions using numerical simulations. The plasma jet (V_{max} = 500 m/s) and particle trajectories deflected from their original axes after the transverse injection of the carrier gas ((V = 10–20 m/s). The radial derivation of the particles is approximately 10–18 mm under these conditions [97].

Considering the one-way injection of the carrier gas in the GP-80 APS system, the chosen calculation domain was a three-dimensional region that included the region of the plasma torch and plasma jet. The input current and Ar gas flow rate of the modeling plasma torch were 550 A and 45 SLPM argon, respectively. The plasma jet is considered to be a fluid, and its transport properties have been reported as functions of temperature. Detailed boundary conditions can be found in previous studies [13,115].

Fig. 11 shows the simulation results for APS performed under carrier gas flow rates of 3 and 10 SLPM. The cold carrier gas (300 K) substantially affected the plasma flow at the bottom of the feeding tube, considering the temperature distributions in Fig. 11-a, 11-b, 11-g, and 11-h. At a high carrier gas flow rate (10 SLPM), a distinct area with low-temperature gas was observed at the bottom of the feeding tube, and the

Fig. 16. (a) Power supply unit of the AMPS system; (b) plasma torch and (c) its internal structure [111]; (d, e) experimental plasma jets produced in an atmospheric environment; (f, g) plasma jet with YSZ particles at different input current.

temperature of the plasma flow increased rapidly at the torch nozzle area. However, the corresponding velocity distributions at the horizontal cross-sections were not apparently disturbed (Fig. 11-d, Fig. 11-e, Fig. 11-j, and Fig. 11-k).

The contour distributions of the plasma gas temperature at the cross-section of the torch nozzle are shown in Fig. 11-c and 11-i. It is evident that there is a relatively low-temperature area at the bottom of the feeding tube at a high carrier gas flow rate (10 SLPM). A similar observation can be drawn from the velocity distributions in Fig. 11-f and 11-l. The centerline distributions of the average plasma gas velocity and temperature at the cross-section of the torch nozzle are shown in Fig. 12-a and 12-d, respectively. The plasma gas velocity increased slightly from 400 to 450 m/s at a carrier gas flow rate of 10 SLPM and main gas flow rate of 45 SLPM argon. Finally, the temperature at the profile evidently decreased from the cross-section to the areas near the boundary wall connected to the feeding tube.

The fluid characteristics, including the surrounding air entrainment during the APS were investigated (Fig. 13). As discussed in Section 1.2, entrainment of the surrounding air can significantly reduce the length of the plasma jet in an atmospheric environment and alter the temperature and velocity distributions. The combined diffusion coefficient method was used to model the diffusion of the gas mixtures [103]. The diffusion mass flux was calculated using the following formula:

$$\overrightarrow{J_A} = -\left(\frac{n^2}{p}\right)\overline{m}_A\overline{m}_B\overline{D}^{x}_{\overline{D}_{AB}}\nabla X_A - \overline{DD}^{T}_{\overline{D}_{AB}}\nabla \ln T \tag{1}$$

where gas A is argon, gas B is air, and m_A and m_B are the average particle masses of Ar and air, respectively [104]. X_A is the mole fraction of argon in the argon–air mixture, and ∇X_A is the argon mole concentration gradient [105].

Considering the entrainment of air, the modeling of the plasma jet length and flow characteristics can approximate real conditions (Fig. 13-e). The expansion of the plasma jet was first apparent near the torch nozzle (Fig. 13-a and Fig. 13-c). The plasma temperature along the-axis decreased abruptly. The high-velocity area of the plasma jet was less than 50 mm. Fig. 13-d and 13-f show the air density and air volume fraction (%) distributions at the horizontal cross-section, respectively. An increasing amount of surrounding air was gradually mixed into the plasma jet owing to the intense entrainment and diffusion along the jet axis. This corresponds to the proposal by Pfender (1994) [49].

2.2. Multiphase flow characteristics during spraying

In this section, the flow characteristics of YSZ particles in the GP-80 APS system are discussed. The original YSZ powder with a particle size range of 39–45 μm was introduced using Ar as a carrier gas supplied at a flow rate of 3 SLPM. The aerodynamic drag force, pressure gradient force, thermophoretic force, and gravitational force were considered to dominate particle motion.

The heat transfer from the plasma gas to the particles was estimated according to the following equation [167]:

at $T < T_m$

$$\pi r_p^2 h_p(T - Tp) = \frac{1}{6}\rho_p \pi r_p^3 C_p \frac{dT_p}{dt} + \pi r_p^2 \sigma_s \varepsilon_{ps}\left(\mathrm{T}_p^4 - \mathrm{T}_a^4\right) \tag{2}$$

at $T = T_m$

$$\pi r_p^2 h_p(T - Tp) = \frac{1}{6}\rho_p \pi r_p^3 H_m \frac{dx_p}{dt} + \pi r_p^2 \sigma_s \varepsilon_{pl}\left(\mathrm{T}_p^4 - \mathrm{T}_a^4\right) \tag{3}$$

at $T_m < T < T_b$

$$\pi r_p^2 h_p(T - Tp) = \frac{1}{6}\rho_p \pi r_p^3 C_p \frac{dT_p}{dt} + \pi r_p^2 \sigma_s \varepsilon_{pl}\left(\mathrm{T}_p^4 - \mathrm{T}_a^4\right) \tag{4}$$

at $T = T_b$

$$\pi r_p^2 h_p(T - Tp) = -\frac{1}{2}\rho_p \pi r_p^2 H_b \frac{dd_p}{dt} + \pi r_p^2 \sigma_s \varepsilon_{pl}\left(\mathrm{T}_p^4 - \mathrm{T}_a^4\right) \tag{5}$$

Here, ε_{ps} and ε_{pl} represent the emissivities of the solid and liquid phases of the particles, respectively. Furthermore, x_p denotes the molten mass fraction of particles. H_m and H_b are the latent heats of melting and evaporation of YSZ particles, respectively. T_m and T_b are the melting and evaporation points of YSZ particles, respectively. T_a denotes the ambient temperature and σ_s is the Stefan–Boltzmann constant.

The heat-transfer coefficient can be calculated from the Nusselt number, which can be solved using the following formula proposed by Vardelle et al. [106].

$$\mathrm{Nu} = 2.0 + 0.515\sqrt{\mathrm{Re}_p} \tag{6}$$

Fig. 14 shows the modeling results for the plasma jet and particles. YSZ was injected through the feeding tubes. The particles then flowed outside this area (Fig. 14-a and 14-b). The flow trajectory of the small particles was tracked close to the jet axis, and that of the larger particles

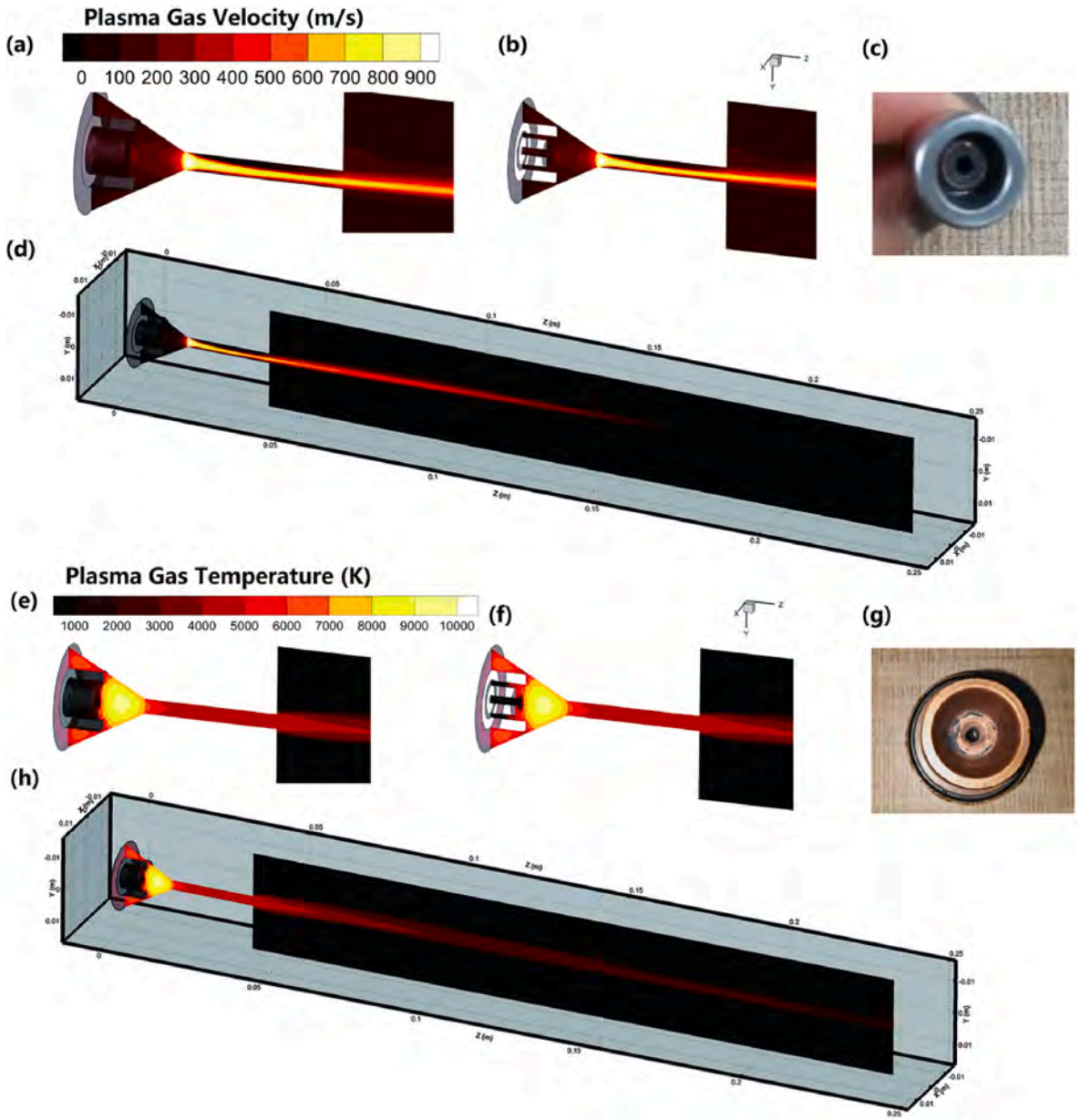

Fig. 17. Numerical simulation of the novel microplasma torch and plasma jet: (a, b) plasma gas velocity distribution inside the plasma torch; (c) cathode used in the experiment; (d) velocity distribution; (e, f) plasma gas temperature distribution inside the plasma torch; (g) anode used in the experiment; (h) temperature distribution.

further deviated from the plasma jet owing to the influence of gravity. In addition, the flight time of the differently sized particles to a maximum distance of 150 mm was short (0.0002–0.009 s). The calculated particle temperature distribution and corresponding magnified plots are shown in Fig. 14-e and 14-f, respectively. The temperatures of the particles and gas inside the feeding tube were lower than those near or at the torch nozzle. The area where the maximum particle temperature was recorded was located outside the nozzle exit. A similar observation can be drawn from Fig. 14-g; the particles gradually accelerated downstream of the plasma jet.

Fig. 14 shows the steady model fluid characteristics during APS, which is beneficial for understanding the experimental multiphase flow and optimizing the deposition parameters. Fig. 15 shows the breakup and atomization models of in-flight droplets during the GP-80 APS processing. The Kelvin–Helmholtz/Rayleigh–Taylor (KH–RT) breakup model was used to track the droplets and particles and to emulate the primary breakup at the initial step and the secondary breakup of in-flight droplets [60,107]. The KH-RT model was found to provide satisfactory results for the predicted spray shape and penetration [108,109].

At the cross-section of the torch nozzle, the in-flight droplets were under high plasma gas velocity and temperature areas (Fig. 15-a and Fig. 15-b). From the magnified view of the tracked trajectory in Fig. 14, the location of the droplets at the cross section deviated from the center after their injection from the feeding tube. The powder had an initial size of 39–45 μm. Fig. 15-c shows the particle diameter distribution. Approximately 56.58% of droplets are in the size range from 10 to 15 μm, 30.6% are in the range from 15 to 20 μm, and 10.77% droplets are in the range from 20 to 25 μm.

Fig. 15-a and Fig. 15-b show the tracked particle velocity and temperature at the cross-section of the spraying distance of 80 mm, respectively. Owing to the strong gravitational and aerodynamic forces, the droplets and solid particles were distributed over a large area. The maximum deviation distance in the Y-direction was 18 mm, and the droplets close to the plasma jet axis exhibited high temperature and

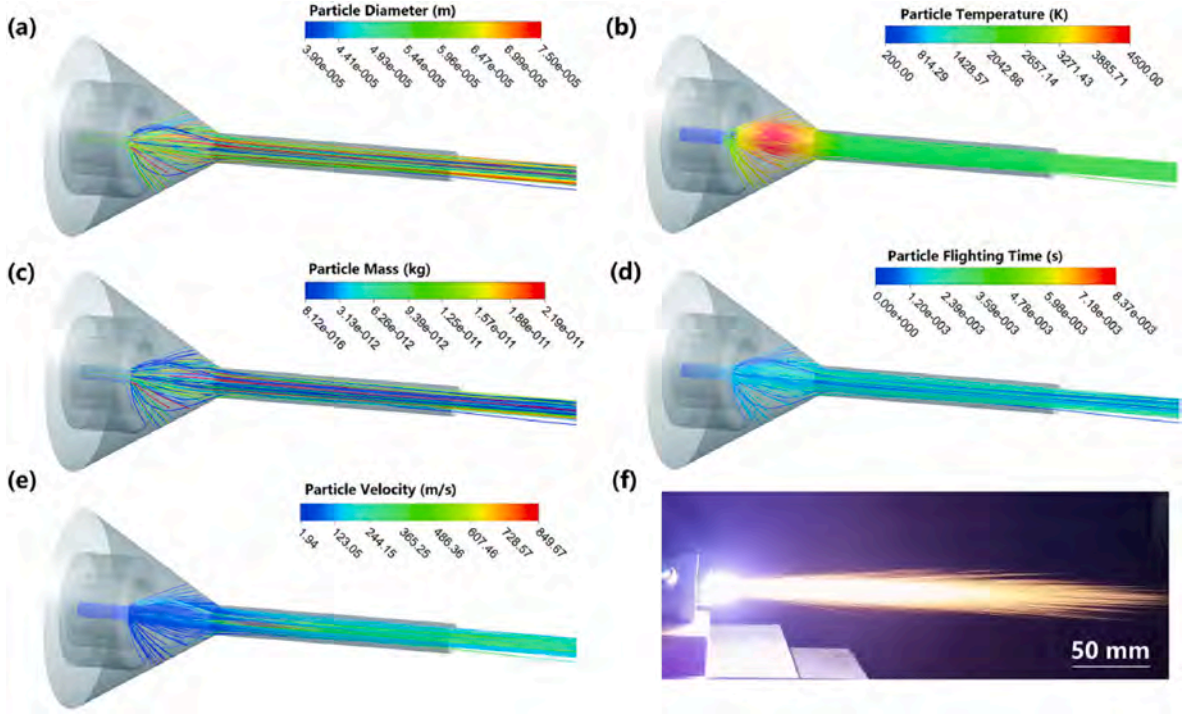

Fig. 18. Modeling of the YSZ particle flows in the AMPS; (a) particle diameter; (b) temperature; (c) mass; (d) flight time; and (e) velocity. (f) Experimental image of the YSZ particle spraying.

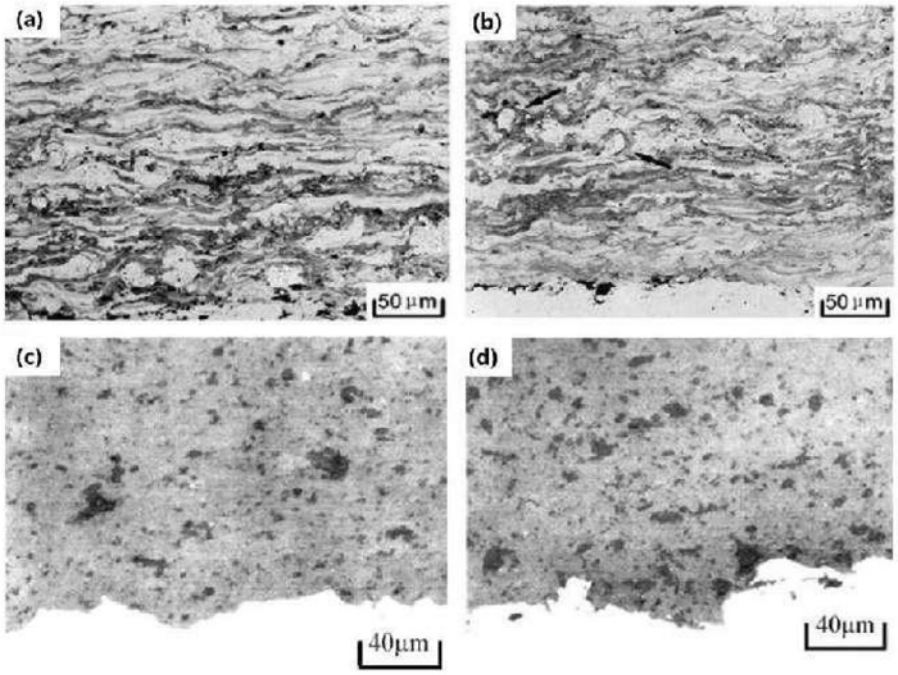

Fig. 19. Microstructures of the coatings produced through AMPS: Cu coating deposited at a torch power of (a) 3.5 and (b) 2.8 kW [110]; Al_2O_3 coating deposited at a torch power of (c) 2.2 and (d) 3.9 kW [111].

velocity. However, the particle diameter distributions obtained through statistical analyses (Fig. 15-f) had a larger variation than the previous results presented in Fig. 15-c. 42.69% of particles are in the range from 2 to 5 μm, 23.97% are in the range from 10 to 20 μm, 16.05% are in the range from 20 to 30 μm, and 12.19% are in the range from 5 to 10 μm. The average size of the deposition unit decreased significantly after a flight distance of 80 mm.

At a spraying distance of 100 mm, which is also a commonly used distance for depositing YSZ coatings, the tracked particles were located in a narrow area at the cross-section. The minimum and maximum size of the particles were 5.25 and 22.11 μm, respectively (Fig. 15-g and 15-h). The average size of the depositing units decreased continually. Approximately 44.75, 49.53, and 5.55% of the particles had sizes ranging from 5 to 10, 10–15, and 15–20 μm, respectively.

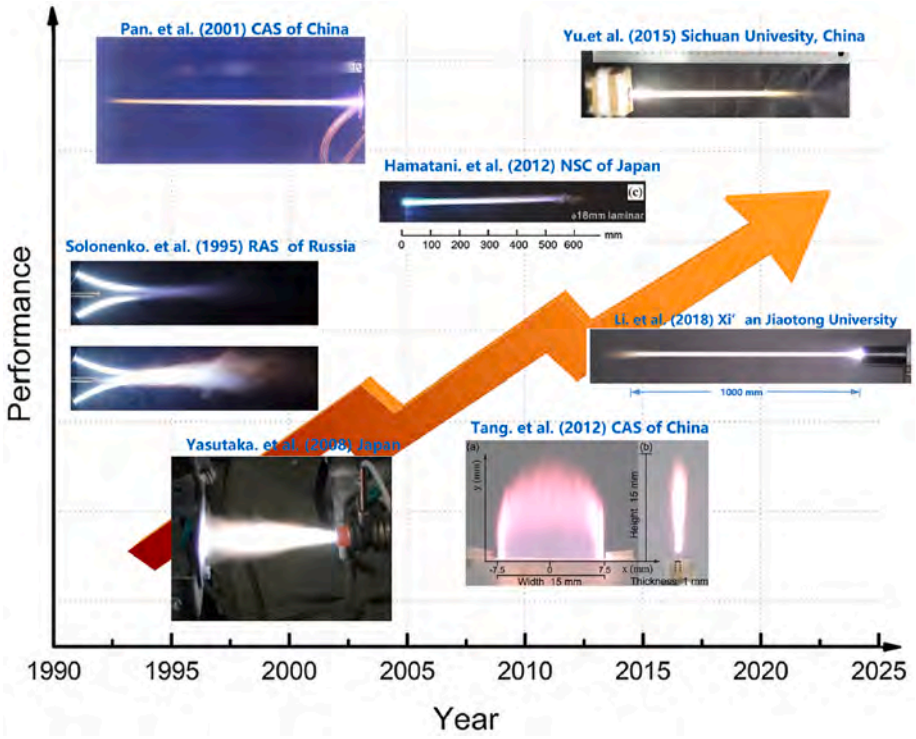

Fig. 20. History and developments of quasi-laminar plasma jets used in materials processing [123,125–127,130,131,134] (Reproduced with permission © Springer Nature, AIP Publishing, IOP Publishing Ltd, & Elsevier B·V.).

3. Novel atmospheric micro-plasma spraying system (AMPS)

3.1. AMPS processing

In this section, AMPS technology, which uses the internal injection of powders from a hollow cathode, is discussed. The method was first proposed by Li et al. (2003) [110,111]. Fig. 16 shows the APS system. The input power ranges from 2.1 to 9.5 kW. In contrast, the input current and arc voltage ranges from 40 to 120 A and 54–88.9 V, respectively. The main input gases, Ar and N_2, are supplied at a total flow rate of 33–65 SLPM. The experimental plasma jet is shown in Fig. 16-d and 16-e. At 80 A, the length of the plasma jet in an atmospheric environment was approximately 90 mm. Figs. 16-f and 16-g show high-speed camera images using a red narrowband filter of the YSZ particles at a carrier gas flow rate of 10 SLPM from the cathode tip. Novel AMPS processing allows longer particle heating distances than the conventional APS method discussed in Section 2.

To better understand the AMPS technology, computational fluid dynamic simulations were performed (Fig. 17), wherein the plasma torch and jet areas are usually identified. The calculation domain was originally derived from the experimental parameters. For the initial simulations, Ar and N_2 were used as the main and carrier gases, supplied at 40 and 10 SLPM, respectively. The input current was 80 A. Fig. 17-a to 17-c show the velocity distributions from the plasma torch to the plasma jet. The predicted maximum velocity inside the plasma torch was approximately 950 $m\ s^{-1}$. The high-velocity area of the plasma gas was located at the throat of the torch nozzle, where the main and carrier gases crossed each other. Subsequently, the plasma gas flowed through the cylindrical nozzle before being ejected into the surrounding air. In contrast, the high-temperature area of the plasma gas is located at the center of the anode. The predicted maximum temperature inside the plasma torch was approximately 9850 K. The water-cooling nozzle decreased the temperature of the plasma gas before it was ejected from the torch nozzle. Fig. 17-g shows the eroded anode after the experiment.

3.2. Multiphase flows and heat transfer in AMPS

Fig. 18 shows the simulations of the YSZ particle heating and motion profiles at a carrier gas flow rate of 10 SLPM and feed rate of 5 $g{\cdot}min^{-1}$. The control equations for the particle heating and motion are described in Section 2.2. Fig. 18-a shows the steady model flow trajectories of the injected particles. Multisized particles were injected from the center tube and then expanded at the center of the anode. Subsequently, the particle flow converged to the nozzle tube, and YSZ was ejected outside. Fig. 18-f shows experimental images of under the same conditions.

The particle temperature distribution is shown in Fig. 18-b. The particle temperature in the internal tube of the cathode was approximately 300 K. When multisized particles were injected into the anode area, the particle temperature rapidly increased. Subsequently, it decreased in the nozzle–tube area.

The particle velocity gradually increased from the internal tube of the cathode to the nozzle tube. The maximum particle velocity area was located at the center of the nozzle tube (Fig. 18-e). The particle flight time was within 1.2 ms.

3.3. Microstructure of coatings by AMPS

Dense ceramic coatings with fully bonded splats are difficult to produce using conventional APS at room temperature [112]. Increasing the plasma power increases both the temperature and velocity of the particles, forming a dense coating with good cohesion between flattened particles and good adhesion to the substrate [111]. The total output power and gas flow rate used in AMPS processing are significantly lower than those employed in other commercial APS systems. Therefore, AMPS was designed to achieve high droplet temperatures at a low output power.

Fig. 19 shows the microstructures of Cu and Al_2O_3 coatings produced through AMPS at a torch power of 2.8–3.9 kW. The polished cross-section of the Cu coating exhibited a dense lamellar microstructure. The oxygen content was measured using an oxygen analyzer. The

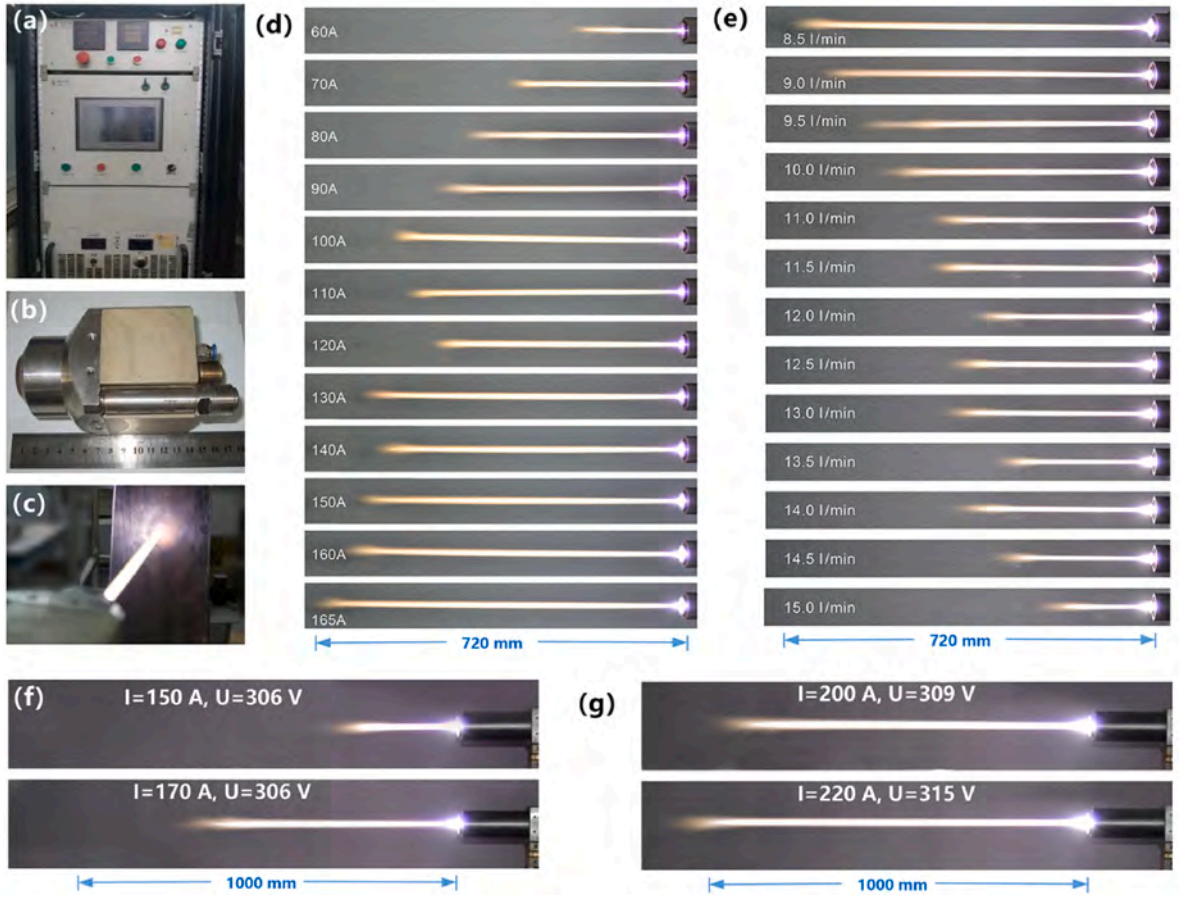

Fig. 21. Novel atmospheric laminar plasma spray technology: (a) power supply unit; (b) plasma torch [115]; (c) long laminar plasma jet impinged on a substrate [116]; (d) plasma jet length variation under different input currents (9.8 SLPM N_2+ 4.2 SLPM Ar), (e) total gas flow rate (I = 100 A) [34], and (f), (g) using 15 SLPM N_2 and 8 SLPM Ar [34] (Reproduced with permission ©Springer Nature, AIP Publishing, IOP Publishing Ltd & Elsevier B·V.).

concentrations ranged from 2.03% to 2.14%. The experimental Cu particle velocity at a spraying distance of 30 mm was approximately 110 $m\ s^{-1}$ according to two-color pyrometry results [110]. Moreover, the Al_2O_3 coating exhibited dense microstructures despite the low plasma torch power applied during spraying. Therefore, coatings with dense microstructures and ample properties can be deposited through AMPS, even at a low output plasma torch power (see Fig. 20).

4. Novel atmospheric long laminar plasma spraying system (ALPS)

4.1. ALPS processing

Over the past three decades, many commercial coating companies have been built globally with the development of the APS technology. In 2020, the global thermal spray coating market was valued at USD 7.6–10.4 billion [113,114]. However, the relationship between the torch input power and the particle temperature still needs to be studied. In general, the particle velocity and temperature increase with increasing torch power. However, the particle flight distance, that is, the spraying distance, and particle dwell time in the plasma plume do not increase simultaneously. As such, the particle temperature does not continuously increase with increasing torch power. Moreover, the deposition efficiency decreases beyond a critical value for particle velocity.

For the purpose of significantly increasing particle surface temperature during atmospheric plasma spray, a novel long laminar plasma torch was applied. The utilization of quasi-laminar and long laminar plasma jets has been proposed and developed over the past few years (Fig. 21). The output power of the laminar plasma equipment varied from 2.35 to 50 kW. The diameter of the anode nozzle was 4–18 mm. Finally, the plasma jet lengths were varied from 100 to 1000 mm using N_2 or Ar gas (Table 4) (see Table 5).

Laminar plasma jets have been successfully used in three-dimensional additive manufacturing [117], plasma synthesis of fine powders [118,123], welding [130], and remelting or cladding of metallic surfaces [119,120]. This method presents highly stable operation, exhibits great flexibility with plasma gases, and improves existing material processing methodologies, which paves the way for the development of new advanced technologies. However, only a few studies have investigated atmospheric long laminar plasma spray technology before 2015. A suitable particle injection method for this spray technology remains to be identified. Variations in the particle velocity and temperature of the laminar plasma jet need to be investigated. Moreover, the properties of laminar plasma-sprayed metallic and ceramic coatings should be studied systematically.

Fig. 21 shows a novel ALPS system composed of a plasma torch, power supply, powder feed unit, water cooling unit, and wires and cables. At a constant flow rate (8.5 SLPM) of a N_2–Ar mixture (70:30 vol ratio), the length of the plasma jet increased as the input current increased from 60 to 165 A. Under such conditions, the maximum plasma jet length was 720 mm (Fig. 21-d). Conversely, the length of the plasma jet decreased as the total gas flow rate increased from 8.5 to 15 SLPM (Fig. 21-e) at a constant input current of 100 A. From Fig. 21-g, the maximum length of the plasma jet can be as high as 1000 mm in an atmospheric environment (I = 220 A, 15 SLPM N_2 + 8 SLPM Ar). Under each condition, the fluid characteristics throughout the plasma jet were highly stable. Turbulence is observed only in the wake or end region of the jet [34]. Therefore, this method provides a wide range of operating

Table 4
Research history of laminar or quasi-laminar plasma torches [121,121].

Year	Departments	Authors	Working Power/Gas	Nozzle Diameter /Jet Length	Reference
1995	Institute of Theoretical and Applied Mechanics, Russia Academy of Sciences	Mikhail F. Zhukov, Solonenko O.P. et al.	50 kW Ar+3%H_2	D = 8 mm, L = 500 mm	[122, 123]
1997	Institute of Aeronautical Engineering, Aviation Industry of China	H. C. Wu; X. D. Yang	Ar, 13–14 SLPM 17.4 kW	L = 100–500 mm	[124]
2000	Yamaguchi University, Japan	Osaki, K. et al.	Ar, 5–8 SLPM 2.35–3.43 kW	D = 6 mm, L = 400–450 mm	[125]
2001	Institute of Mechanics, Chinese Academy of Science, China	W. X. Pan, C. K. Wu. et al.	Ar/Ar + N_2, 12–30 SLPM 15–30 kW	D = 4–10 mm, L = 250–600 mm	[126]
2008	Ashikaga Institute of Technology, Japan	Yasutaka Ando. et al.	Ar, 3.5–10 SLPM, 3.12 kW	D = 6 mm L = 100 mm	[127]
2008	Georgian Technical University, Georgia	M. Khutsishvili	Ar 7.5–9 kW	D = 7–8 mm L = 140 mm	[128]
2012	Nippon Steel Corporation, Japan	Hideki Hamatanis. et al.	Ar+2%N_2 18–40 kW	D = 18 mm, L = 600 mm	[129, 130]
2012	Xi'an Institute of Optics and Precision Mechanics, Chinese Academy of Science	Tang, J. et al.	N_2 500W (DC Glow Discharge)	D = 15 × 1 mm (rectangle) L = 15 mm	[131]
2014	University of Limoges, France	J. Krowka. et al.	N_2, 1.1 kW 0.0336–0.0992 SLPM	D = 2.5–4 mm L = 10–14 mm	[132]
2015	Sichuan University, China	De-ping Yu. et al.	N_2/Ar,1.3–4.1SLPM 0.9–10 kW	D = 3 mm L = 300–400 mm	[133, 134]
2015	University of Science and Technology of China, China	Jiang-ling Wang, Z. X. Dong. et al.	N_2/Ar, 5–8.5 SLPM 1.2–5 kW	D = 3–5 mm L = 180–500 mm	[135]
2018	Xi'an Jiaotong University, China	C. X. Li. et al.	N_2/Ar, 8–25 SLPM 8–100 kW	D = 5–8 mm L = 100–1000 mm	[121]
2020	Southeast University, China	Ting Dai. et al.	Ar, I = 60 A, wire feed rate of 20 mm/s	\	[136]
2020	Sichuan University of Science and Engineering, China	Xiuquan Cao. et al.	N2, 9–18 SLPM, I = 60–120 A	L = 520–550 mm	[137, 138]

Table 5
Operating parameters of the atmospheric long laminar plasma jet in this work.

Output Power (kW)	Plasma Gas	Total Flow Rate (SLPM)	Input Current (A)	Arc Voltage (V)	**Jet Length (mm)**	Powder Feed Rate (g/min)
8–30	Ar, N_2/Ar, or N_2	8 15	60–165	135–158	100–720	1–25
30–100	Ar, N_2/Ar, or N_2	15–25	60–220	130–315	150–1000	1–25

conditions for parameters such as the spraying distance, substrate temperature, and powder injection, which are critical for plasma spraying. This method can also be applied to the repair of small parts and pipe coatings.

4.2. Multiphase flow and heat transfer in ALPS processing

In this section, the particle heating and motion profiles during ALPS are presented. A commercial DPV-2000 particle diagnosis system was used to monitor the particle velocity and surface temperature of Al_2O_3, $La_{0.6}Sr_{0.4}Co_{0.2}Fe_{0.8}O_{3-\delta}$, Mo, and YSZ powders at different spraying distances (Fig. 22). Details of the spraying parameters are listed in Table 6.

Powder injection was performed radially near the torch nozzle. Initially, the particle velocities of the different powders were low. Subsequently, they gradually increased along the laminar plasma jet (Fig. 22-a). Considering the densities of the powders, the maximum particle velocity of the Al_2O_3 particles was higher than that of the Mo, Ni-60, and YSZ powders. During the ALPS processing, the particle surface temperature along the axis direction of the plasma jet was consistently high (Fig. 22-b). In particular, the surface temperatures of the YSZ and Al_2O_3 powders are close to their boiling points. Although the output power of other conventional plasma spray methods is higher than that of the ALPS method, the particle surface temperatures during these traditional spraying routes are not apparently higher than those obtained during ALPS processing.

A three-dimensional simulation of ALPS processing is shown in Fig. 23 (I = 160 A, 9.8 SLPM N_2+4.2 Ar), where a plane substrate was set at a spraying distance of 250 mm. YSZ powder (Metco 6700 8YSZ, d = 1–30 μm, d_{50} = 10 μm) was injected in the radial direction of the plasma jet near the torch nozzle without a carrier gas. Fig. 23-b shows the particle diameter distributions along the tracked trajectories. Small particles (diameter <5.8 μm) consistently flowed along the plasma jet axis. In contrast, larger particles gradually flowed down and deviated from the center of the plasma jet, particularly at a spraying distance of 250 mm. Fig. 23-c shows the YSZ particle velocity and corresponding plasma gas velocity distributions. Fig. 23-e shows the YSZ particle temperature and corresponding plasma gas temperature distributions. The results of the theoretical simulations correspond well with the experimental measurements, which show that the particle velocity near the torch nozzle was low during the initial stage and gradually increased with spraying distance. A large region of high particle temperature was observed during plasma spraying. Moreover, the in-flight particles far from the center of the plasma jet exhibited low velocities and temperatures (Fig. 23-c and 23-e).

Fig. 23-d and 23-f show the YSZ particle flight time and mass distribution, respectively. The mean flight time of the YSZ particles ranged from 0.47 to 2.36 ms. The maximum flight time of the particles far from the center of plasma jet was 2.84 ms. The particle mass distribution corresponded well to the particle diameter distribution; low and high mass concentrations were observed near and away the plasma jet axis, respectively.

Fig. 23-g and 23-h present the experimental observations when the YSZ particles were injected at the initial stage near the torch nozzle at feed rates of 5 and 2 g/min, respectively. The penetration distance of the injected particles along the radial direction varied for the two feed rates. If this method were used in conventional APS, the quality of the coating

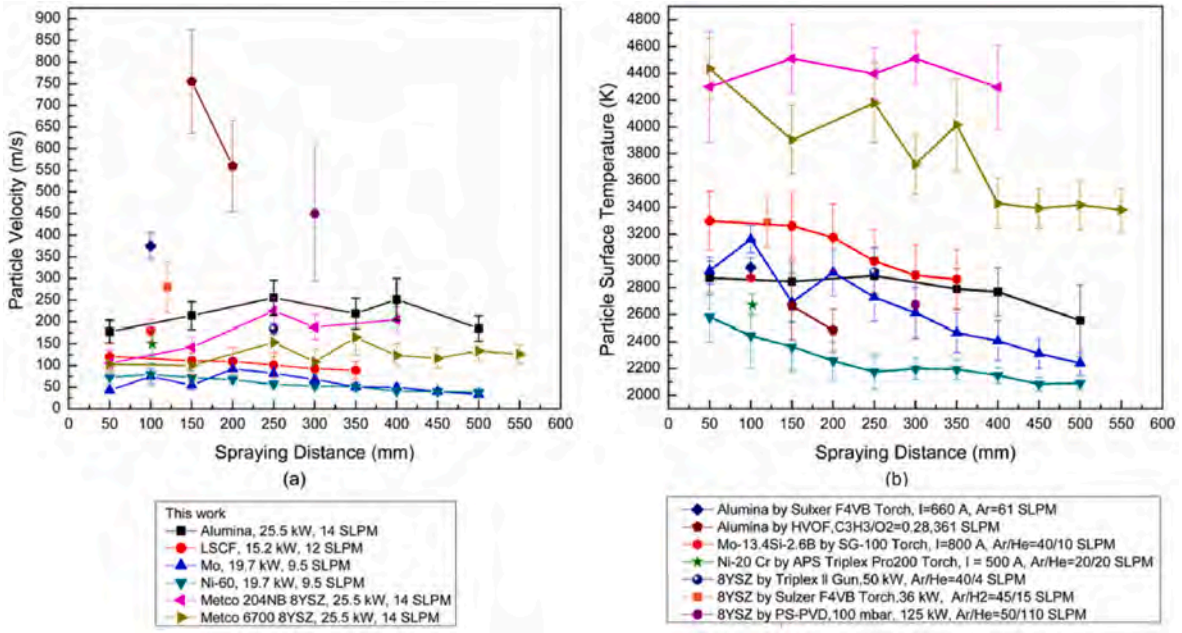

Fig. 22. (a) Particle velocity and (b) surface temperature during atmospheric laminar plasma spray using DPV-2000 in the experiment [19,90] (Reproduced with permission ©Springer Nature & Elsevier B·V).

Table 6
Particle materials, diameters, and spraying parameters in ALPS processing [90,139,140].

Name or Business Name	Materials	Density (kg/m^3)	Particle Size	Melting Point (K)	Depositing Parameters
Metco 6062 Al_2O_3	Al_2O_3	3965–3990	−45 ~ +22 μm	2327 K	25.5 kW, 14 SLPM
LSCF	$La_{0.6}Sr_{0.4}Co_{0.2}Fe_{0.8}O_{3-\delta}$	6210		2013 K	15.2 kW, 12 SLPM
Mo	Mo	10,220	−100 to +40 μm	2890 K	19.8 kW, 9.5 SLPM
Ni-60	Ni, 5%Fe, 3–4.5% B, 3.5–5.5% Si, 14–18% Cr, 0.6–1% C	7528–7793	−106 to +45 μm	1323–1353 K	19.8 kW, 9.5 SLPM
Metco 204NB YSZ	7–8 mol% Y_2O_3 + ZrO_2	5680–5980	−75 μm to +39 μm	2950 K	25.5 kW, 14 SLPM
Metco 6700 YSZ	7–8 mol% Y_2O_3 + ZrO_2	5680–5980	−30 μm to +1 μm	2950 K	25.5 kW, 14 SLPM

would be considerably affected if it were produced using the conventional APS method under similar deposition parameters to those discussed in Section 2. However, because of the long heating and motion distances achieved through ALPS, the bias value and effect of the initial powder injection were eliminated.

Furthermore, the self-shadowing effect of impinging YSZ particles on the substrate (Inconel 718 alloy, δ = 5 mm) was investigated (Fig. 24). At a spraying distance of 250 mm, a highly focused deposition spot with a high pressure gradient was observed at the center of the substrate (Fig. 24-a), where the maximum temperature of the substrate was 1120 K. The tracked trajectories of impinging particles (d = 1–30 μm) at the velocity boundary layer of the substrate are shown in Fig. 24-d. Apparently, the smaller particles preferred to bend and then flow on the surface of the substrate because the plasma jet streamlines became parallel to the substrate, resulting in very low incident angles of the impinging particles. The fluid mechanism of the self-shadowing effect of the impinging particles was caused by different tangential velocities of particles with different sizes within the velocity boundary layer of the substrate; small particles (diameter ≤2.56 μm) had larger tangential velocities than the larger particles. As such, during the repeated scanning of the plasma spraying, the previously deposited particles blocked the incoming particles from the incident direction (Fig. 24-f). The growth rate of the local areas of deposition along the vertical direction is higher than that along the horizontal axis [20]. Thus, non-line-of-sight coatings can be deposited on blades, vanes, buckets, or combustion components of complex structures.

The D50 of the original YSZ powders used for the ALPS processing was 10 μm [141], which implies that the diameter of 50% of the particles was smaller than 10 μm. It is currently a specifically designed powder to produce EB-PVD type microstructures using PS-PVD coating process [93, 94]. Considering these results, the self-shadowing effect of the impinging particles will be promoted if the size of most particles ranges from 1 to 10 μm. Moreover, the size of the original YSZ particles in the atmospheric suspension and plasma spraying solution ranged from 0.001 to 0.5 μm [142,143]. Therefore, ALPS processing also allows the fabrication of quasi-columnar structures owing to the shadow effect of in-flight particles on the substrate [144].

4.3. Depositing of coatings in ALPS technology

Metallic powders (Mo and Ni-60) and ceramics (YSZ, LZO, and LSCF) were deposited using the ALPS method under different deposition conditions. Despite the different sizes of the original powder used, abundant vapor-deposited microstructures formed on the top surfaces of the coatings (Fig. 25). Thermal barrier coatings based on YSZ, LZO, or LCO of vertical crack microstructures were deposited directly through the ALPS method even without auxiliary heating of the substrate (Fig. 25-e and 25-f). Moreover, the produced coatings were not thick. The crack density was approximately 4–5 cracks·mm^{-1}, which was higher than that of coatings deposited using the conventional APS method [145–147].

The LSCF coatings exhibit cluster-like microstructures on their top surfaces. Large-scale vertical cracks were observed at the cross-section. Furthermore, the polarization resistance of the LSFC coating prepared using the ALPS method was lower than that of the coatings deposited using conventional APS routes [148] (Fig. 25-c, -d). Vertical cracks at

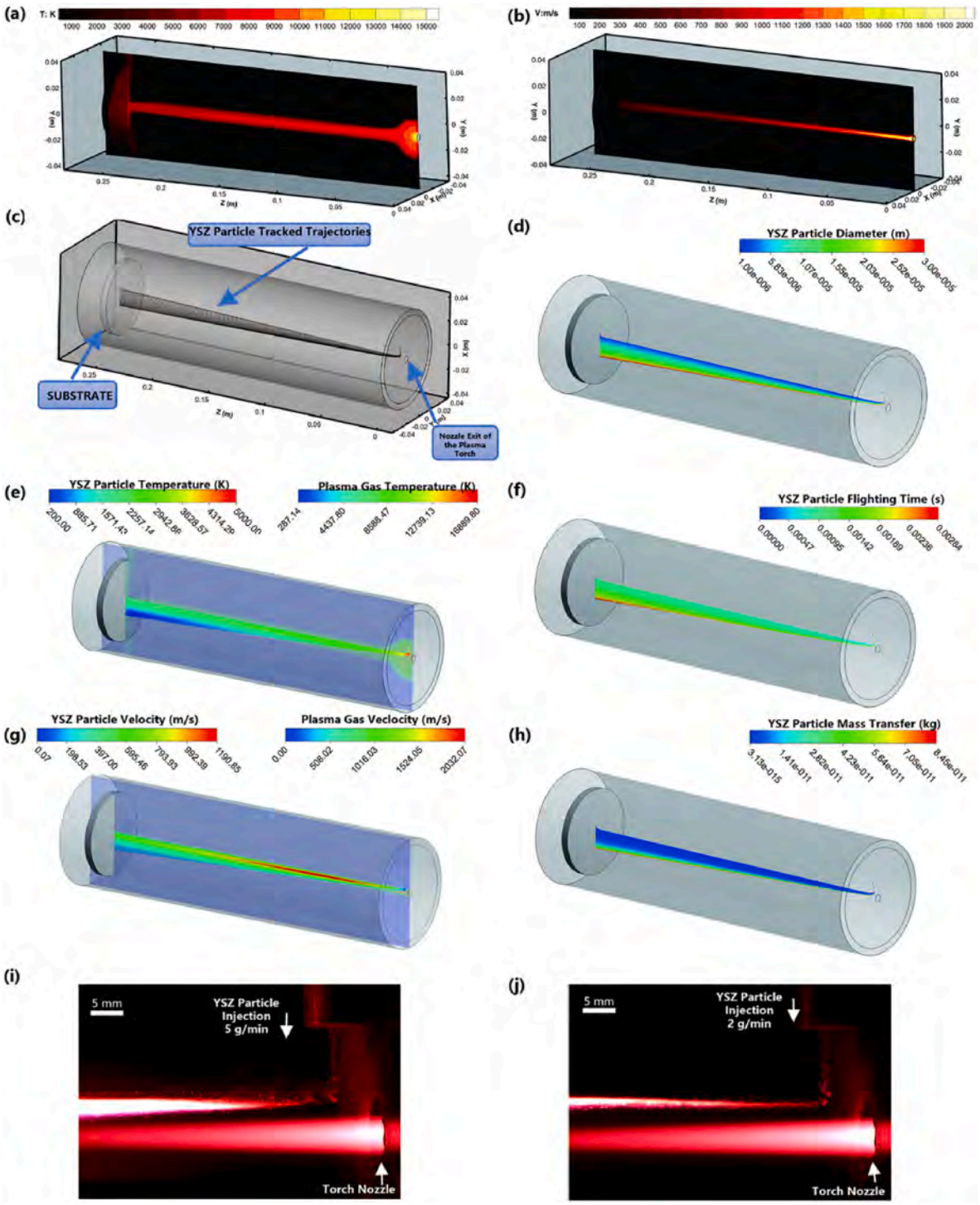

Fig. 23. (a) Atmospheric long laminar plasma gas (a) temperature, (b) velocity distribution [20]; and (c) YSZ particle tracked trajectories at a spraying distance of 250 mm; YSZ particle (d) diameter distribution (Metco 6700 8YSZ, D = 1–30 μm); (e) particle temperature with plasma temperature; (f) flight time; (g) velocity distribution; and (h) mass distribution along the tracked trajectories; experimental YSZ particle injection near the torch nozzle at a feed rate of (i) 5 g·min^{-1} and (j) 2 g·min^{-1}.

the cross-section of the coating can improve the gas diffusion characteristics of the material when used as a cathode in SOFCs. Therefore, this technology represents a promising novel route for the synthesis of functional SOFC coatings.

In contrast, vapor-deposited clusters of needle-like microstructures were observed on the top surface of the Mo-based coatings. The Mo particles were fully melted at spraying distances of 150–400 mm. The hardness of the coating increased with increasing molybdic oxide content during plasma spraying, indicating that the coating quality can be tuned by modifying the deposition parameters during ALPS processing.

Coatings are produced through multiple impinging particles such as droplets, semi-molten droplets, condensed particles from vapor phases, and resolidified particles. For ceramic coatings produced through the conventional APS process, flattened droplets form a typical lamellar structure at the cross-section. Pores, unbonded interfaces, and cracks are

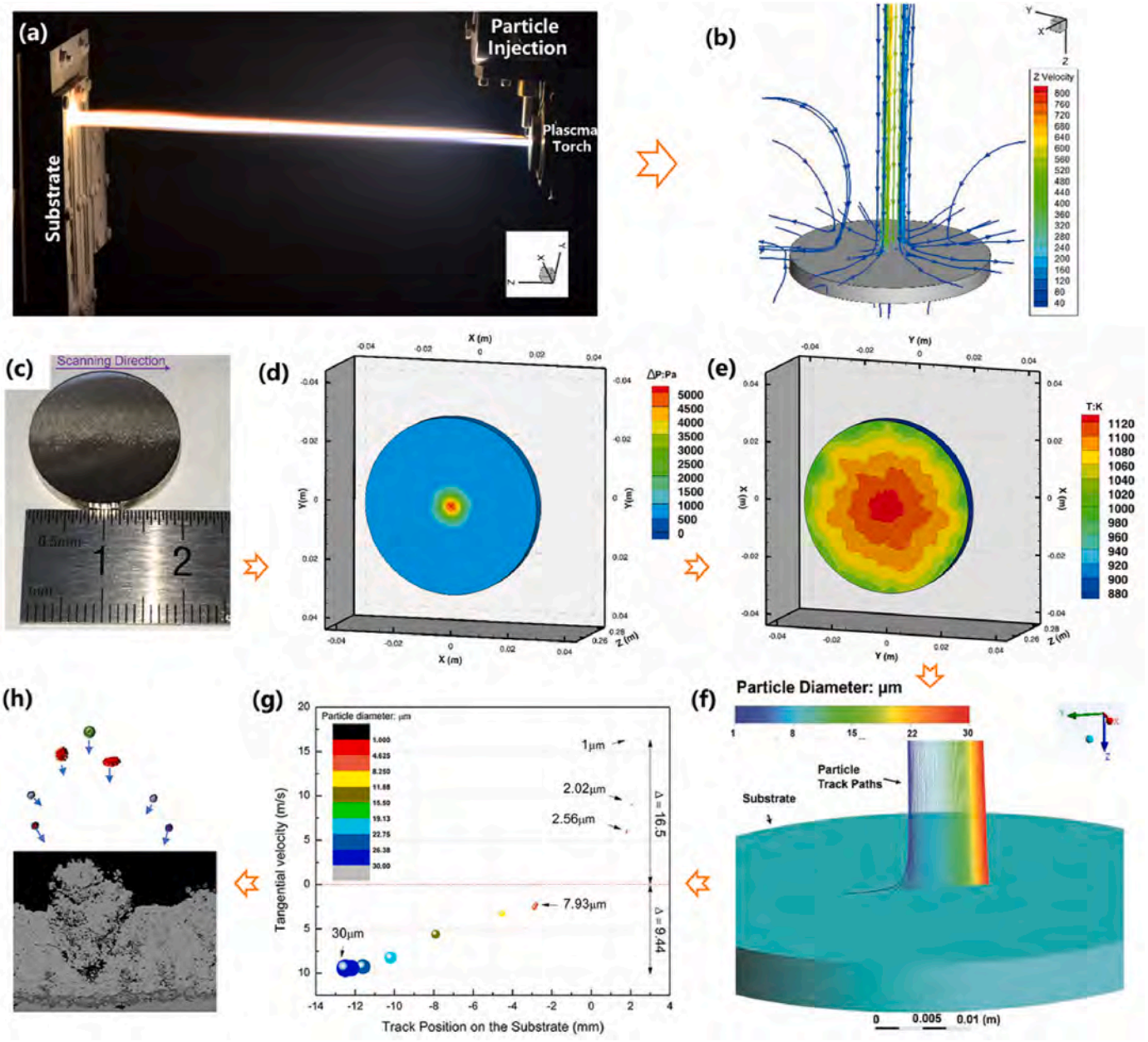

Fig. 24. (a) ALPS processing at a spraying distance of 250 mm; (b) velocity flow along the *z*-axis of the plasma jet at the edge of the substrate; (c) polished substrate after a single plasma spraying scan; (d) pressure gradient; (e) temperature distribution; and (f) track paths of multiple particles on the substrate surface prior to flattening; (g) tangential velocity of the particles as a function of the track position on the surface of the substrate according to (f); (h) shadowing effect of the incident particles on the microstructural formation in ALPS [20] (Reproduced with permission ©Springer Nature, IOP Publishing Ltd & Elsevier B·V.).

also commonly formed [2,6]. The ALPS process provides high particle surface temperature and substrate temperature (e.g., 500–850 °C) to induce the vapor deposition in an atmospheric environment. A mass of stable clusters of all sizes was observed on the substrate, which featured needle-like and needle/cauliflower-like clusters that possibly originated from the vapor stream during plasma spraying [20]. Cauliflower-like clusters were formed through the co-deposition of vapor and droplets and resolidification of particles. Stable clusters are formed on the substrate through adatom capture by surface diffusion and the direct deposition of atoms from the vapor stream during plasma spraying [151]. The surface roughness (Ra) of the as-sprayed YSZ coating with a thickness of 150 μm ranged from 25 to 38 μm. Nevertheless, the formation of a mixture of deposition units, such as solids, droplets, and vapor, is difficult to avoid, particularly under atmospheric plasma-spraying conditions. In addition, surface diffusion of some droplets within the as-sprayed coating can also affect the final microstructure at the cross-sectional interfaces and interspaces. Furthermore, secondary dendrite growth on the deposited splats [20], which occurred uniformly along the edge of a flattened splat, was observed, possibly owing to the high interface/substrate temperature during plasma spraying.

Calcium–magnesium–aluminosilicate (CMAS) corrosion can lower the lifetime of coatings, which is particularly problematic for thermal barrier coatings in aircraft engines, as molten CMAS from sand, dust, and/or volcanic deposits can penetrate the coating, which induces corrosion of the components when the aircraft is subjected to various environments. YSZ coatings produced through ALPS which exhibit high surface roughness are beneficial for the prevention of CMAS corrosion. The multi-island protrusions on the top surface, with a mean Ra of 33.8 μm effectively hindered the spreading and penetration of CMAS into the

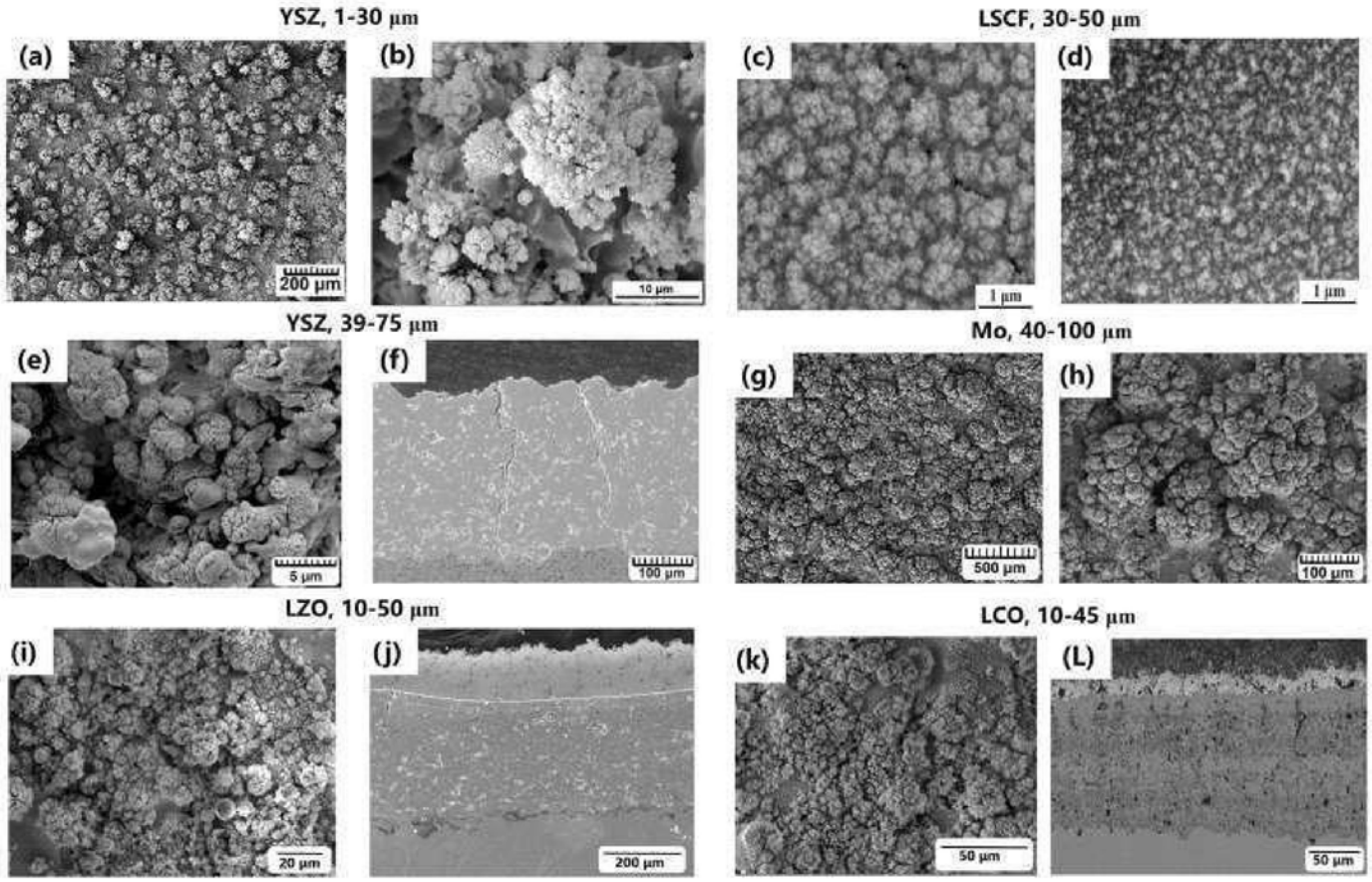

Fig. 25. Microstructures of the coatings produced through ALPS: top surfaces of the (a,b) YSZ coating produced using Metco 6700 8YSZ powder (d = 1–30 μm); (c,d) $La_{0.6}Sr_{0.4}Co_{0.2}Fe_{0.8}O_{3-\delta}$ coating (original powder diameter = 30–50 μm); and (e) YSZ coating (original powder diameter = 39–75 μm); (f) cross-section of the coating in (e); (g,h) top surfaces of the Mo coating (original powder diameter = 40–100 μm); top surface and cross-section of (i,j) $La_2Zr_2O_7$ coating (original powder diameter = 10–50 μm); and (k,l) $La_2Ce_2O_7$ coating (original powder diameter = 10–45 μm) [90,148–150] (Reproduced with permission ©Springer Nature, AIP Publishing, IOP Publishing Ltd & Elsevier B·V.).

YSZ coating. Porous layers were formed immediately at the interface between the CMAS droplets and substrate, which acted as an air barrier to prevent further penetration of CMAS into the coating [116].

Therefore, relative to conventional APS methods, ALPS processing allows the utilization of a wide array of deposition parameters, such as the spraying distance, particle velocity, and substrate temperature. This method can also be performed using low output power and less working noise (≤80 dB). The microstructures of commonly produced coatings contain vertical cracks and exhibit multiporous quasi-columnar structures. Hence, the coatings exhibit excellent bonding strength, surface roughness, hardness, and thermal isolation properties. The microscale island protrusions with nanosized villous structures on the top surface of the coatings effectively hinder the flattening and spreading of CMAS droplets, which is particularly beneficial for the production of thermal barrier coatings.

5. Low pressure plasma spraying system at 50–10^5 Pa

5.1. LPPS and PS-PVD processing

Low-pressure (or very low) plasma spray (LLPS) technology has been proposed for the deposition of dense metallic thin films and coatings over large areas because of its lower cost and higher deposition efficiency than those of conventional PVD methods. The deposition rate (e.g., 5 μm·min^{-1}) in LPPS is approximately an order of magnitude higher than those of the traditional PVD and CVD processes (e.g.,0.5 μm·min^{-1}). This method allows the fabrication of coatings for critical turbine engine parts and medical implants [152]. Furthermore, the velocities of the plasma gas and the corresponding particle flow during LPPS were considerably higher than those attained using conventional plasma spray methods. Typically, a high-output power plasma torch is used in LPPS, which allows the rapid deposition of abundant vapors from ceramic powders, such as YSZ, GZO, and LCO, for the synthesis of thermal barrier coatings [94,153,154]. The microstructures of these ceramic coatings exhibit quasi-columnar or EB-PVD-like columnar structures. In the industry, this method is commonly known as PS-PVD. It is performed under very low pressure conditions (50–200 Pa) [155]. PS-PVD has received considerable research attention, particularly for studies on the synthesis of coatings for aerospace, automobile, and nuclear power applications.

Fig. 26 shows photographs of the low-pressure plasma jet used for spraying from 50 to 10^5 Pa. Regardless of the composition of the plasma torch (Ar–H_2 or Ar–He mixture gases), bright Mach Dick and shock waves were observed near the torch nozzle, and low-pressure plasma jets expanded abruptly along the radial and axial directions. Hence, the spraying distance can be as long as 1500 mm, which provides ultralong heating and motion distances for the injected powders. The current PS-PVD deposition parameters can be found in Ref. 13. To deposit a YSZ coating with a quasi-columnar structure, the input current of the plasma torch must be in the range of 2000–2600 A using Ar and He gases. Finally, the powder feed rate must be within 0.5–20 g·min^{-1}, which is significantly lower than that required for conventional APS methods (e.g., 30–70 g·min^{-1}).

A typical commercial PS-PVD system is shown in Fig. 27, which is

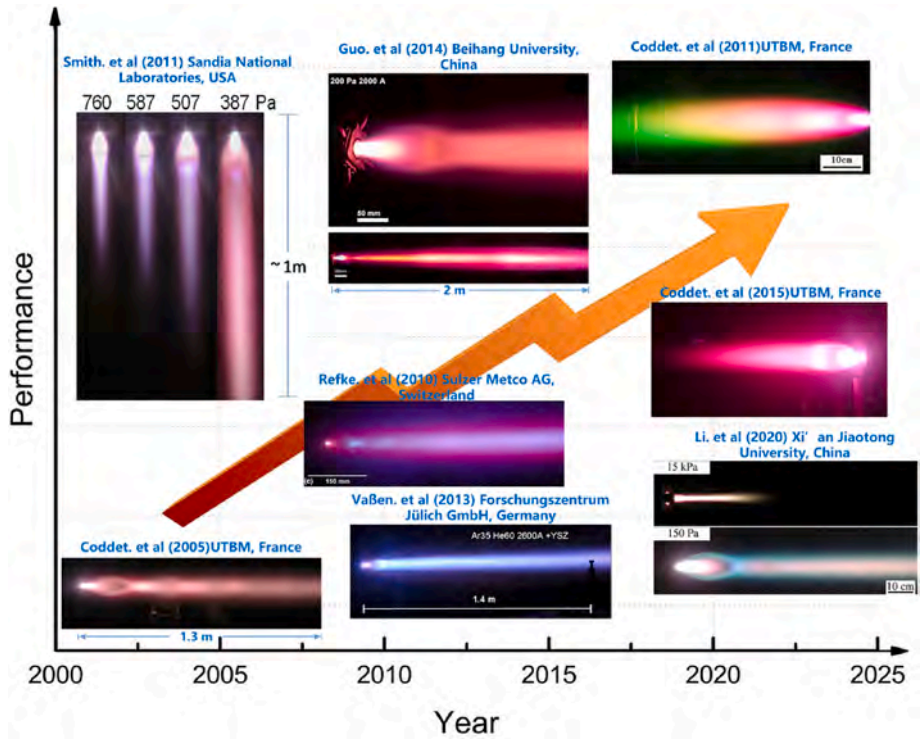

Fig. 26. History and developments of low-pressure plasma spraying [152,155–161] (Reproduced with permission © Springer Nature & Elsevier B·V.).

composed of a power supply, gas supply, powder supply, pump, vacuum chamber, plasma gun, cooling unit, wires, and cables. Fig. 27-a shows a schematic of the low-vacuum chamber unit, which is an important components of the PS-PVD system. It was used to maintain a low-pressure environment during plasma spraying. The length of the plasma jet along the axial direction increased with increasing input power and decreasing chamber pressure (Fig. 27-e to Fig. 27-g). Similarly, the plasma jet expanded in the radial direction. However, the low-pressure chamber as also presents huge challenges for the understanding of the deposition mechanisms in the PS-PVD method. The heat and mass transfer processes within a distance as high as 1500 mm between the supersonic plasma flow and nanoparticles; production of quasi-columnar coatings from vapor, droplets, and solid particles; and control of the vaporization and deposition of abundant vapors during the PS-PVD process are not well understood.

Computational fluid dynamic modeling of PS-PVD processing (P = 200 Pa, I = 2000 A, 30 SLPM Ar+60 SLPM helium) was performed, as shown in Fig. 28. The RSM model was used in the simulation and was found to be suitable for high swirling flow during the PS-PVD process [163–166], which corresponds well with the simulation results of previously reported studies [167–169]. High-value distribution areas were located inside the plasma torch. Considering the axial attenuation profile, the plasma temperature gradually decreases as the distance increases. However, the axial pressure and velocity vary differently in the Mach disk area outside the torch nozzle. The plasma jet expanded after it was injected from a torch nozzle (diameter = 27.5 mm). Similar to the experimental results, the high-velocity flow induced shockwaves near the torch nozzle. A substrate with a diameter of 300 mm was placed 1500 mm from the torch nozzle. The angle of the flow pattern of the plasma jet impinging perpendicularly to the substrate increased. The flow streamlines along the radial direction of the velocity boundary layer of the substrate are bent. The experimental temperature and velocity distributions of the plasma jet completely cover the top surface area of the substrate [13].

The velocity and temperature distributions near the torch nozzle are shown in Fig. 28. An apparently high-temperature arc was generated between the cathode tip and the anode. The predicted maximum velocity at the torch nozzle is greater than 6000 $m\,s^{-1}$. The plasma gas was ejected through a divergent nozzle, which allowed it to expand along the radial direction. Outside the torch area, a bright Mach disk initially formed close to the torch nozzle. A closed stagnation zone formed because the loss of the total pressure behind the Mach disk exceeded the losses behind the compression shock in the peripheral region of the jet. Therefore, the gas stream at the obstacle surface cannot flow outward from the obstacle center [170]. The calculations reveal that the irregular reflections of the formed shocks from the symmetry axis produced a shear layer that promoted the formation of a region with a reverse flow behind the Mach disk [171]. Under the employed conditions, the predicted maximum Mach number was 3.58.

Regardless of the mode of injection of the powders, the velocity and temperature profiles at the cross-section of the torch nozzle are important initial conditions for plasma spraying. Bolot and Coddet (1997) and Vardelle et al. (1998) determined the velocity and temperature distributions during APS through numerical simulations [172–174]. The results of these works have been revised and widely applied in subsequent studies. However, the results cannot be directly used for LPPS torches because of the large differences between the operating parameters of the two methods. For example, the input current of the PS-PVD torch ranges from 2000 to 2600 A (Tables 1 and 7), whereas that of most commercial APS torches varies from 400 to 800 A. The differences in the input current requirements potentially caused a significant difference between the current density distributions at the cathode tip of the PS-PVD and APS torches.

The pressure distributions at the cross-section of the PS-PVD torch (MC-100, Medicoat AG, Switzerland) at chamber pressures of 50, 100, 200, and 1000 Pa are investigated. The internal pressure of the plasma torch ranged from 6000 to 7500 Pa. As the distance increased, the internal pressure decreased to as low as the chamber pressure except in the plasma jet shock area. The plasma gas pressure at the cross-section of the torch nozzle changed marginally as the chamber pressure varied from 50 to 1000 Pa. The plasma gas pressure (P_{out}, Pa) profile at the torch nozzle (chamber pressure = 200 Pa) follows a Gauss–Amp distribution, which

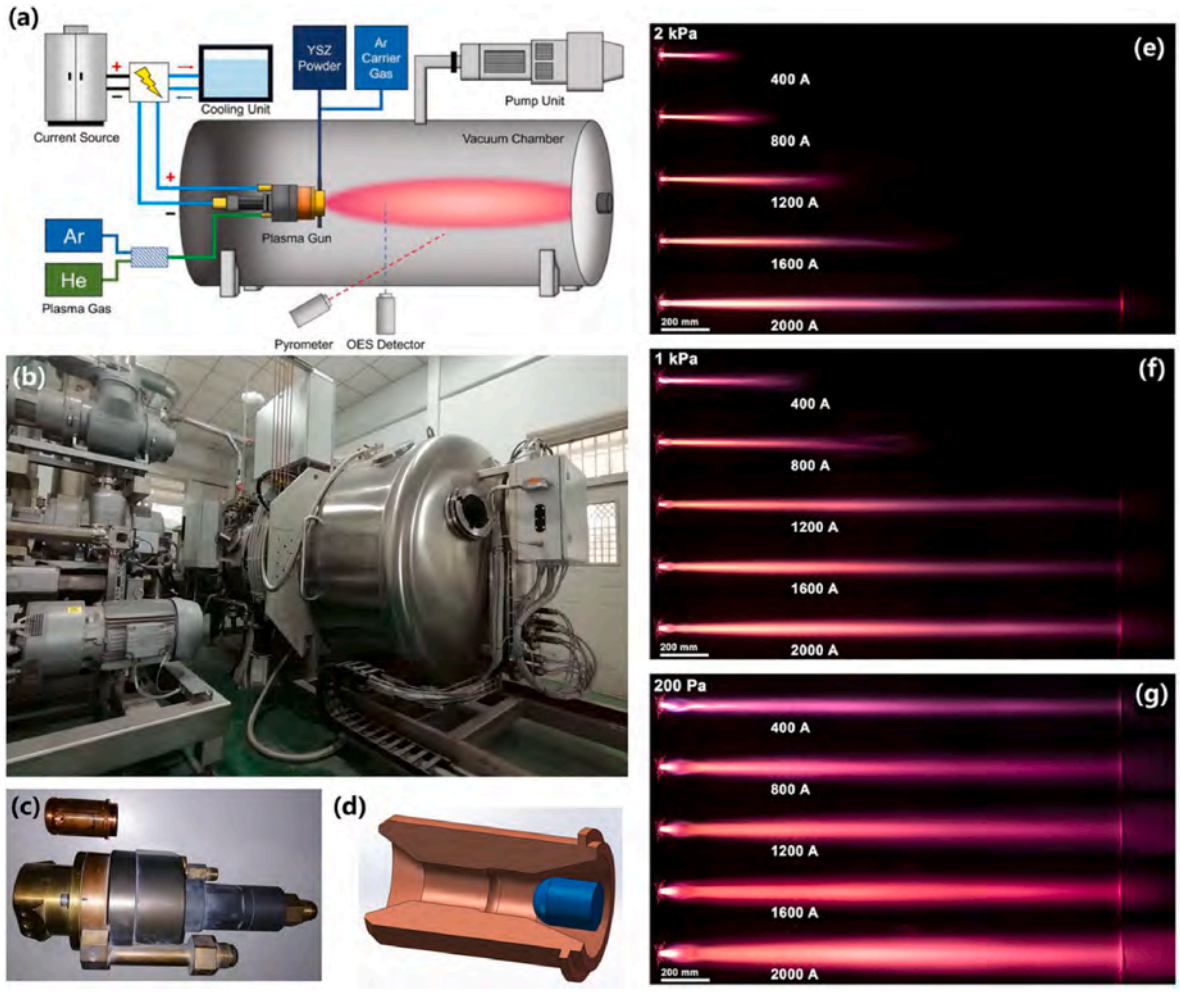

Fig. 27. (a) Schematic and (b) photograph (Beihang University) of the PS-PVD system [13]; (c) plasma spray torch used in this system and (d) its internal structure. Variation of the plasma jet length at chamber pressures of (e) 2000, (f) 1000, and (g) 200 Pa [162] (Reproduced with permission © Elsevier B·V.).

is a function of the torch nozzle radius (*r*, mm) in Eq. (7) [13].

$$P_{out} = -798.18 + 8140.80 \times e^{-\frac{(r-0.01)^2}{80.78}} \quad (7)$$

where P_{out} is in Pa and r is in mm.

The plasma gas temperature (T_{out}, K) and velocity (V_{out}, $m{\cdot}s^{-1}$) profiles at the torch nozzle can be fitted as polynomial functions of the torch nozzle radius (*r*, mm), as shown in Eqs. (8) and (9), respectively:

$$T_{out} = 9078.32312 - 2.06764 \times r + 11.24426 \times r^2 + 0.0872 \times r^3 - 0.74899 \times r^4 - 7.98488 \times 10^{-4} \times r^5 + 0.01112 \times r^6 - 4.28153 \times 10^{-7} \times r^7 - 5.01671 \times 10^{-5} \times r^8 + 1.43629 \times 10^{-8} \times r^9 \quad (8)$$

$$V_{out} = 5976.22964 - 6.56933 \times r + 16.75847 \times r^2 + 0.27536 \times r^3 - 0.90256 \times r^4 - 0.00346 \times 10^{-4} \times r^5 + 0.0843 \times r^6 + 1.76383 \times 10^{-5} \times r^7 - 2.80536 \times 10^{-5} \times r^8 - 3.2315 \times 10^{-8} \times r^9 \quad (9)$$

Owing to the large diameter of the plasma torch (Fig. 29-b), the maximum temperature of the PS-PVD torch at the nozzle exit was not higher than that of the conventional plasma spray torches, even though the input power requirement of the PS-PVD torch was the highest. Moreover, at a constant input current, the temperature distribution at the torch exit during PS-PVD was marginally affected by the variation in the chamber pressure. The maximum velocity at the PS-PVD torch exit was almost four times that at the other plasma spray torches (Fig. 29-c). Figs. 29-c and 29-d summarize the numerically predicted maximum velocity and temperature of plasma gases over the last 20 years. A summary of the operating parameters is listed in Ref. 13. Most of the predicted maximum velocities under different chamber pressures ranged from 5000 to 7000 $m\ s^{-1}$. The predicted maximum temperature was greater than 10,000 K, except for some special cases.

Fig. 30 shows the velocity and temperature distributions at the cross-section of a low-pressure plasma jet at spraying distances of 1000 and 1200 mm, which are the commonly chosen parameters for the plasma spraying of ceramic coatings. The cross-sectional contour distributions revealed that the high-velocity and high-temperature areas were at the center of the plasma jet and distributed in an asymmetric plane. Fig. 30-e and 30-f show the centerline attenuation of the plasma gas velocity and

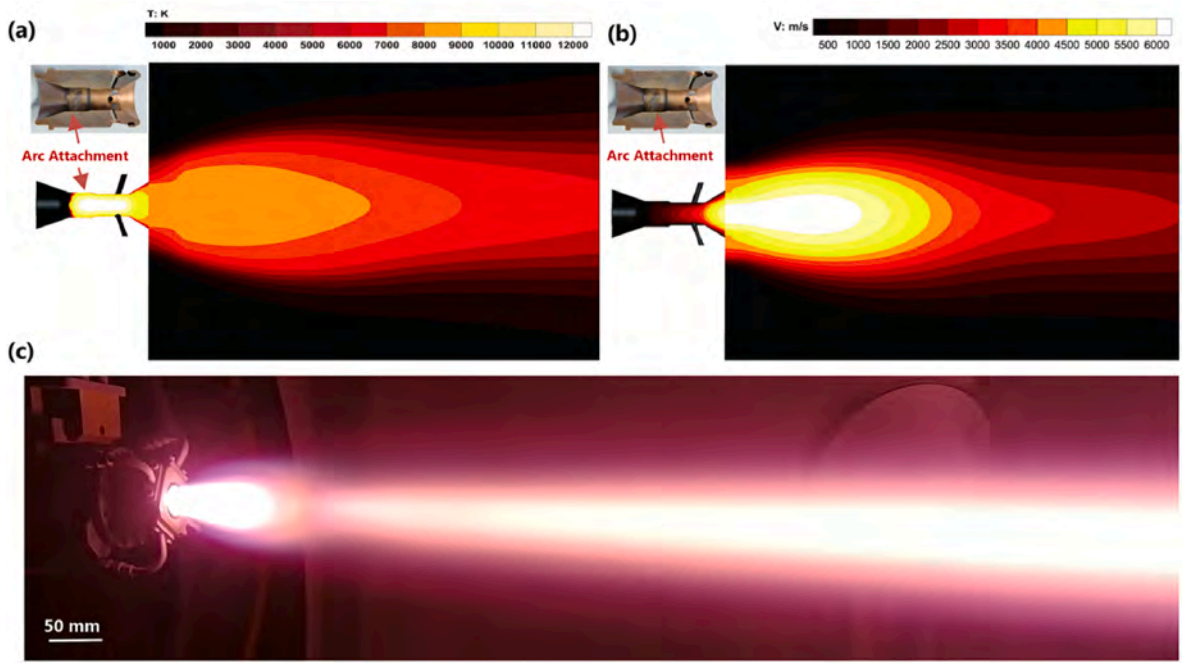

Fig. 28. (a) Temperature and (b) velocity distributions at the plasma jet area near the torch nozzle exit (I = 2000 A, 100 Pa, Ar/He = 30/60 SLPM); (c) observation of the low-pressure plasma jet in the experiment [13] (Reproduced with permission © Elsevier B·V.).

Table 7
Comparison of YSZ particle velocity and temperature in LPPS and PS-PVD processes.

Authors	Operating Conditions	Torch	Chamber Pressure	Particle Size (μm)	Distance (mm)	Particle Velocity (m/s)	Particle Temperature (°C)	Method	Reference
Mark F.Smith& Ronald C. Dykhuizen (1988)	\	\	6.7–8 kPa	Al_2O_3, 44 μm		200–400	\	Laser Velocimeter	[179]
Sodeoka. et al. (2001)	41.6–47.2 kW	Sulzer Metco F4-VB	30–200 kPa	YSZ, 11–106 μm (Metco 204 NS-G)	75–250	180–380	2900–3250	DPV-2000	[71,180]
Schiller. et al. (2001)	30 kW	M3 Laval	10 kPa	YSZ, 5–25 μm	25–250	400–475	/	Laser Doppler Anemometry	[71,181]
Rat. et al. (2003)	30 kW	M3 Laval	1–20 kPa	YSZ, 5–20 μm	10–250	175–375	/	Laser Doppler Anemometry	[71,182]
Refke. et al. (2003)	I = 1500–2600 A 50/110 SLPM Ar/He	Sulzer Metco O3CP	5–20 kPa	YSZ, 5–22 μm	150–550	470–580	2280–2690	DPV-2000	[70]
Coddet. et al. (2005)	15 kW, 40 SLPM Ar	Sulzer MetcoF4-VB	0.5–15 kPa	YSZ, 35–75 μm (Metco 204 B-NB)	150–560	289–666	1720–2425	DPV-2000	[71]
Zhang N, H. L. Liao, C. Coddet (2017)	I = 500 A, 40 SLPM Ar + 8 SLPM H_2	Sulzer MetcoF4-VB	1×10^4–2.5×10^4 Pa	YSZ, 5–22 μm	20–50	260–380	2050–2340	DPV-2000	[160]
Liu & Guo. et al. (2021)	I = 2000 A, 30 SLPM Ar+60 SLPM He	MC-100, Medicoat AG, Switzerland	50–200 Pa	YSZ, 1–30 μm (Metco 6700)	0 (Nozzle Exit)	1659.82 (STDEV = 1093.7)	4336.4 (STDEV = 354.5)	Numerical Simulation	[13]
					1200	709.05 (STDEV = 424.95)	2150.47 (STDEV = 1021.1)		
					1500	395.28 (STDEV = 174.8)	1524.62 (STDEV = 464.3)		

temperature, respectively. At a radius of 350 mm, the velocity and temperature gradients at the cross-section were high. The maximum plasma gas velocities at 1000 and 1200 mm were 495.93 and 572.45 $m\ s^{-1}$, respectively. Conversely, the maximum plasma gas temperatures at spraying distances of 1000 and 1200 mm were 1681.85 K (1408.7 °C) and 1803.81 K (1530.66 °C), respectively. The melting point of the commonly used DD6 single crystal superalloy is in the range from 1360 to 1411 °C [175]. Hence, appropriate experimental spraying parameters should be chosen to prevent melting of the alloy substrate. Although the temperature gradient at the cross -section of the plasma jet is high, this method can be used to deposit coatings on the vanes of aircraft engines in a certain length.

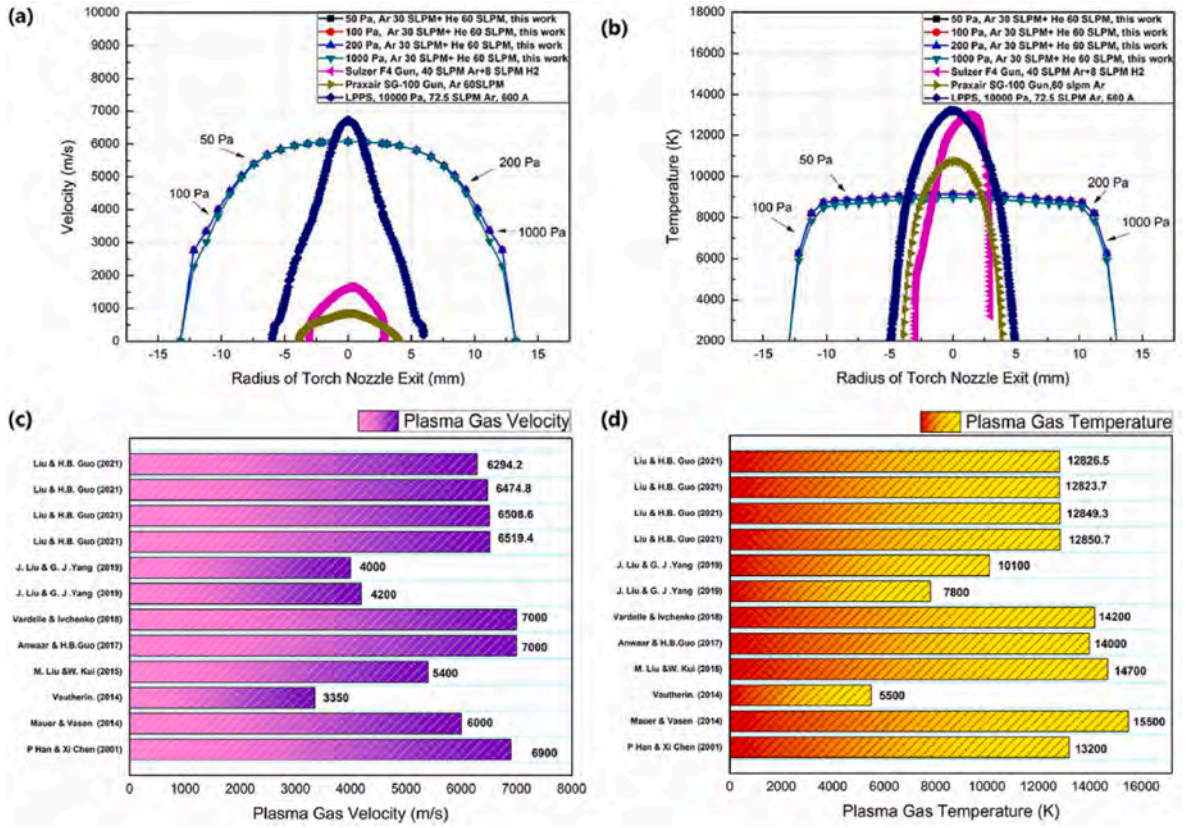

Fig. 29. (a) Velocity and (b) temperature distributions at the cross-section of the torch nozzle at chamber pressures of 50, 100, 200, and 1000 Pa [13]. Predicted maximum (d) velocity and (e) temperature of the low-pressure plasma jets through numerical calculations.

5.2. Multiphase flows and heat transfer in PS-PVD processing

Considering the above mentioned results for PS-PVD plasma jets, the heating and motion profiles of ceramic powders during plasma spraying are presented herein. YSZ particles were injected into the plasma torch using two carrier gas pipes. The fluid characteristics of YSZ particles inside the plasma torch can be found in Ref. 13. Fig. 31 shows the steady flow model of the YSZ particles sprayed at a maximum distance of 2200 mm. The aerodynamic drag, pressure gradient, thermophoretic, and gravitational forces govern the particle flow in the plasma gas.

The YSZ particle diameter distributions are present in Fig. 31 without considering droplet breakup and atomization. The modeling of droplet breakup and atomization in this process was investigated in Ref 13. The tracked trajectories of the particles with diameters ranging from 21 to 30 μm were directed toward the chamber wall at large angles, which may be induced by the high-pressure gradient force of larger particles. On the contrary, particles with diameters ranging from 8 to 21 μm exhibited swirling flow trajectories around the jet axis at a distance of 1.5 *m*. The YSZ mass transfer distribution, which correspond well to the particle diameter distribution in which large particles have high mass concentrations. For a distance of 2.2 *m*, the flight time of the particles was less than 0.1 s. In particular, the flight time of swirling particles varied from 0.4 to 0.7 s.

Fig. 31-d and 31-e show the predicted particle velocity and temperature along the flow trajectories, respectively. Fig. 31-h presents the experimental observations outside the torch nozzle. The particles that flowed close to the torch nozzle exhibited high temperatures close to the boiling point of zirconia (4548 K). However, the maximum particle velocity near the torch nozzle was 6000 $m\ s^{-1}$ in a very small zone, which rapidly decreased along the trajectories.

A comparison of the YSZ particle velocity and temperature in low-pressure plasma spraying at different spraying distances is listed in Table 7. The measured velocity distributions were found to be strongly dependent on the spray chamber pressure using a laser velocimeter. For Al_2O_3 powders with a mean diameter of 44 μm [180], the peak particle velocities ranged from 200 to 400 $m\ s^{-1}$, and the highest particle velocities were recorded at intermediate pressures of approximately 40 kPa (300 Torr). Generally, at a constant distance, the particle velocity is dominated by the chamber pressure and input power of the plasma torch. The particle temperature was slightly higher than the melting point of zirconia (2677 °C). However, at certain spraying distances, the particle temperature decreased. The micro-/nano-deposited units from the atomization, breakup, and resolidification of the in-flight droplets contribute to the formation of quasi-columnar structures through PS-PVD. A smooth quasi-columnar surface structure was easily deposited at the center of the plasma jet. The coating produced at the periphery of the plasma center contains a mass of splashed nanoparticles and unclear interspaces within the quasi-columnar structure on the top surface [176–178].

The calculation of the vapor concentration of zirconia is shown in Fig. 32. The ZrO gas phase is assumed to exist at 298–2500 K [183,184]. Solid zirconia is mainly formed from ZrO_2 vapor, rather than through the reaction of ZrO with O [20,185]. Regardless of the mode of injection of the YSZ powders (one-way or two-way), the high-vapor-concentration area was consistently located near the torch nozzle (Fig. 32-c, Fig. 32-g). Subsequently, the vapor phase was intensely transferred through the plasma jet to distances greater than 1000 mm. In the one-way injection method, the flow streamline of the vapor phase was initially directed to the bottom of the chamber owing to the influence of gravity (Fig. 32-b and 32-d). This observation is similar to that of the tracked trajectories of in-flight particles or droplets during the one-way injection of YSZ powder [13]. In contrast, the flow streamline of the vapor phase was directed to the top of the chamber during two-way injection of the powders (Fig. 32-f and 32-h). Nevertheless, the final deposition tended

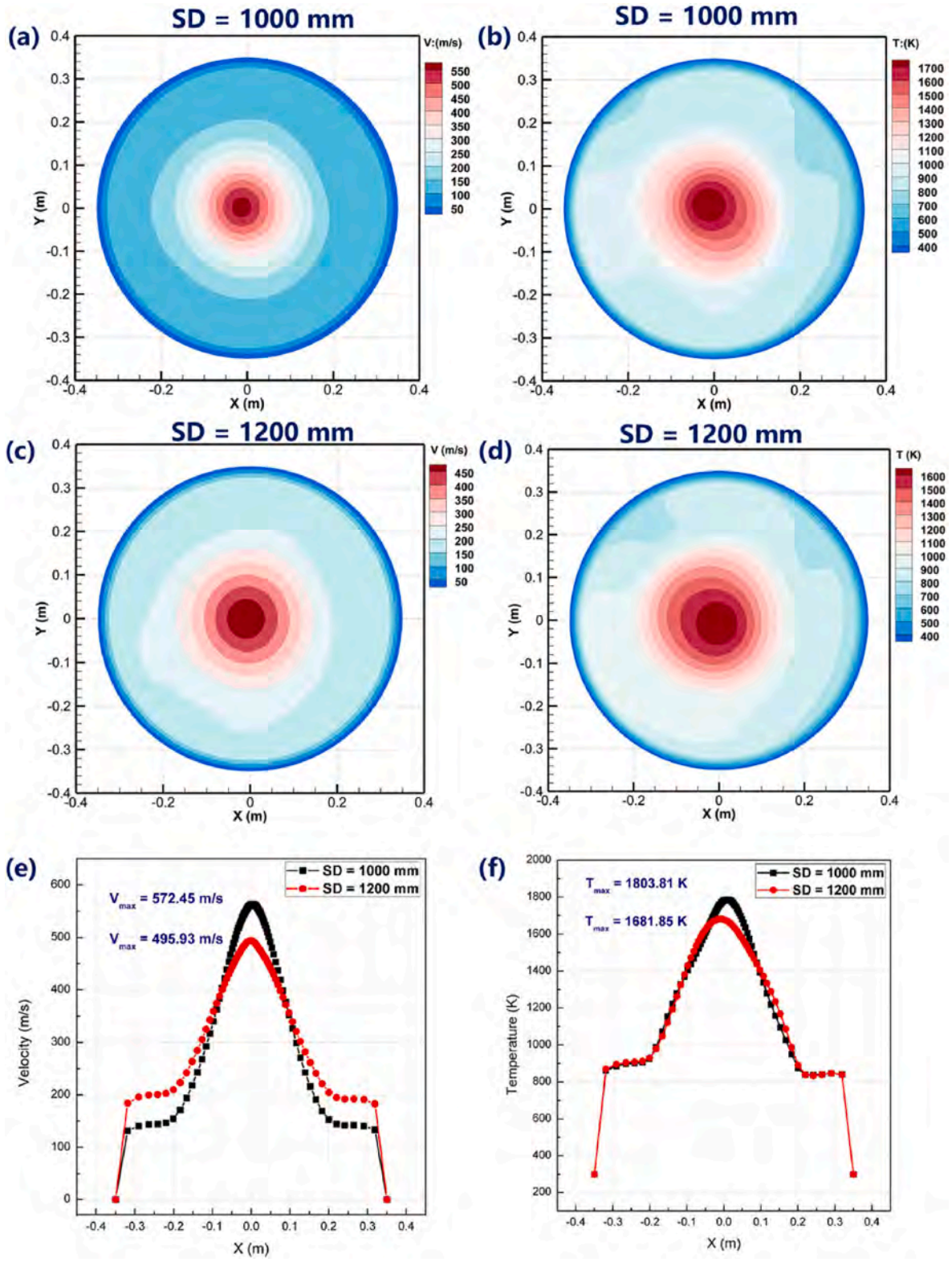

Fig. 30. Predicted velocity and contour distribution at the cross-section of a low-pressure plasma jet (P = 100 Pa, I = 2000 A, 30 SLPM Ar + 60 SLPM He) at spraying distances of (a, b) 1000 and (c, d) 1200 mm; comparison of the average (e) velocity and (f) temperature at the center line of cross-section.

to be perpendicular to the substrate because the plasma jet improved the mass-transfer characteristics during the process. Accordingly, at the anode of the PS-PVD torch (Fig. 32-g and Fig. 32-h), the extent of the evaporation of the YSZ powders during the two-way injection route was approximately 38% at a total feed rate of 8 g·min^{-1}. Considering the vapor concentration of zirconia (Fig. 32-e and 32-f), the deposition rate on the substrate was approximately 5–10 μm·min^{-1} without considering the apparent in-flight particles and droplets. It is worth noting that the highest vapor concentration area was still located at the center of the plane substrate, which explains the formation of smooth cauliflower-like microstructured coatings at the center of the substrate.

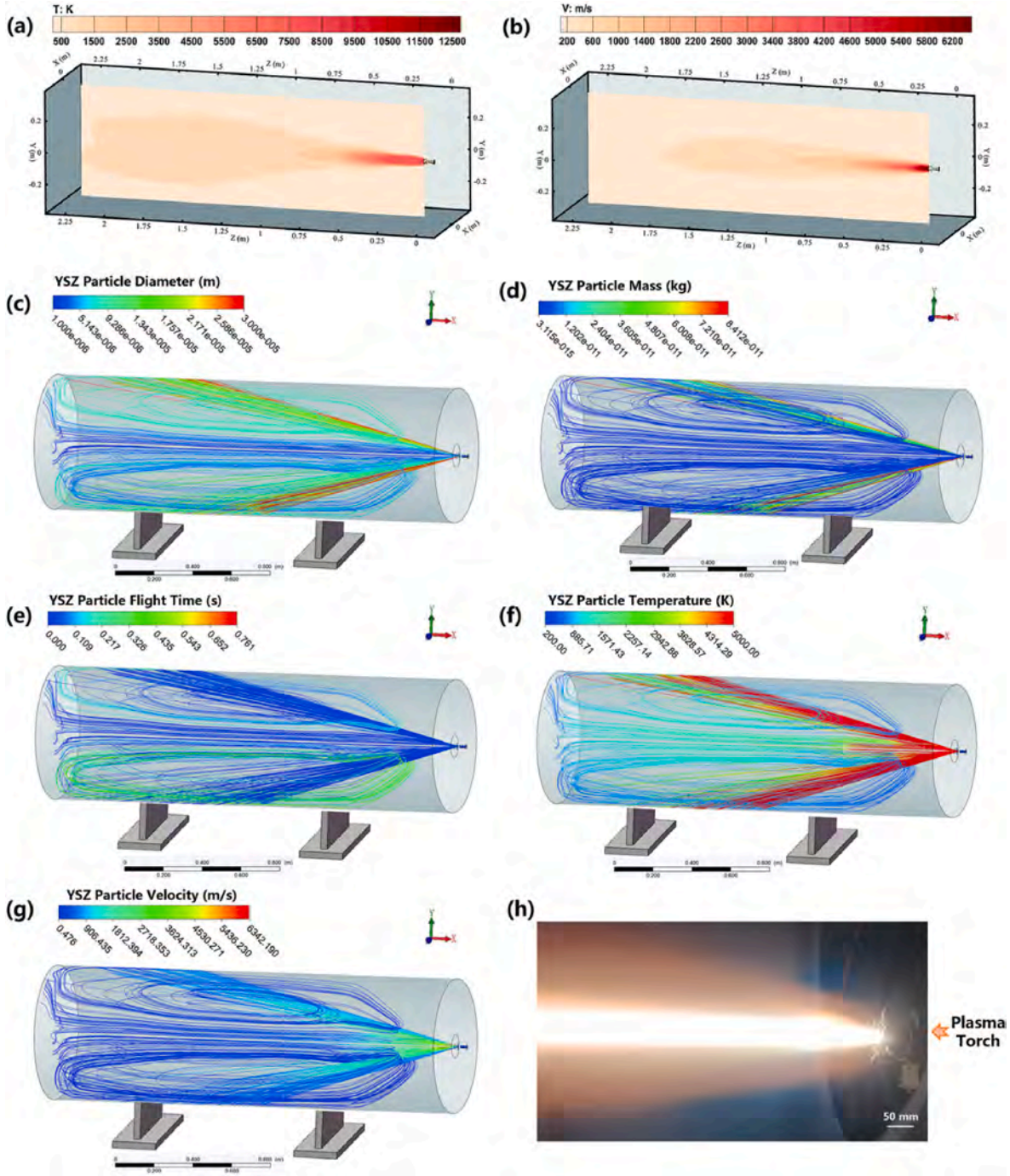

Fig. 31. Modeling of heating and motion of YSZ particles in PS-PVD (P = 200 Pa, I = 2000 A, 30 SLPM Ar + 60 SLPM He, SD = 2200 mm): (a) plasma jet temperature, (b) plasma jet velocity. Particle (c) diameter, (d) temperature, and (e) velocity distributions through two-way injection of the carrier gas (2 × 10 SLPM argon, 2 × 4 g·min^{-1} YSZ). Observation (f) of the region near the torch nozzle with the YSZ particles under the same conditions ([13] reproduced with permission © Elsevier B. V.).

5.3. Depositing of ceramic thermal barrier coatings on blades of aircraft engines through PS-PVD

In the experiment, the depositing of ceramic thermal barrier coatings was carried out for a few minutes. Fig. 33 shows the evolution of the microstructures from single-scan deposition to thin-film coating formation. Uniformly distributed island-like deposits were obtained within 2 s. Thereafter, larger islands with nanosized stable clusters that coagulated from the vapor stream or impinging particles were produced.

With continuous deposition, more islands or droplets fill the spaces formed by the previously deposited particles and form a thin film. Considering the self-shadowing effect of the impinging particles, the local growth rate in the perpendicular direction is higher than that in the horizontal direction. Furthermore, considering the deposited thin films with increasing thicknesses, the surface diffusion coefficients of coatings based on Zr, O, Y, La, Ce, Gd, and Yb increase with the interface temperature [13]. Therefore, coatings typically exhibit a quasi-columnar microstructure with larger diameters at the top surface. The boundaries of the interspaces between the quasi-columns became less apparent with increasing coating thickness.

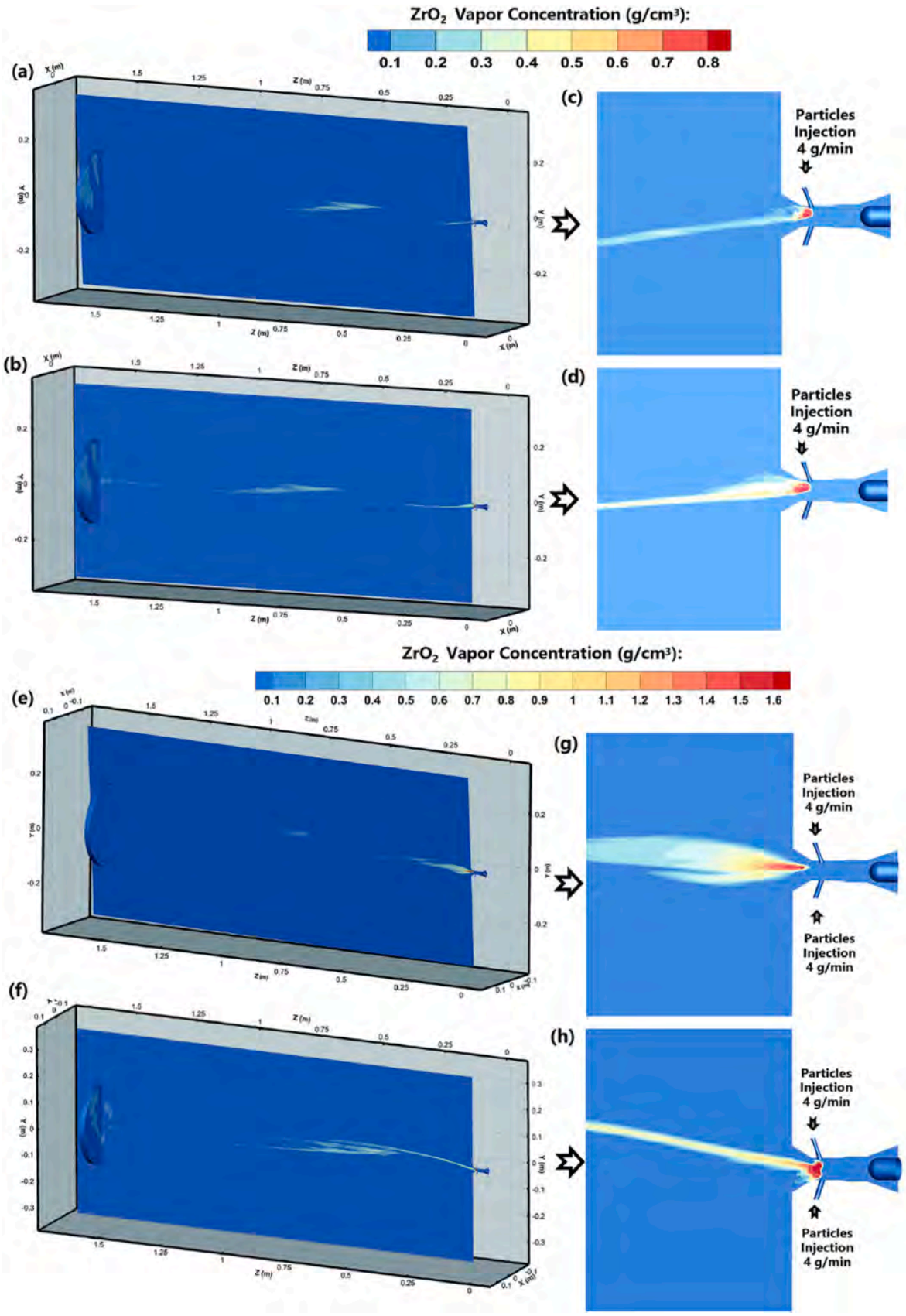

Fig. 32. Transient zirconia vapor distribution in the PS-PVD processing (P = 100 Pa, I = 2000 A, 30 SLPM Ar +60 SPLM He): (a, b) distributions of the continuous flow at an interval of 10 μs through a one-way injection of particles from the plasma torch to the substrate (SD = 1500 mm); (c, d) magnified views nearby the torch nozzle. (e, f) Distributions of the continuous flow at an interval of 10 μs through two-way injection method [13]; (g, h) magnified views nearby the torch nozzle [13].

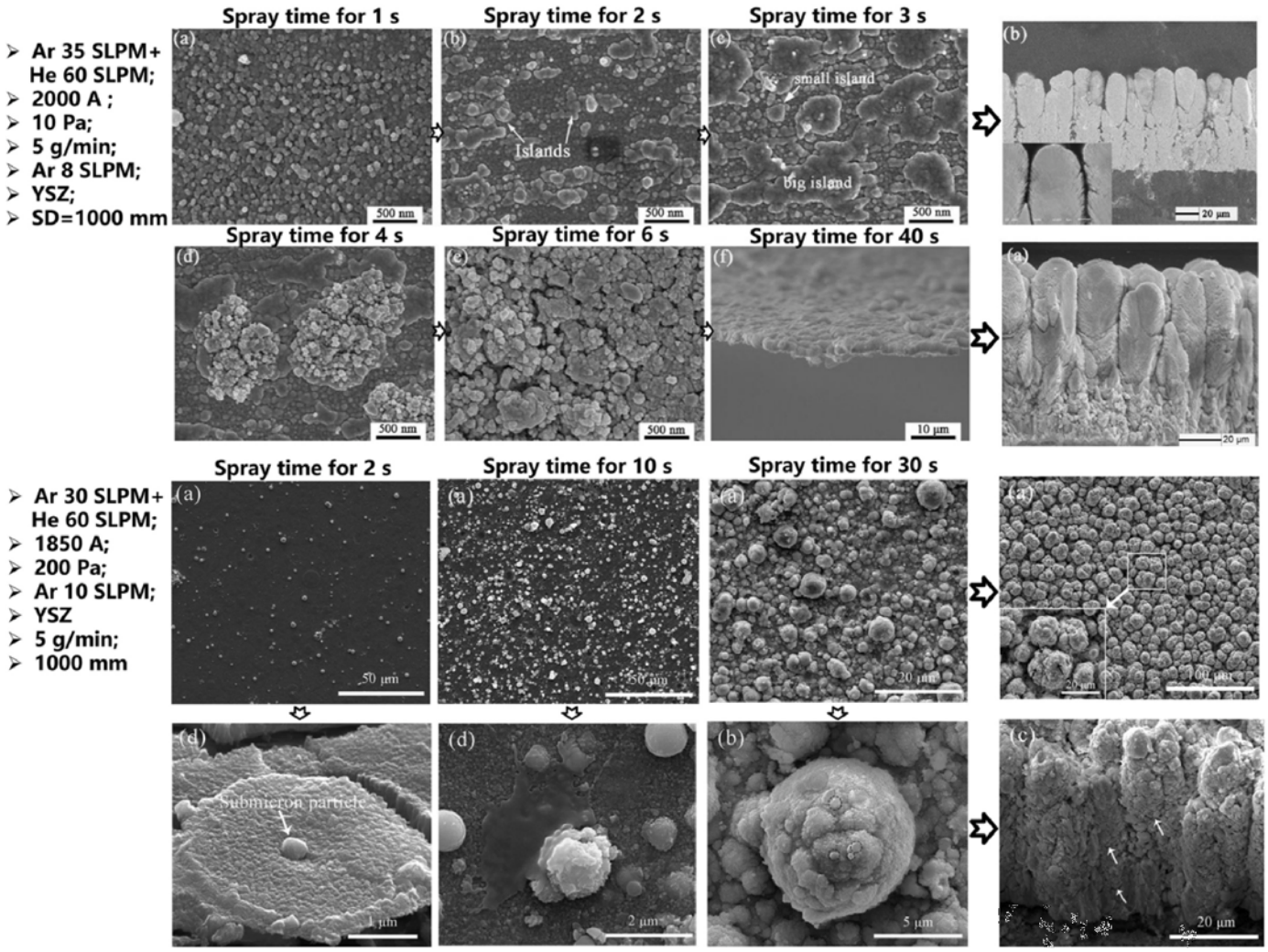

Fig. 33. Depositing of quasi-columnar coatings in PS-PVD [13,186] (Reproduced with permission© Elsevier B·V.).

6. Summary

In this paper, we review the current nontransferred arc plasma spray technology and focus on changes in the multiphase flows and heat transfer mechanisms of the precursor powders and produced coatings. The following conclusions were drawn:

(1) The arc flow instabilities inside the plasma spray torch still induce plasma jet instabilities downstream, which reduce the controllability and reproducibility of spraying the particles.
(2) In addition to solid particle melting, evaporation, and solidification during plasma spraying, liquid column breakup, secondary breakup, and atomization will inevitable occur duo to the cross-flows in internal injection or outside injection ways of plasma spraying. By using a long spraying distance and nano-size powders, in-flight droplet re-solidification, and self-shadowing of impinging particles will also occur.
(3) For APS processing, the influence of the cold carrier gas on the thermal plasma gas was significant under transverse injection of the carrier gas containing the particles. The entrainment of air should be considered in the modeling of Ar plasma jets used in APS to obtain reliable simulation results.
(4) For AMPS technology, the carrier gas containing the powders was supplied from a hollow cathode, which was specifically designed to deposit ceramic or metallic coatings, even at low output powers.
(5) For ALPS technology, the surface temperatures of the YSZ and Al_2O_3 powders were close to the boiling points of the materials. In general, the output power of other conventional APS methods is larger than that required for ALPS. As such, this technology can be used to produce vertical cracks or quasi-columnar YSZ coatings, even under atmospheric conditions.
(6) In PS-PVD technology, heat and mass transfers occur over long distances in a closed chamber. The formation of mixtures of deposition materials containing vapor, droplets, and resolidified solid particles was confirmed by experimental and numerical simulation results. Appropriate and precise spraying parameters should be used for the deposition of coatings on substrates.

7. Outlook and critical challenges

Although extensive research on APS processing has been conducted, further investigations are required to clarify existing problems that have not been fully resolved. Trelles (2018) investigated the basic phenomena in a direct-current arc plasma torch (Fig. 34-a). Although the length and diameter of the plasma torch were both small, the phenomena inside and outside the torch varied significantly. Furthermore, they were found to be complex, three-dimensional, and time-dependent [197]. To date, the

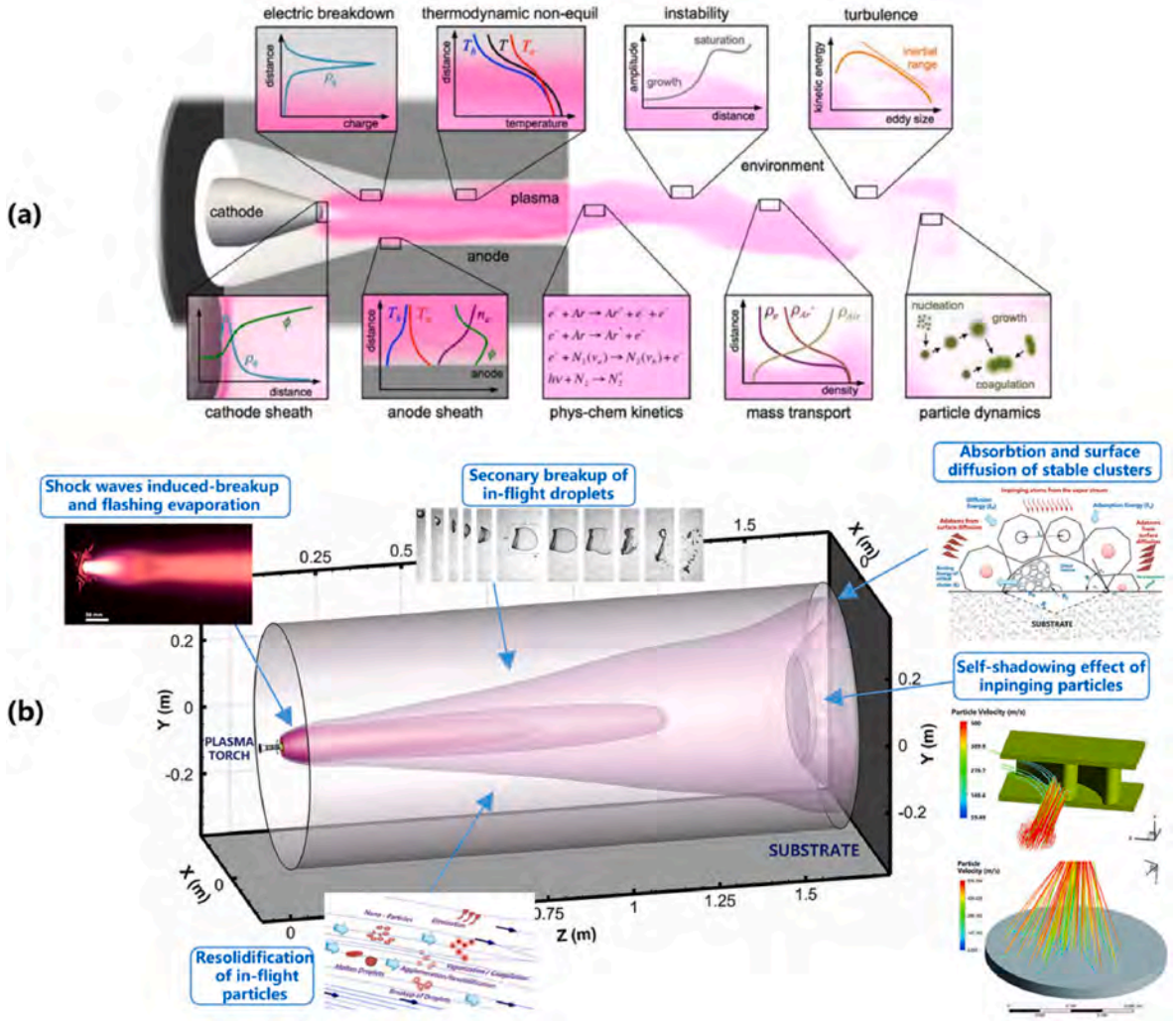

Fig. 34. (a) Understanding phenomena in atmospheric plasma spraying [196] and (b) low-pressure plasma spraying (Reproduced with permission © IOP Publishing Ltd).

computational fluid dynamics (CFD) approach has been employed to simulate APS processing, wherein a set of magnetohydrodynamic equations that include the conservation of mass, momentum, and energy of the plasma gas are used. However, nonequilibrium conditions can be observed extensively in the arc fringes and regions near the electrodes [187]. Although many nonlocal thermodynamic equilibrium (NLTE) models have been developed for APS processing, the chemical non-equilibrium effect should be considered in modeling the arc contraction behavior inside the arc plasma spray torch [188,189]. In addition, the plasma torch, commonly Ar and Ar–H_2 gases, is considered a full plasma gas; that is, the heat transfer between the thermal plasma jet and the cold surrounding air is not considered in most cases during the numerical simulation. The heat transfer phenomenon is considerable, particularly in modeling Ar plasma spraying under atmospheric environments, because the difference in specific heat between Ar and air is high [34]. For PS-PVD processing (Fig. 34-b), the flight distance of the powders was approximately 10 times that of the particles used in APS technology. The flight time of particles in PS-PVD (0.1 to 0.4 s) is at least three orders of magnitude higher than that in APS (1×10^{-4} to 1×10^{-3} s). Moreover, many experimental results have demonstrated that low-pressure plasma jets have larger electron temperature gradients at the torch cross-section [190–192]. For PS-PVD, the nonequilibrium parameter (T_e/T_h) was approximately 1.23–1.28 at a spraying distance in the range 500–1200 mm and chamber pressure of 200 Pa [193]. Therefore, CFD simulations of the LPPS and PS-PVD methods should be performed using NLTE conditions. The data for the electrons and heavy particles in the Ar–He plasma gases should be completely reported.

Moreover, according to the distribution of the K_n number ($K_n = Ma/Re = \lambda/L$) along the axis of the PS-PVD jet in Fig. 35, the actual value of the K_n number at spraying distances ranging from 1000 to 1500 mm was less than 1. However, at a critical length of 1 μm, the value of K_n in the shock area is quite high. Therefore, an advanced multiscale CFD approach should be developed to improve the fidelity and accuracy of the models for LPPS and PS-PVD technologies.

There exists a weak effective electric field of the plasma jet in the atmospheric environment for plasma spraying at an input current of 400 A [194]. Hence, PS-PVD jet should have a more intense effective electric field in the three-dimensional domain from 2000 to 2600 A. Chen Xi reported that the charging time of particles with an average size 10 μm in an Ar plasma jet was on the order of 10^{-11} s [195]. However, the

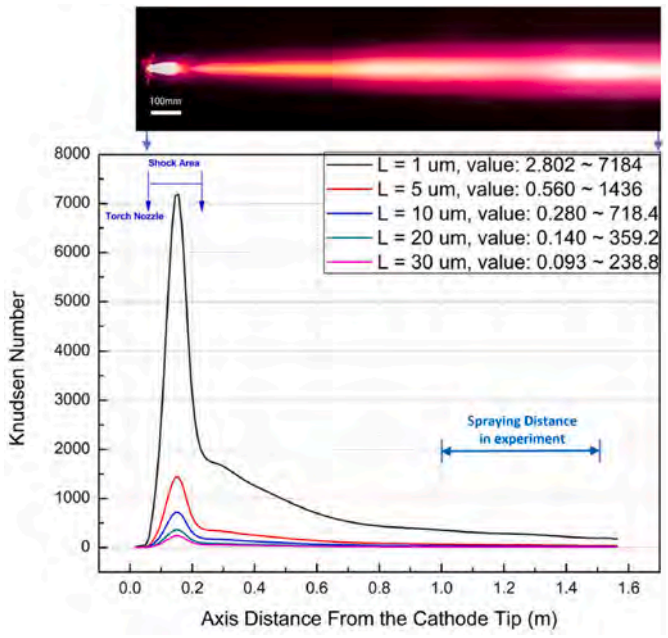

Fig. 35. Distribution of Kn along the axis of the PS-PVD plasma jet (P = 100 Pa, I = 200 A, 30 SLPM Ar + 60 SLPM He).

spraying distance and flight time during APS processing were quite short. The nonlocal electric neutrality induced by NLTE does not need to be considered. In PS-PVD processing, the charging of in-flight particles may or may not induce coagulation. Coagulation and agglomeration of nanoclusters should be further investigated.

Declaration of competing interest

The authors declare that they have no known competing financial interests or personal relationships that could have appeared to influence the work reported in this paper.

Data availability

Data will be made available on request.

Acknowledgments

The authors acknowledge the Massachusetts Green High-Performance Computing Center (MGH - PCC). This work was supported by the National Natural Science Foundation of China (Grant No. 52001017), the National Science and Technology Major Project (No. 2017-VI-0010-0081, 2017-VI-0002-0072, 2021YFB4001400), and Fundamental Research Funds for the Central University. The authors would like to thank Dr. Anthony. B. Murphy (CSIRO Manufacturing, Lindfield, Australia) for guidance on the modeling of plasma gas, and Dr. Wen-ting He (Beihang University) and Dr. Margarita. Baeva (Leibniz Institute for Plasma Science and Technology, Germany) for discussing the nonequilibrium effect in thermal plasmas.The data presented in this paper are available upon the request from the authors.

References

[1] P.L. Fauchais, et al., Thermal Spray Fundamentals: from Powder to Part, Springer Science+Business Media New York, 2014, https://doi.org/10.1007/978-0-387-68991-3_1.
[2] Chang-Jiu Li, C.-X.L. Guan-Jun Yang, Development of particle interface bonding in thermal spray coatings: a review, J. Therm. Spray Technol. 22 (2–3) (2013) 192–206.
[3] Armelle Vardelle, et al., The 2016 thermal spray roadmap, J. Therm. Spray Technol. 25 (8) (2016) 1376–1440.
[4] C.J. Li, G.J. Yang, A. Ohmori, Relationship between particle erosion and lamellar microstructure for plasma-sprayed alumina coatings, Wear 260 (11–12) (2006) 1166–1172.
[5] A.S.M. Ang, C.C. Berndt, A review of testing methods for thermal spray coatings, Int. Mater. Rev. 59 (4) (2014) 179–223.
[6] C.-J.C.-X. Li, Q.-L. Zhang, S.-W. Yao, G.-J. Yang, C.-J.C.-X. Li, Plasma spraying of dense ceramic coating with fully bonded lamellae through materials design based on the critical bonding temperature concept, J. Therm. Spray Technol. 28 (1–2) (2019) 53–62.
[7] J.-T. Gao, J.-H. Li, Y.-P. Wang, C.-J. Li, C.-X. Li, Performance and stability of plasma-sprayed 10 × 10 cm 2 self-sealing metal-supported solid oxide fuel cells, J. Therm. Spray Technol. 30 (4) (2021) 1059–1068.
[8] Shan-Lin Zhang*, Yuan-Bo Shang, Cheng-Xin Li*, Chang-Jiu Li, Vacuum cold sprayed nanostructured La0.6Sr0.4Co0.2Fe0.8O3−δ as a high-performance cathode for porous metal-supported solid oxide fuel cells operating bellow 600 °C, Mater. Today Energy, 2021 21, 100815.
[9] H. Zhang, S. Liu, C. Li, C. Li, Deposition and oxidation behavior of atmospheric laminar plasma sprayed Mo coatings from 200 mm to 400 mm under 20 kW : numerical and experimental analyses, Surf. Coating. Technol. 400 (May) (2020).
[10] J. Xiang, K. Tanaka, F.F. Chen, M. Shigeta, M. Tanaka, A.B. Murphy, Modelling and Measurements of Gas Tungsten Arc Welding in Argon–Helium Mixtures with Metal Vapour, Welding in the World, 2021.
[11] Y. Zhang, F. Cheng, S. Wu, The microstructure and mechanical properties of duplex stainless steel components fabricated via flux-cored wire arc-additive manufacturing, J. Manuf. Process. 69 (July) (2021) 204–214.
[12] D.R. Gunasegaram, A.B. Murphy, A. Barnard, T. Debroy, M.J. Matthews, L. Ladani, D. Gu, Towards developing multiscale-multiphysics models and their surrogates for digital twins of metal additive manufacturing, Addit. Manuf. 46 (April) (2021).
[13] S.-H. Liu, J.P. Trelles, A.B. Murphy, W.-T. He, J. Shi, S. Li, C.-J. Li, C.-X. Li, H.-B. Guo, Low-pressure plasma-induced physical vapor deposition of advanced thermal barrier coatings: microstructures, modelling and mechanisms, Materials Today Physics 21 (2021): 100481.
[14] T. Liu, S. Yao, L. Wang, G. Yang, C. Li, C. Li, Plasma-sprayed thermal barrier coatings with enhanced splat bonding for CMAS and corrosion protection, J. Therm. Spray Technol. 25 (January) (2016) 213e221.
[15] T. Liu, S. Zhang, X. Luo, G. Yang, C. Li, C. Li, High heat insulating thermal barrier coating designed with large two-dimensional inter- lamellar pores, J. Therm. Spray Technol. 25 (1) (2016) 222e230.
[16] S. Pal, A. Deore, N.M. Alford, A. Templeton, S.J. Penn, High temperature thermal properties of columnar yttria stabilized zirconia thermal barrier coating performed, J. Phys. Conf. 745 (2016): 032012.
[17] D. Zhou, J. Malzbender, Y.J. Sohn, O. Guillon, R. Vaßen, Sintering behavior of columnar thermal barrier coatings deposited by axial suspension plasma spraying (SPS), J. Eur. Ceram. Soc. 39 (2e3) (2019) 482e490.
[18] D. Zhou, D.E. Mack, E. Bakan, G. Mauer, D. Sebold, O. Guillon, R. Vaßen, Thermal cycling performances of multilayered yttria-stabilized zirconia/gadolinium zirconate thermal barrier coatings, J. Am. Ceram. Soc. 103 (3) (2020) 2048e2061.
[19] S.H. Liu, C.X.C.J. Li, H.Y. Zhang, S.L. Zhang, L. Li, P. Xu, G.J. Yang, C.X.C.J. Li, A novel structure of YSZ coatings by atmospheric laminar plasma spraying technology, Scripta Mater. 153 (2018) 73e76.
[20] S.-H. Liu, J.P. Trelles, C.-J. Li, H.B. Guo, C.-X. Li, Numerical analysis of the plasma-induced self-shadowing effect of impinging particles and phases transformation in a novel long laminar plasma jet, J. Phys. Appl. Phys. 53 (2020): 375202.
[21] X. Wang, D. Fan, J. Huang, Y. Huang, Numerical simulation of arc plasma and weld pool in double electrodes tungsten inert gas welding, Int. J. Heat Mass Tran. 85 (2015) 924–934.
[22] S. Tashiro, T. Zeniya, K. Yamamoto, M. Tanaka, K. Nakata, A.B. Murphy, E. Yamamoto, K. Yamazaki, K. Suzuki, Numerical analysis of fume formation mechanism in arc welding, J. Phys. Appl. Phys. 43 (43) (2010).
[23] E. Pfender, J. Fincke, R. Spores, Entrainment of cold gas into thermal plasma jets, Plasma Chem. Plasma Process. 11 (4) (1991) 529–543.
[24] X. Chen, W. Pan, X. Meng, K. Cheng, D. Xu, C. Wu, What do we know about long laminar plasma jets, Pure Appl. Chem. 78 (6) (2006) 1253–1264.
[25] D.Y. Xu, X. Chen, W. Pan, Effects of natural convection on the characteristics of a long laminar argon plasma jet issuing horizontally into ambient air, Int. J. Heat Mass Tran. 48 (15) (2005) 3253–3255.
[26] A.B. Murphy, D. Uhrlandt, Foundations of high-pressure thermal plasmas, Plasma Sources Sci. Technol. 27 (6) (2018).
[27] H. Li, E. Pfender, X. Chen, Application of Steenbeck's minimum principle for three-dimensional modelling of DC arc plasma torches, J. Phys. Appl. Phys. 36 (9) (2003) 1084–1096.
[28] J.P. Trelles, J.V.R. Heberlein, E. Pfender, Non-equilibrium modelling of arc plasma torches, J. Phys. Appl. Phys. 40 (19) (2007) 5937–5952.
[29] W.X. Pan, X. Meng, H.J. Huang, C.K. Wu, Effects of anode temperature on the arc volt-ampere characteristics and ejected plume property of a low-power supersonic plasma, Plasma Sources Sci. Technol. 20 (6) (2011): 65006.
[30] C.R. Britton, in: I.A. Bucklow (Ed.), 12th International Conference on Thermal Spraying Proceedings, Welding Institute, London, 1989, p. 465.
[31] J.L. Marque ′s, G. Forster, J. Schein, Multi-electrode plasma torches: motivation for development and current state-of-the- art, Open Plasma Phys. J. 1 (2) (2009) 89–98.
[32] K. Osaki, O. Fukumasa, A. Kobayashi, High thermal efficiency-type laminar plasma jet generator for plasma processing, Vacuum 59 (2000) 47–54.

[33] O.P.S.A.V. Smirnov, Advanced oxide powders processing based on cascade plasma, J. Phys. Conf. 550 (550) (2014): 12017.
[34] S.H. Liu, S. Lin, Z. Cheng, X. Li, L. Li, J. Hua, Sen-Hui Liu, Shan-Lin Zhang, Cheng-Xin Li, Li Lu, Jia-Hua Huang, Juan Pablo Trelles, B. Anthony, C.L. Murphy, Generation of long laminar plasma jets: experimental and numerical analyses, Plasma Chem. Plasma Process. 1–11 (2019): 123456789.
[35] M. Javad, M.I. Boulos, Thermal plasma sources: how well are they adapted to process needs? Plasma Chem. Plasma Process. 3 (35) (2015) 421–436.
[36] R. Chidambaram Seshadri, S. Sampath, R. Chidambaram, S. Sanjay, Characteristics of conventional and cascaded arc plasma spray-deposited ceramic under standard and high-throughput conditions, J. Therm. Spray Technol. 28 (4) (2019) 690–705.
[37] M.F. Zhukov, Electric arc generators of thermal plasma (review), Plasma Dev. Oper. 5 (1) (1996) 1–36.
[38] https://www.oerlikon.com/en/meta-navigation/search-result/?q=9M.
[39] https://www.oerlikon.com/metco/en/products-services/thermal-spray-equipment/thermal-spray-components/spray-guns/plasma/external-atmospheric-plasma/sinplexpro%E2%84%A2/.
[40] https://www.oerlikon.com/ecoma/files/DSE-0062.2_TriplexPro-210_EN.pdf?download=true.
[41] https://www.oerlikon.com/en/search-results/?q=SinplexPro&type=files.
[42] https://www.oerlikon.com/en/search-results/?q=03CP&type=files.
[43] https://www.praxairsurfacetechnologies.com/en/materials-and-equipment/coating-equipment/thermal-spray-coating-systems/plasma-spray.
[44] M. Baeva, M.S. Benilov, N.A. Almeida, D. Uhrlandt, Novel non-equilibrium modelling of a DC electric arc in argon, J. Phys. Appl. Phys. 49 (2016): 245205.
[45] H. Huang, W. Pan, C. Wu, Arc root motion in an argon-hydrogen DC plasma torch, IEEE Trans. Plasma Sci. 36 (4 PART 1) (2008) 1050–1051.
[46] Z. Duan, J. Heberlein, arc instabilities in a plasma spray torch, J. Therm. Spray Technol. 11 (March) (2002) 44–51.
[47] E. Nogues, M. Vardelle, P. Fauchais, P. Granger, Arc voltage fluctuations : comparison between two plasma torch types, Surf. Coating. Technol. 202 (18) (2008) 4387–4393.
[48] Juan Pablo Trelles, J.H. Emil Pfender, Multiscale finite element modeling of arc dynamics in a DC plasma torch, Plasma Chem. Plasma Process. 26 (6) (2006) 557–575.
[49] E. Pfender, Plasma jet behavior and modeling associated with the plasma spray process, Thin Solid Films 238 (1994) 228–241.
[50] C.L. Ng, R. Sankarakrishnan, K.A. Sallam, Bag breakup of nonturbulent liquid jets in crossflow, Int. J. Multiphas. Flow 34 (3) (2008) 241–259.
[51] C. Wang, R. Xu, Y. Song, P. Jiang, Study on water droplet flash vaporization in vacuum spray cooling, Int. J. Heat Mass Tran. 112 (2017) 279e288.
[52] H. Xiong, W. Sun, Investigation of droplet atomization and evaporation in solution precursor plasma spray coating, Coatings 7 (11) (2017).
[53] E. Sher, T. Bar-Kohany, A. Rashkovan, Flash-boiling atomization, Prog. Energy Combust. Sci. 34 (4) (2008) 417–439.
[54] S.V. Apte, M. Gorokhovski, P. Moin, LES of atomizing spray with stochastic modeling of secondary breakup, Int. J. Multiphas. Flow 29 (9) (2003) 1503–1522.
[55] J. Fazilleau, C. Delbos, V. Rat, J.F. Coudert, P. Fauchais, B. Pateyron, Phenomena involved in suspension plasma apraying part 1: suspension injection and behavior, Plasma Chem. Plasma Process. 26 (4) (2006) 371–391.
[56] S. Sampath, On the response of different particle state sensors to deliberate process variations, J. Therm. Spray Technol. 20 (5) (2011) 1035–1048.
[57] M.P. Planche, R. Bolot, C. Coddet, In-flight characteristics of plasma sprayed alumina particles : measurements , modeling , and comparison, J. Therm. Spray Technol. 12 (March) (2003) 101–111.
[58] Y.P. Wan, J.R. Fincke, S. Sampath, V. Prasad, H. Herman, Modeling and experimental observation of evaporation from oxidizing molybdenum particles entrained in a thermal plasma jet, Int. J. Heat Mass Tran. 45 (2002) 1007–1015.
[59] E. Dalir, A. Dolatabadi, J. Mostaghimi, Modeling the effect of droplet shape and solid concentration on the suspension plasma spraying, Int. J. Heat Mass Tran. (2020) 161.
[60] E. Dalir, C. Moreau, A. Dolatabadi, Three-dimensional modeling of suspension plasma spraying with arc voltage fluctuations, J. Therm. Spray Technol. 27 (8) (2018) 1465–1490.
[61] T.C. Totemeier, R.N. Wright, W.D. Swank, FeAl and Mo-Si-B intermetallic coatings prepared by thermal spraying, Intermetallics 12 (12) (2004) 1335–1344.
[62] S. Sampath, X. Jiang, J. Matejicek, L. Prchlik, A. Kulkarni, A. Vaidya, Role of thermal spray processing method on the microstructure, residual stress and properties of coatings: an integrated study for Ni–5 wt.%Al bond coats, Materials Science and Engineering A-Structural Materials Properties Microstructure and Processing 364 (1) (2004) 216–231.
[63] S.P. Mates, D. Basak, F.S. Biancaniello, S.D. Ridder, J.C. Geist, Calibration of a two-color imaging pyrometer and its use for particle measurements in controlled air plasma spray experiments, J. Therm. Spray Technol. 11 (2) (2002) 195–205.
[64] K. Shinoda, S. Liang, S. Sampath, R.J. Gambino, Processing effects on in-flight particle state and functional coating properties of plasma-sprayed manganese zinc ferrite, Materials Science and Engineering B-Advanced Functional Solid-State Materials 176 (1) (2011) 22–31.
[65] A. Valarezo, S. Sampath, An integrated assessment of process-microstructure-property relationships for thermal-sprayed NiCr coatings, J. Therm. Spray Technol. 20 (6) (2011) 1244–1258.
[66] Z. Yin, S. Tao, X. Zhou, C. Ding, Particle in-flight behavior and its influence on the microstructure and mechanical properties of plasma-sprayed Al2O3 coatings, J. Eur. Ceram. Soc. 28 (6) (2008) 1143–1148.
[67] H.B. Parizi, J. Mostaghimi, L. Pershin, H.S. Jazi, Analysis of the microstructure of thermal spray coatings: a modeling approach, J. Therm. Spray Technol. 19 (4) (2010) 736–744.
[68] V. Debout, et al., Investagetion of in-light particle characteristics and Microstructural effects on optical properties of YSZ plasma-sprayed coatings, High Temp. Mater. Process. 11 (2007) 309–320.
[69] V. Debout, et al., Investagetion of in-light particle characteristics and Microstructural effects on optical properties of YSZ plasma-sprayed coatings, High Temp. Mater. Process. 11 (2007) 309–320.
[70] a Refke, G. Barbezat, Characterization of LPPS processes under various spray conditions for potential applications, in: International Thermal Spray Conference 2003, (May), 2003, pp. 581–588.
[71] Z. Salhi, S. Guessasma, P. Gougeon, D. Klein, C. Coddet, Diagnostic of YSZ in-flight particle characteristics under low pressure VPS conditions, Aero. Sci. Technol. 9 (2005) 203–209.
[72] D. Zhou, D. Sebold, D. Emil, M. Emine, O. Guillon, R. Vaßen, D.E. Mack, E. Bakan, G. Mauer, D. Sebold, O. Guillon, R. Vaßen, Thermal cycling performances of multilayered yttria-stabilized zirconia/gadolinium zirconate thermal barrier coatings, J. Am. Ceram. Soc. 103 (3) (2020) 2048–2061.
[73] A. Dolmaire, E. Hartikainen, S. Goutier, E. Béchade, M. Vardelle, P.M. Geffroy, A. Joulia, Benefits of hydrogen in a segmented-anode plasma torch in suspension plasma spraying, J. Therm. Spray Technol. 30 (1) (2021) 236–250.
[74] R. Westhoff, G. Trapaga, J. Szekely, Plasma-particle interactions in plasma spraying systems, Metall. Trans. A B 23 (6) (1992) 683–693.
[75] J.J. Tian, S.W. Yao, S.L. Zhang, C.J. Li, Effect of the shell-core-structured particle design on the heating characteristic of nickel-based alloy particle during plasma spraying, Surf. Coating. Technol. 335 (December 2017) (2018) 52–61.
[76] L. Pawlowski, Suspension and solution thermal spray coatings, Surf. Coating. Technol. 203 (19) (2009) 2807–2829.
[77] P. Fauchais, Understanding plasma spraying, J. Phys. Appl. Phys. 37 (9) (2004).
[78] C. Wang, R. Xu, Y. Song, P. Jiang, Study on water droplet flash evaporation in vacuum spray cooling, Int. J. Heat Mass Tran. 112 (2017) 279e288.
[79] E. Sadeghi, N. Markocsan, S. Joshi, Advances in corrosion-resistant thermal spray coatings for renewable energy power plants. Part I: effect of composition and microstructure, in: Journal of Thermal Spray Technology, vol. 28, Springer US, 2019. Issue 8.
[80] G.M. Faeth, L.P. Hs, K W P, Structure and breakup properties of sprays, Int. J. Multiphas. Flow 21 (1995) 99e127.
[81] G. Polanco, A.E. Holdø, G. Munday, General review of flashing jet studies, J. Hazard Mater. 173 (1e3) (2010) 2e18.
[82] X. Chen, D. Ma, V. Yang, S. Popinet, High-fidelity simulations of impinging jet atomization, Atomization Sprays 23 (12) (2013) 1079e1101.
[83] L. Opfer, I.V. Roisman, J. Venzmer, M. Klostermann, C. Tropea, Droplet-air collision dynamics: evolution of the film thickness, Phys. Rev. 89 (1) (2014) 1e6.
[84] M. Wang, M. Broumand, M. Birouk, Liquid Jet Trajectory in a Subsonic Gaseous Cross-Flow: an Analysis of Published Correlations, Atomization Sprays, 2016.
[85] B.A. Movchan, Inorganic materials and coatings produced by EBPVD, Surf. Eng. 22 (1) (2006) 35e46.
[86] E.H. Jordan, C. Jiang, M. Gell, The solution precursor plasma spray (SPPS) process: a review with energy considerations, J. Therm. Spray Technol. 24 (7) (2015) 1153e1165.
[87] P. Xu, T.W. Coyle, L. Pershin, J. Mostaghimi, Fabrication of superhydrophobic ceramic coatings via solution precursor plasma spray under atmospheric and low-pressure conditions, J. Therm. Spray Technol. 28 (1e2) (2019) 242e254.
[88] B. Bernard, A. Quet, L. Bianchi, V. Schick, A. Joulia, A. Mali e, B. R emy, Effect of suspension plasma-sprayed YSZ columnar microstructure and bond coat surface preparation on thermal barrier coating properties, J. Therm. Spray Technol. 26 (6) (2017) 1025e1037.
[89] A. Shinozawa, K. Eguchi, M. Kambara, T. Yoshida, Feather-like structured YSZ coatings at fast rates by plasma spray physical vapor deposition, J. Therm. Spray Technol. 19 (1–2) (2010) 190–197.
[90] .C.X. Li, S.H. Liu, H.Y. Zhang, et al., An introduction and progress of a novel atmospheric laminar plasma spray method, China Surface Engineering 32 (6) (2019) 1–19.
[91] J. Wen, C. Song, T. Liu, Z. Deng, S. Niu, Y. Zhang, Fabrication of dense gadolinia-doped ceria coatings via very-low-pressure plasma spray and plasma sprayephysical vapor deposition process, Coatings 9 (717) (2019).
[92] O. Racek, The effect of HVOF particle-substrate interactions on local varia- tions in the coating microstructure and the corrosion resistance, J. Therm. Spray Technol. 19 (5) (2010) 841e851.
[93] X.F. Zhang, K.S. Zhou, C.M. Deng, M. Liu, Z.Q. Deng, C.G. Deng, J.B. Song, Gas-deposition mechanisms of 7YSZ coating based on plasma spray-physical vapor deposition, J. Eur. Ceram. Soc. 36 (3) (2016) 697e703.
[94] L.H. Gao, L. Wei, H.B. Guo, S. Gong, H. Xu, Deposition mechanisms of yttria-stabilized zirconia coatings during plasma spray physical vapor deposition, Ceram. Int. 42 (4) (2016) 5530e5536.
[95] H. Li, X. Chen, Three-dimensional simulation of a plasma jet with transverse particle and carrier gas injection, Thin Solid Films 390 (2001) 175–180.
[96] D.-Y. Xu, X. Chen, K. Cheng, Three-dimensional modelling of the characteristics of long laminar plasma jets with lateral injection of carrier gas and particulate matter, J. Phys. Appl. Phys. 36 (13) (2003) 1583–1594.
[97] H. Li, X. Chen, Three-dimensional modeling of the turbulent plasma jet impinging upon a flat plate and with transverse particle and carrier-gas injection, Plasma Chem. Plasma Process. 22 (1) (2002).

[98] A.B. Murphy, C.J. Arundelli, Transport coefficients of argon, nitrogen, oxygen, argon-nitrogen, and argon-oxygen plasmas, Plasma Chem. Plasma Process. 14 (4) (1994) 451–490.

[99] A.B. Murphy, Transport coefficients of air, argon-air, nitrogen-air, and oxygen-air plasmas, Plasma Chem. Plasma Process. 15 (2) (1995) 279–307.

[100] A.B. Murphy, Transport coefficients of helium and argon – helium plasmas, IEEE Trans. Plasma Sci. 25 (5) (1997) 809–814.

[101] M. Boulos, P. Fauchais, E. Pfender, Thermal Plasmas: Fundamentals and Applications, Springer Science+Business Media, 1994.

[102] Chen xi. Thermal Plasma Heat Transfer and Flow. Science press.

[103] A.B. Murphy, Thermal plasmas in gas mixtures, J. Phys. Appl. Phys. 34 (20) (2001) R151–R173.

[104] A.B. Murphy, Diffusion in equilibrium mixtures of ionized gases, Phys. Rev. 48 (5) (1993) 3594.

[105] A.B. Murphy, A comparison of treatments of diffusion in thermal plasmas, J. Phys. Appl. Phys. 29 (7) (1996) 1922.

[106] A. Vardelle, P. Fauchais, B. Dussoubs, N.J. Themelis, Heat generation and particle injection in a thermal plasma torch, Plasma Chem. Plasma Process. 18 (4) (1998) 551–574.

[107] K. Pourang, C. Moreau, A. Dolatabadi, A three-dimensional analysis of the suspension plasma spray impinging on a curved substrate, J. Therm. Spray Technol. 24 (1–2) (2015).

[108] J.C. Beale, R.D. Reitz, Modeling spray atomization with the Kelvin-Helmholtz/Rayleigh-Taylor hybrid model, Atomization Sprays 9 (6) (1999).

[109] M. Jadidi, M. Mousavi, S. Moghtadernejad, A. Dolatabadi, A three-dimensional analysis of the suspension plasma spray impinging on a flat substrate, J. Therm. Spray Technol. 24 (January) (2015) 11–23.

[110] C.J. Li, B. Sun, Microstructure and property of micro-plasma-sprayed Cu coating, Mater. Sci. Eng. 379 (1–2) (2004) 92–101.

[111] C.J. Li, B. Sun, Microstructure and property of Al2O3 coating microplasma-sprayed using a novel hollow cathode torch, Mater. Lett. 58 (1–2) (2004) 179–183.

[112] T. Liu, S.W. Yao, L.S. Wang, G.J. Yang, C.X.C.J. Li, C.X.C.J. Li, Plasma-sprayed thermal barrier coatings with enhanced splat bonding for CMAS and corrosion protection, J. Therm. Spray Technol. 25 (1–2) (2016) 213–221.

[113] https://www.marketsandmarkets.com/Market-Reports/thermal-spray-coating-market.

[114] https://www.grandviewresearch.com/industry-analysis/thermal-spray-coatings-market.

[115] Sen-Hui Liu, J.P. Trelles, A.B. Murphy, L. Li, S. Zhang, G.-J. Yang, Chang-Jiu Li, Chen-Xin Li, Numerical simulation of the flow characteristics inside a novel plasma spray torch, J. Phys. Appl. Phys. 52 (33) (2019): 335203.

[116] Sen-Hui Liu, Gang Ji, Chang-Jiu Li, H.-B.G. Cheng-Xin Li, Novel long laminar plasma sprayed hybrid structure thermal barrier coatings for high-temperature anti-sintering and volcanic ash corrosion resistance, J. Mater. Sci. Technol. 79 (5) (2021) 141–146.

[117] Jiang long Wang, Investments of Mental Rapid Manufacturing by Laminar Plasma Torch, University of Science and Technology of China, 2015 (M.D dissertation. In Chinese).

[118] O. Solonenko, A.V. Smirnov, Advanced oxide powders processing based on cascade plasma, J. Phys. Conf. Ser. 550 (2014) 120–127.

[119] W. Ma, Q. Fei, W. Pan, C. Wu, Investigation of laminar plasma remelting/cladding processing, Appl. Surf. Sci. 252 (10) (2006) 3541–3546.

[120] W.X. Pan, X. Meng, G. Li, Q.X. Fei, C.K. Wu, Feasibility of laminar plasma-jet hardening of cast iron surface, Surf. Coat. Technol. 197 (2–3) (2005) 345–350.

[121] Sen-Hui Liu, Cheng-Xin Li, Li Lu, Jia-Hua Huang, Pan Xu, G.-J.Y. Ying-Zhen Hua, C.-J. Li, Development of long laminar plasma jet on thermal spraying process: microstructures of zirconia coatings, Surf. Coating. Technol. 337 (2018) 241–249.

[122] V.I. Kuz′Min, O.P. Solonenko, M.F. Zhukov, Application of DC Plasma Torch with a Quasi-Laminar Jet Outflow. 1995 National Thermal Spray Conference, 1995, pp. p11–15. Houston, TX (United States).

[123] O.P. Solonenko, H. Nishiyama, A.V.V. Smirnov, H. Takana, J. Jang, Visualization of arc and plasma flow patterns for advanced material processing, J. Visual 18 (2014) 1–15.

[124] H.C. Wu, X.D. Yang, A Plasma Torch Used in Thermal Spray, CN2413467, 1999: 19990910. http://www.patent-cn.com/H05H/CN2413467.shtml.

[125] K. Osaki, O. Fukumasa, A. Kobayashi, High thermal efficiency-type laminar plasma jet generator for plasma processing, Vacuum 59 (2000) 47–54.

[126] W. Pan, W. Zhang, W. Zhang, C. Wu, Generation of long, laminar plasma jets at atmospheric pressure and effects of flow turbulence, Plasma Chem. Plasma Process. 21 (1) (2001) 23–35.

[127] Y. Ando, S. Tobe, H. Tahara, M. Tokuyama, I. Oppenheim, H. Nishiyama, TiO2 film deposition by atmospheric thermal plasma CVD using laminar and turbulence plasma jets, AIP Conf. Proc. 982 (2008) 612–617.

[128] M. Khutsishvili, L. Kikvadze, H.-J. Hartfuss, M. Dudeck, J. Musielok, M. J. Sadowski, Spraying powder materials by the high-enthalpy laminar plasma flow, AIP Conf. Proc. 993 (2008) 423–426.

[129] H. Hideki, W. Fuminori, T. Sunao, N. Tetsurou, Development of quasi laminar plasma DC torch, J. Jpn. Inst. Metals 4 (2001) 5–6 (in Japanese).

[130] F.W. Hideki Hamatani, Development of laminar plasma shielded HF-ERW process, Proceedings of the 2012 9th International Pipeline Conference 1–8 (2012).

[131] J. Tang, S. Li, W. Zhao, Y. Wang, Y. Duan, Development of a stable dielectric-barrier discharge enhanced laminar plasma jet generated at atmospheric pressure, Appl. Phys. Lett. 100 (25) (2012) p253–255.

[132] J. Krowka, V. Rat, C. Chazelas, J.-F. Coudert, Pulsed laminar arc jet with synchronized suspension injection-spectroscopic studies, J. Phys. Conf. 550 (2014): 12020.

[133] J. Miao, D. Yu, X. Cao, Y. Xiang, M. Xiao, J. Yao, Experimental study on the characteristics of a miniature laminar plasma torch with different gas flow patterns, Plasma Chem. Plasma Process. 35 (5) (2015) p879–893.

[134] X. Cao, D. Yu, M. Xiao, J. Miao, Y. Xiang, J. Yao, Design and characteristics of a laminar plasma torch for materials processing, Plasma Chem. Plasma Process. 36 (2) (2016) p693–710.

[135] Jiang long Wang, Investments of Mental Rapid Manufacturing by Laminar Plasma Torch, University of Science and Technology of China, M.D dissertation, 2015 (In Chinese).

[136] M. Li, T. Lu, J. Dai, X. Jia, X. Gu, T. Dai, Microstructure and mechanical properties of 308L stainless steel fabricated by laminar plasma additive manufacturing, Materials Science and Engineering A-Structural Materials Properties Microstructure and Processing 770 (2020): 138523.

[137] X. Cao, C. Li, R. He, H. Xu, L. Chen, B. Huang, Study on the influences of the anode structures on the jet characteristics of a laminar plasma torch, Plasma Research Express 2 (1) (2020): 18001.

[138] X. Cao, C. Li, L. Chen, B. Huang, Experimental study on the design and characteristics of a laminar plasma torch with medium working power and its applications for surface hardening, IEEE Trans. Plasma Sci. 48 (4) (2020) 961–968.

[139] N. Orlovskaya, Y. Gogotsi, M. Reece, B. Cheng, I. Gibson, Ferroelasticity and hysteresis in LaCoO based perovskites, Acta Mater. 50 (2002) 715e723.

[140] J. Yao, L. Yang, L. Bo, Z. Li, Characteristics and performance of hard Ni60 alloy coating produced with supersonic laser deposition technique, Mater. Des. 83 (2015) 26–35.

[141] https://www.oerlikon.com/ecomaXL/metco/files/oerlikon_DSMTS-0019.2_8YO_ZrO_Agglom.pdf&download=1.

[142] V. Rat, J.F. Coudert, P. Fauchais, N. Caron, K. Wittman, S. Alexandre, Influence of plasma instabilities in ceramic suspension plasma spraying, J. Therm. Spray Technol. 16 (December) (2007) 857–865.

[143] L. Pawlowski, Suspension and solution thermal spray coatings, Surf. Coating. Technol. 203 (19) (2009) 2807–2829.

[144] P. Fauchais, Suspension and solution plasma spraying, J. Phys. Appl. Phys. 46 (2013): 224015.

[145] H.B. Guo, R. VaEn, D. StVer, Surf. Coat. Technol. 186 (2004) 353–363.

[146] M. Karger, R. Vaßen, D. Stöver, Surf. Coat. Technol. 206 (1) (2011) 16–23.

[147] E.H. Jordan, C. Jiang, J. Roth, M. Gell, J. Therm. Spray Technol. (2014) 849–859.

[148] Y.P. Wang, S.H. Liu, H.Y. Zhang, C.X. Li, S.L. Zhang, G.J. Yang, C.J. Li, Structured La0.6Sr0.4Co0.2Fe0.8O3-δ cathode with large-scale vertical cracks by atmospheric laminar plasma spraying for IT-SOFCs, J. Alloys Compd. 825 (2020): 153865.

[149] H. Zhang, C. Li, S. Liu, L. Li, G. Yang, C. Li, Splash involved deposition behavior and erosion mechanism of long laminar plasma sprayed NiCrBSi coatings, Surf. Coating. Technol. 395 (May) (2020): 125939.

[150] H. Zhang, S. Liu, C. Li, C. Li, Deposition and oxidation behavior of atmospheric laminar plasma sprayed Mo coatings from 200 mm to 400 mm under 20 kW : numerical and experimental analyses, Surf. Coating. Technol. 400 (May) (2020).

[151] L.H. Chen, C.Y. Chen, Y.L. Lee, Nucleation and growth of clusters in the process of vapor deposition, Surf. Sci. 429 (1) (1999) 150e160.

[152] M.F. Smith, A.C. Hall, J.D. Fleetwood, P. Meyer, Very low pressure plasma spray-a review of an emerging technology in the thermal spray community, Coatings 1 (2) (2011) 117–132.

[153] S. Li, W. He, J. Shi, L. Wei, J. He, H. Guo, PS-PVD gadolinium zirconate thermal barrier coatings with columnar microstructure sprayed from sintered powder feedstocks, Surf. Coating. Technol. 383 (August 2019) (2020): 125243.

[154] C. Zhao, W. He, J. Shi, Q. Guo, J. Li, H. Guo, Deposition mechanisms of columnar structured La2Ce2O7 coatings via plasma spray-PVD, Ceram. Int. 46 (9) (2020) 13424–13432.

[155] K. Von Niessen, M. Gindrat, A. Refke, Vapor phase deposition using plasma spray-PVDTM, J. Therm. Spray Technol. 19 (1–2) (2010) 502–509.

[156] G. Mauer, A. Hospach, R. Vaßen, Process development and coating characteristics of plasma spray-PVD, Surf. Coating. Technol. 220 (2013) 219–224.

[157] M. Liu, G. Zhang, Y. Lu, J. Han, G. Li, Plasma Spray – Physical Vapor Deposition toward Advanced Thermal Barrier Coatings : a Review, Rare Metals, 2020.

[158] P. He, H. Sun, Y. Gui, F. Lapostolle, H. Liao, C. Coddet, Microstructure and properties of nanostructured YSZ coating prepared by suspension plasma spraying at low pressure, Surf. Coating. Technol. 261 (2015) 318–326.

[159] J. Shi, S. Liu, J. Li, W. Chen, W. He, H. Peng, Low vacuum enhanced expansion of a supersonic arc plasma plume, Vacuum 198 (November 2021) (2022): 110858.

[160] N. Zhang, F. Sun, L. Zhu, M.P. Planche, H. Liao, C. Dong, C. Coddet, Measurement of specific enthalpy under very low pressure plasma spray condition, J. Therm. Spray Technol. 21 (3) (2012) 489–495.

[161] L. Zhu, N. Zhang, B. Zhang, F. Sun, R. Bolot, M.P. Planche, C. Coddet, Very low pressure plasma sprayed alumina and yttria-stabilized zirconia thin dense coatings using a modified transferred arc plasma torch, Appl. Surf. Sci. 258 (4) (2011) 1422–1428.

[162] Shi Jia, SenHui Liu, Hongo Guo, et al., Low Vacuum Enhanced Expansion of the Arc Plasma Plume for Deposition of Ceramic Coatings, 2022. Materials Letter (under review).

[163] A.B. Murphy, M.I. Boulos, V. Colombo, P. Fauchais, E. Ghedini, A. Gleizes, J. Mostaghimi, P. Proulx, D C S, Advanced thermal plasma modelling, High Temperature Material Processing 12 (2008) 255–336.

[164] A. Gleizes, Perspectives on thermal plasma modelling, Plasma Chem. Plasma Process. (2014) 455–469.
[165] R. Huang, H. Fukanuma, Y. Uesugi, Y. Tanaka, An improved local thermal equilibrium model of DC arc plasma torch, IEEE Trans. Plasma Sci. 39 (10) (2011): 1974e1982.
[166] A. Gleizes, J.J. Gonzalez, P. Freton, Thermal plasma modelling, J. Phys. Appl. Phys. 38 (9) (2005) R153–R183, https://doi.org/10.1088/0022-3727/38/9/R01.
[167] V. Bianco, A. Khait, A. Noskov, V. Alekhin, A comparison of the application of RSM and LES turbulence models in the numerical simulation of thermal and flow patterns in a double-circuit Ranque-Hilsch vortex tube, Appl. Therm. Eng. 106 (2016) 1244e1256.
[168] Q. Zhou, H. Li, X. Xu, F. Liu, S. Guo, X. Chang, P. Xu, Comparative study of turbulence models on highly constricted plasma cutting arc, J. Phys. D 42 (1) (2009): 15210.
[169] X C, M. Liu, G.F. Xu, et al., Numerical simulation for heat transfer and flow of plasma in LPPS, China Surf. Eng. 28 (5) (2015) 57e63 (In Chinese).
[170] V.I. Zapryagaev, V.M. Boiko, I.N. Kavun, N.P. Kiselev, A.A. Pivovarov, Flow structure behind the Mach disk in supersonic non-isobaric jet, in: AIP Conference Proceedings, 1770(October), 2016.
[171] P. Reijasse, F. Bouvier, P. Servel, Experimental and numerical investigation of the cap-shock structure in overexpanded thrust-optimized nozzles, in: D.E. Zeitoun, et al. (Eds.), West East High Speed Flow Fields 2002, Conference Proceedings, CIMNE, Barcelona, 2003, pp. 338–345.
[172] A. Vardelle, P. Fauchais, B. Dussoubs, N.J. Themelis, Heat generation and particle injection in a thermal plasma torch, Plasma Chem. Plasma Process. 18 (4) (1998) 551–574.
[173] R. Bolot, C. Coddet, M. Imbert, Mathematical modeling of a free plasma jet discharging into air and comparison with probe measurements, in: C.C. Berndt (Ed.), Thermal Spray: A United Forum for Scienti®c and Technological Advances, Pub. ASM International, Materials Park, OH, USA, 1997, p. 549±555.
[174] R. Bolot, V. Monin, M. Imbert, C. Coddet, Mathematical modeling of a plasma jet impinging on a ¯at structure, in: C. Coddet (Ed.), Thermal Spray: Meeting the Challenges of the 21th Century, vol. 1, Pub. ASM International, Materials Park, OH, USA, 1998, p. 439±444.
[175] L.I. Jia-rong, L.I.U. Shi-zhong, S.H.I. Zhen-xue, Yu-shi Luo, W.A.N.G. Xiao-guang, Third generation single crystal superalloy DD9, J. Iron Steel Res. (2011), https://doi.org/10.13228/j.boyuan.issn1001-0963.2011.s2.088 v23-2 (In Chinese).
[176] S. Li, W. He, J. Shi, L. Wei, J. He, H. Guo, PS-PVD gadolinium zirconate thermal barrier coatings with columnar microstructure sprayed from sintered pow- der feedstocks, Surf. Coating. Technol. 383 (2020): 125243. August 2019.
[177] C. Zhao, W. He, L. Wei, H. Guo, Microstructures of La2Ce2O7 coatings pro- duced by plasma spray-physical vapor deposition, J. Eur. Ceram. Soc. 40 (4) (2020) 1462e1470.
[178] Li-hua Gao, Yu Yue-guang, Fang Jia, Ji Xiao-juan, De-ming Zhang, Progress in plasma spray-physical vapor deposition thermal barrier coatings, Therm. Spray Technol. 2 (9) (2017) (In Chinese).
[179] M.F. Smith, R.C. Dykhuizen, Effect of chamber pressure on particle velocities in low pressure plasma spray deposition, Surf. Coating. Technol. 34 (1) (1988) 25–31.
[180] S. Sodeoka, M. Suzuki, T. Inoue, Control of plasma sprayed tempera- ture and velocity by chamber pressure, in: C.C. Berndt, K.A. Kohr, E.F. Lugscheider (Eds.), Thermal Spray 2001: New Surfaces for a NewMil- Lenium, ASM International, Materials Park, OH, USA, 2001, pp. 737–741.
[181] M. Lang, R. Henne, S. Schaper, G. Schiller, Development and charac- terization of vacuum plasma sprayed thin film solid oxide fuel cells, J. Therm. Spray Technol. 10 (2001) 618–625.
[182] V. Rat, E. Bouyer, R.H. Henne, DC plasma diagnostics for improvement of the plasma process under soft vacuum conditions, in: C. Moreau, B. Marple (Eds.), Thermal Spray 2003, ASMInternational, Materials Park, OH, USA, 2003, pp. 1269–1278.
[183] LawlessWN, T.K. Gupta, Thermal properties of tetragonal ZrO2 at low temperatures, Phys. Rev. B 28 (1983), 5507–10.
[184] ChupkaWA, J. Berkowitz, M.G. Inghram, Thermodynamics of the Zr-ZrO2 system: the dissociation energies of ZrO and ZrO2, J. Chem. Phys. 26 (1957) 1207.
[185] S.J. Elliott, Thermodynamic modeling of the zirconia, J. Am. Ceram. Soc. 85 (2002), 2903–10.
[186] B.P. Zhang, L. Wei, H.B. Guo, H.B. Xu, Microstructures and deposition mechanisms of quasi-columnar structured yttria-stabilized zirconia coatings by plasma spray physical vapor deposition, Ceram. Int. 43 (15) (2017) 12920–12929.
[187] M. Baeva, Non-equilibrium modeling of tungsten-inert gas arcs, Plasma Chem. Plasma Process. 37 (2) (2017) 341–370.
[188] J. Hong, S. Su, R. Sun, L. Hui, Z. Hai, X. Wang, Two - Temperature Chemical Non - Equilibrium Modeling of Argon DC Arc Plasma Torch, Plasma Chemistry and Plasma Processing, 2020: 0123456789.
[189] H. Sun, Y. Wu, Y. Tanaka, K. Tomita, Investigation on chemically non-equilibrium arc behaviors of different gas media during arc decay phase in a model circuit breaker, J. Phys. Appl. Phys. 52 (2019), 0725202.
[190] W. He, G. Mauer, R. Vaßen, Excitation temperature and constituent concentration profiles of the plasma jet under plasma spray-PVD, Plasma Chem. Plasma Process. 37 (5) (2017) 1293–1311.
[191] A. Anwaar, L. Wei, Q. Guo, B. Zhang, H. Guo, Novel prospects for plasma spray–physical vapor deposition of columnar thermal barrier coatings, J. Therm. Spray Technol. 26 (8) (2017) 1810–1822.
[192] W K, M. Liu, J. Mao, Z.Q. Deng, Kui Wen, Spectroscopic method for diagnosing PS-PVD jet for different gas composition, Spectroscopy ans Spectral Analysis 37 (10) (2017) (In Chinese).
[193] G. Mauer, R. Vaßen, Plasma Spray-PVD: plasma characteristics and impact on coating properties, J. Phys. Conf. 406 (1) (2012).
[194] J.P. Trelles, Computational study of flow dynamics from a dc arc plasma jet, J. Phys. Appl. Phys. 46 (2013): 255201.
[195] X. Chen, P. He, Heat transfer from a rarefied plasma flow to a metallic or nonmetallic particle, Plasma Chem. Plasma Process. 6 (4) (1986) 313–333.
[196] J.P. Trelles, Advances and challenges in computational fluid dynamics of atmospheric pressure plasmas, Plasma Sources Sci. Technol. 27 (2018).